Microstructural evolution in deformed austenitic TWinning Induced Plasticity steels

Ronald Theodoor VAN TOL

Microstructural evolution in deformed austenitic TWinning Induced Plasticity steels

Proefschrift

ter verkrijging van de graad doctor
aan de Technische Universiteit Delft,
op gezag van de Rector Magnificus Prof. ir. K.C.A.M. Luyben,
voorzitter van het college voor Promoties,
in het openbaar te verdedigen
op donderdag 17 april 2014 om 12:30 uur
door

Ronald Theodoor VAN TOL

werktuigbouwkundig ingenieur,
geboren te 's-Gravenzande.

Dit proefschrift is goedgekeurd door de promotor:
Prof.dr.ir. J. Sietsma

Samenstelling promotiecommissie:

Rector Magnificus	Voorzitter
Prof.dr.ir. J. Sietsma	Technische Universiteit Delft, promotor
Prof.dr. R. Boom	Technische Universiteit Delft
Prof.dr.ir. L.A.I. Kestens	Universiteit Gent, Belgium
Prof.dr.ir. B.C. De Cooman	Pohang University of Science and Technology, South-Korea
Prof.dr. K. Tsuzaki	Kyushu University, Japan
Dr. L. Zhao	VDL Weweler, Apeldoorn
Dr.ir. M. van der Winden	TATA Steel Europe, IJmuiden
Prof.dr. I.M. Richardson	Technische Universiteit Delft, reservelid

Dr. L. Zhao heeft als begeleider in belangrijke mate aan de totstandkoming van het proefschrift bijgedragen.

This research was carried out under the project number MC10.07292 in the framework of the Research Program of the Materials innovation institute (M2i, www.m2i.nl). The support of Tata Steel Europe is gratefully acknowledged.

Copyright © 2014 by R.T. van Tol
All rights reserved. No part of this book may be reproduced, stored in a retrieval system or transmitted, in any form or by any means, without the prior permission from the copyright owner.

ISBN: 978-94-6108-650-1

Printed by: Gildeprint Drukkerijen, Enschede, The Netherlands

Cover and chapter headings by A-creation (www.a-creation.nl) and Mak van Tol

To our twins

Dankwoord

Dit boekje markeert het einde van een prachtige tijd in Delft en IJmuiden, maar nu is het mooi geweest. Dank

aan mijn begeleiders voor dit ‘geschenk’. Jilt, we zijn begonnen met Callister en geëindigd met een paper in Acta. Bedankt voor al je aandacht en vooral je geduld. Lie, we hebben elkaar goed leren kennen en waarderen. Bedankt voor je kritische houding en oog voor detail. Henk, een goed begin is het halve werk: jouw vakmanschap en bovenal schrijfkunsten hebben mij goed op weg geholpen.

aan de Hoogovenaren voor deze kans, de (financiële) steun en toeverlaat; ik ben mij ervan bewust dat ik de afgelopen jaren in een bevoorrechte positie heb verkeerd. Een aantal mensen wil ik hiervoor in het bijzonder bedanken. Mark (Maier), Pieter en Richard voor het steunen en aanmoedigen van dit initiatief. Rob, Leo, Jan (Bottema), René, Lene en Arjan voor de totstandkoming van dit project. Marc (Cornelissen), ik heb veel van je geleerd, vooral van je scherpe blik. Freek, bedankt voor het realisme. Basjan, Pascal, Patricia, Menno, Maxim en Jan (Heijne) voor jullie inbreng en nog belangrijker luisterend oor. Jan (Brussel), Floor, Edward, Lieven en Guido voor de mooie tijd, we hebben veel gelachen. Peter, ‘samen’ een promotietraject in, een uitstekende gelegenheid om eens te bomen en dat hebben we geweten! Verder natuurlijk al mijn andere collega’s in de kennisgroepen en IJmuiden. Helaas zijn we geen directe collega’s meer.

aan de Delftenaren voor het bij tijd en wijle onderbreken van de eenzaamheid, in het bijzonder aan Andrea voor de ‘Duitse onderonsjes’ en Monica voor de spontaniteit.

aan de ‘Koreanen’ voor de gastvrijheid, met name Bruno (Prof. De Cooman) en Jin-Kyung.

aan de technici voor het doen wat ikzelf liever laat doen: Leon, Aad en Bert van DEMO, Niek, Rob, Ruud en Kees van 3mE en Mohammed van SKF, bedankt!

aan de studenten voor jullie interesse en enthousiasme, in het bijzonder Tjerk.

aan mijn (schoon)familie en vrienden voor alles wat niets met dit proefschrift van doen heeft.

aan Annemieke, Mak, Cas† en Lem voor waar het eigenlijk om te doen is.

Ron van Tol

’s-Gravenzande, maart 2014

Summary

This thesis studies the effect of plastic deformation on the stability of the austenitic microstructure against martensitic transformation and diffusional decomposition and its role in the phenomenon of delayed fracture in austenitic manganese (Mn)-based TWinning Induced Plasticity (TWIP) steels. The transformation to α'-martensite upon mechanical loading and diffusional decomposition into pearlite upon annealing at intermediate temperatures shows the austenite to be metastable. An increase in the austenite stability is expected to improve the resistance against delayed fracture.

In the automotive industry, the requirements for fuel economy and safety are continuously increasing. Improvements in fuel economy require a lower weight of the vehicle whereas improvements in safety often result in additional weight. To resolve this contradiction, the requirements for strength and formability of steel increase continuously. To this purpose, the steel industry develops (Advanced) High Strength Steels and Press Hardening Steels. One of the latest developments is fully austenitic Mn-based TWIP steels that combine a high strength with a very high uniform elongation. These superior mechanical properties result from the high work-hardening of these austenitic Mn-based TWIP steels. The main reasons for this high work-hardening are deformation mechanisms combining slip of dislocations with strain induced microtwinning and martensite transformation. The deformation mechanisms relate to the austenite stability and form shear bands like slip bands, twins and/or ε-martensite laths, which are obstacles for further dislocation glide increasing work-hardening.

In addition to usual application issues like formability and weldability, a problem encountered with austenitic Mn-based TWIP steels is delayed fracture. This is the phenomenon that even after successful forming, fracture may still occur. The time until fracture can range from seconds to weeks. Increased understanding of the phenomenon of

delayed fracture would accelerate the introduction of austenitic Mn-based TWIP steels to the automotive industry, enabling further weight reduction and improved safety and fuel economy.

The susceptibility to delayed fracture is a combination of (1) the austenite stability against microstructural defect formation, (2) the internal residual stress and (3) the presence of mobile hydrogen. Most research on delayed fracture concentrates on the role of hydrogen, leaving the austenite stability against defect formation and internal residual stress underexposed. Increasing the austenite stability against microstructural defect formation like strain-induced transformation improves the resistance against delayed fracture. This work discusses the effect of plastic deformation on the stability of the austenitic microstructure against martensitic transformation and diffusional decomposition and its role in the phenomenon of delayed fracture.

The effect of deep drawing on the generation of structural defects in austenitic Mn-based TWIP steels is investigated experimentally using X-ray diffraction, positron annihilation Doppler broadening spectroscopy and magnetic measurements. To this purpose, the characteristics of defects were studied along the wall of deep-drawn cups, representing a gradually changing deformation state. Positron annihilation detects that two different defect types result from plastic deformation during deep drawing. The two defect types can be expected to be dislocations and partial dislocations. Magnetic field measurements reveal the formation of α'-martensite which correlates with the density of the defects identified as partial dislocations.

The effect of strain on the defect and microstructure evolution in austenitic Mn-based TWIP steels is experimentally investigated using magnetic measurements, X-ray diffraction, positron beam Doppler Spectroscopy and Transmission Electron Microscopy techniques. The strain evolution during deep drawing is simulated by means of Finite Element Method simulations. The formation of α'-martensite is attributed to the accumulated equivalent strain and crystallographic texture. The presence of α'-martensite is observed at shear band and twin intersections and questions the sequential $\gamma \rightarrow \varepsilon \rightarrow \alpha$' martensitic transformation. The results indicate that the formation of α'-martensite in a high Stacking Fault Energy (SFE) Face Centred Cubic alloy does not necessarily require the intermediate formation of ε-martensite laths. A model for α'-martensite volume fraction evolution upon straining is proposed and the estimated fraction of intersected shear bands - the preferred nucleation sites for α'-martensite formation - as a function of accumulated equivalent strain is in good agreement with the experimentally determined α'-martensite fraction.

The role of α'-martensite in the phenomenon of delayed fracture is studied in austenitic Mn-based TWIP steels after deep drawing, observed by *in-situ* video recording. The formation of α'-martensite indicates the formation of crack initiation sites, which is discussed as a possible cause of delayed fracture. Delayed fracture occurs where the α'-martensite fraction is the highest. An intermittent crack propagation concept and model is proposed based on the coalescence of initial cracks into a macrocrack. A higher α'-martensite fraction indicates a higher density of shear-band intersections, resulting in more potential crack-initiation sites and easier coalescence. The SFE in the tested range of 22 to 52 mJ/m^2 does not affect the formation of α'-martensite and does not relate to the delayed fracture susceptibility.

The transformation of austenite by martensitic mechanisms upon plastic deformation shows the metastability of the austenite and indicates diffusional decomposition of austenite into pearlite in case the material is annealed at temperatures below the A_1-temperature. This transformation and the effect of prior plastic deformation on the austenite decomposition into pearlite at intermediate temperatures is investigated. The transformation kinetics are governed by Mn-partitioning between ferrite and cementite within the pearlite. Mn-diffusion is too slow to allow partitioning between pearlite and austenite, and a mixed equilibrium condition is established of ortho-equilibrium between ferrite and pearlite and para-equilibrium between pearlite and austenite. Nucleation of pearlite takes place only in the initial stages of the transformation. Prior plastic deformation enhances the formation rate of pearlite from austenite and increases the number density of pearlite colonies, primarily through increased nucleation efficiency. Prior plastic deformation does not significantly affect the nucleation rate or growth rate in the observed timescale.

Samenvatting

Dit proefschrift bestudeert het effect van plastische vervorming op de stabiliteit van de austenitische microstructuur tegen transformatie naar martensiet en perliet en haar rol in het fenomeen van vertraagde scheurvorming bij austenitische mangaan (Mn)-gelegeerde staalsoorten met tweeling-geïnduceerde plasticiteit (TWIP). De transformaties naar α'-martensiet door mechanische belasting en naar perliet op basis van diffusie door warmtebehandelingen laten zien dat het austeniet metastabiel is. Een toename van de austenietstabiliteit leidt naar verwachting tot een verbeterde weerstand tegen vertraagde scheurvorming.

De eisen voor brandstofverbruik en veiligheid in de automobielindustrie nemen gestaag toe. Een lager brandstofverbruik vereist een lager gewicht van het voertuig, terwijl een hogere veiligheid vaak in meer gewicht resulteert. Om deze tegenstelling het hoofd te bieden, moeten de sterkte en vervormbaarheid van staal omhoog. Hiervoor ontwikkelt de staalindustrie geavanceerde hoge sterkte en warmvervormbare staalsoorten. Een van de laatste ontwikkelingen is volledig austenitische Mn-gelegeerde TWIP-staalsoorten met hoge sterkte en zeer hoge uniforme rek. Deze superieure mechanische eigenschappen zijn het resultaat van de hoge werkversteviging van deze austenitische Mn-gelegeerde TWIP-staalsoorten. De hoofdredenen voor deze hoge werkversteviging zijn vervormings-mechanismen die slip van dislocaties combineren met vervormingsgeïnduceerde tweelingvorming en martensiet transformatie. De vervormingsmechanismen hangen samen met de austenietstabiliteit en vormen slipbanden, tweelingen en/of ε-martensietnaalden, welke obstakels zijn voor verdere dislocatiebeweging en daarmee de werkversteviging verhogen.

Naast gebruikelijke toepassingsproblemen zoals vervorm- en lasbaarheid, doet zich bij austenitische Mn-gelegeerde TWIP-staalsoorten het probleem van vertraagde scheurvorming voor. Dit is het fenomeen dat zelfs na succesvol vervormen, scheurvorming op kan treden. De tijd tot scheuren kan variëren van secondes tot weken. Een beter begrip van het fenomeen van vertraagde scheurvorming zal de introductie van austenitische Mn-gelegeerde TWIP-staalsoorten versnellen, met verdere gewichtsreductie en verbeterde veiligheid en brandstofverbruik tot gevolg.

De gevoeligheid voor vertraagde scheurvorming wordt bepaald door een combinatie van (1) de austenietstabiliteit tegen de vorming van microstructurele defecten, (2) de interne residuele spanning en (3) de aanwezigheid van mobiel waterstof. Het merendeel van het onderzoek naar vertraagde scheurvorming concentreert zich op de rol van waterstof, waardoor de austenietstabiliteit tegen de vorming van microstructurele defecten en de interne residuele spanning onderbelicht blijven. Een verhoogde austenietstabiliteit tegen de vorming van microstructurele defecten, zoals vervormingsgeïnduceerde transformatie, verbetert de weerstand tegen vertraagde scheurvorming. Dit proefschrift behandelt het effect van plastische vervorming op de stabiliteit van de austenitische microstructuur tegen transformatie naar martensiet en perliet en haar rol in het fenomeen van vertraagde scheurvorming.

Het effect van dieptrekken op de vorming van structurele defecten in austenitische Mn-gelegeerde TWIP-staalsoorten is experimenteel onderzocht door middel van röntgendiffractie, positronannihilatie Doppler verbredingspectroscopie en magnetische metingen. Hiervoor zijn de defect karakteristieken langs de wand van diepgetrokken bekers bestudeerd, die een geleidelijk veranderende vervormingstoestand representeren. Positronannihilatie heeft als gevolg van de plastische vervorming tijdens het dieptrekken twee verschillende soorten defecten waargenomen. De twee soorten defecten zijn naar verwachting dislocaties en partiële dislocaties. Magnetische metingen geven de vorming van α'-martensiet aan, welke samenhangt met de dichtheid van de defectsoort geïdentificeerd als partiële dislocaties.

Het effect van rek op de defect- en microstructuurevolutie bij austenitische Mn-gelegeerde TWIP-staalsoorten is experimenteel onderzocht door middel van magnetische metingen, röntgendiffractie, positronannihilatie Doppler verbredingspectroscopie en transmissie-electronenmicroscopie. De evolutie van de rek tijdens het dieptrekken is gesimuleerd met behulp van eindige-elementen-methode simulaties. De vorming van α'-martensiet wordt toegeschreven aan de geaccumuleerde equivalente rek en kristallografische textuur. De aanwezigheid van α'-martensiet is geobserveerd bij

vervormingsbanden en tweelingen en zet vraagtekens bij de sequentiële $\gamma \rightarrow \varepsilon \rightarrow \alpha'$ martensitische transformatie. De resultaten geven aan dat de vorming van α'-martensiet in een kubisch vlakken gecentreerde legering met een hoge StapelFoutEnergie (SFE) niet noodzakelijkerwijs de tussentijdse vorming van ε-martensietnaalden nodig heeft. Een model voor de evolutie van de α'-martensiet volumefractie afhankelijk van de rek wordt voorgesteld en de geschatte fractie van gekruiste vervormingsbanden - de voorkeurslocatie voor de nucleatie en vorming van α'-martensiet - als functie van de geaccumuleerde equivalente rek komt goed overeen met de experimenteel vastgestelde α'-martensietvolumefractie.

De rol van α'-martensiet in het fenomeen van vertraagde scheurvorming is onderzocht bij austenitische Mn-gelegeerde TWIP-staalsoorten na dieptrekken en waargenomen met behulp van *in-situ* video-opnames. De vorming van α'-martensiet wijst op de vorming van scheurinitiatiepunten, welke besproken worden als mogelijke oorzaak van vertraagde scheurvorming. Vertraagde scheurvorming treedt op daar waar de α'-martensietfractie het hoogst is. Een concept en een model voor schoksgewijze scheurgroei worden voorgesteld op basis van het samengroeien van initiële scheurtjes tot een scheur. Een hogere α'-martensietfractie duidt op een hogere dichtheid van gekruisde vervormingsbanden met als gevolg meer potentiële scheurinitiatiepunten en een eenvoudigere samengroei. De SFE in het geteste bereik van 22 tot 52 mJ/m^2 heeft geen invloed op de vorming van α'-martensiet en hangt niet samen met de gevoeligheid voor vertraagde scheurvorming.

De transformatie van austeniet door martensitische mechanismen als gevolg van plastische vervorming geeft de metastabiliteit van het austeniet aan en daarmee de transformatie van austeniet naar perliet in het geval van verhitting bij temperaturen onder de A_1-temperatuur. Deze transformatie van austeniet naar perliet en het effect van plastische vervorming hierop is onderzocht. De transformatiekinetiek wordt bepaald door de Mn-afscheiding tussen ferriet en cementiet binnenin het perliet. De Mn-diffusie is te langzaam voor Mn-afscheiding tussen perliet en austeniet. Een gemengde evenwichtstoestand vormt zich, bestaande uit een ortho-evenwicht tussen ferriet en perliet en een para-evenwicht tussen perliet en austeniet. De nucleatie van perliet vindt alleen plaats in de beginfase van de transformatie. Voorafgaande plastische vervorming versnelt de vorming van perliet en verhoogt de dichtheid van het aantal perlietkolonies, hoofdzakelijk door de toegenomen efficiëntie van de nucleatie. Voorafgaande plastische vervorming heeft binnen de onderzochte tijdspanne geen significant effect op de nucleatie- en groeisnelheid.

List of publications

R.T. van Tol, L. Zhao and J. Sietsma, Effect of strain on the deformation mechanism in austenitic Mn-based TWIP steels, The 1st International Conference on High Mn TWIP Steels HMnS2011, Seoul, South Korea, 2011.

R.T. van Tol, L. Zhao, H. Schut and J. Sietsma, Experimental investigation of structural defects in deep-drawn austenitic Mn-based TWIP steel, Material Science and Technology, vol. 28, no. 3, pp. 348-353, 2012 (Chapter 3).

R.T. van Tol, L. Zhao, H. Schut and J. Sietsma, Investigation of deformation mechanisms in deep-drawn and tensile-strained austenitic Mn-based TWIP steel, Metallurgical and Materials Transactions A, vol. 43, no. 9, pp. 3070-3077, 2012 (Chapter 4).

R.T. van Tol, J.K. Kim, L. Zhao, J. Sietsma and B.C. De Cooman, α'-Martensite Formation in deep-drawn Mn-based TWIP Steel, Journal of Materials Science, vol. 47, pp. 4845-4850, 2012 (Chapter 4).

R.T. van Tol, L. Zhao, L. Bracke, P. Kömmelt and J. Sietsma, Investigation of the delayed fracture phenomenon in deep-drawn austenitic manganese-based Twinning Induced Plasticity steels, Metallurgical and Materials Transactions A, vol. 44, no. 10, pp. 4654-4660, 2013 (Chapter 5).

R.T. van Tol, L. Zhao and J. Sietsma, Kinetics of austenite decomposition in manganese-based steel, Acta Materialia, vol. 64, pp. 33-40, 2014 (Chapter 6).

About the author

Ronald (Ron) Theodoor van Tol was born on July, 9th 1979 in 's-Gravenzande, The Netherlands. After his 'Athenaeum' (Dutch A-levels) at the Zandevelt College in 's-Gravenzande, he embarked on his studies in Mechanical Engineering at the Technische Universiteit Delft in 1997. In 2003 he obtained his 'ir' (M.Sc.) degree on the subject of Paint Bake Response of the Aluminium Body Front-end of the BMW 5-series, in close cooperation with the BMW Group in Munich (Germany).

After a year at Mitsubishi Heavy Industries, he joined Corus to work on the development of steel grades for the automotive industry in the Knowledge Group Strip Metallurgy for Automotive and Packaging in 2005. After three years, he was given the opportunity to start a PhD research at the Materials innovation institute (M2i) under the supervision of Prof.dr.ir. J. Sietsma and Dr. L. Zhao from the group of Microstructure Control in Metals (MCM) of the Department of Materials Science and Engineering (MSE) of the Faculty of Mechanical, Maritime and Materials Engineering (3mE) at the Technische Universiteit Delft.

Ron is currently Research Engineer Materials & Corrosion at Shell Projects & Technology, Innovation, Research & Development in Amsterdam.

Outline

1 Introduction

Steel is the most commonly used material in our daily life. Through time, steel technology has developed empirically into one of the most important drivers for human prosperity. It owes most of its success to the abundance of iron ore and coal and the good combination of price and properties, like manufacturing, mechanical, chemical, electrical, magnetic or thermal properties. This is a result of the ability of steel to allow for a variety of microstructural phases through alloying and thermomechanical treatment. The main disadvantage of steel however is weight. The automotive industry is one of the industries where steel is primarily used and the reduction of weight is of increasing importance. In the last decade the use of High Strength Steels (HSS), Advanced High Strength Steels (AHSS) and Press Hardening Steels (PHS) in the automotive industry has increased significantly in order to reduce weight and improve safety and fuel economy. The Automotive Group of the World Steel Association has developed the Future Steel Vehicle (Figure 1.1a)) to demonstrate the potential of (A)HSS and PHS. Figure 1.1b) shows the steel usage in the body structure of the Future Steel Vehicle [1] enabling a weight reduction of 35% compared to an equivalent design with Mild Steel.

Figure 1.2 shows the uniform elongation against ultimate tensile strength for the following categories of steel grades, shown in Figure 1.1b):

- Mild Steels: Interstitial Free (IF), Bake Hardening (BH);
- HSS: High Strength Low Alloy (HSLA);
- AHSS: Dual Phase (DP), TRansformation Induced Plasticity (TRIP), Multi Phase (MP), Martensitic Steels (MS);
- Press Hardening Steels.

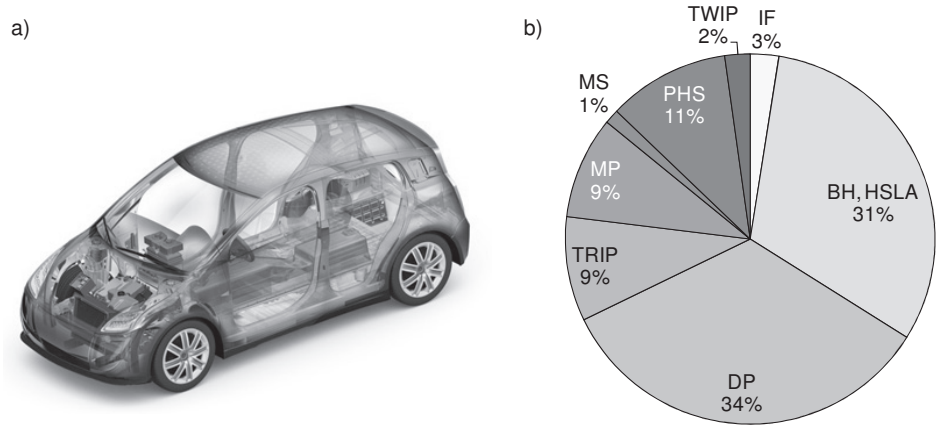

Figure 1.1 a) Picture of the Future Steel Vehicle [1] and b) Pie-chart of the used steel grades.

The increased strength level is a result of precipitation hardening (IF, HSLA), Bake Hardening (BH) through C-diffusion, hardening by multi phase microstructures (DP, TRIP, MP, MS) or press hardening (PHS).

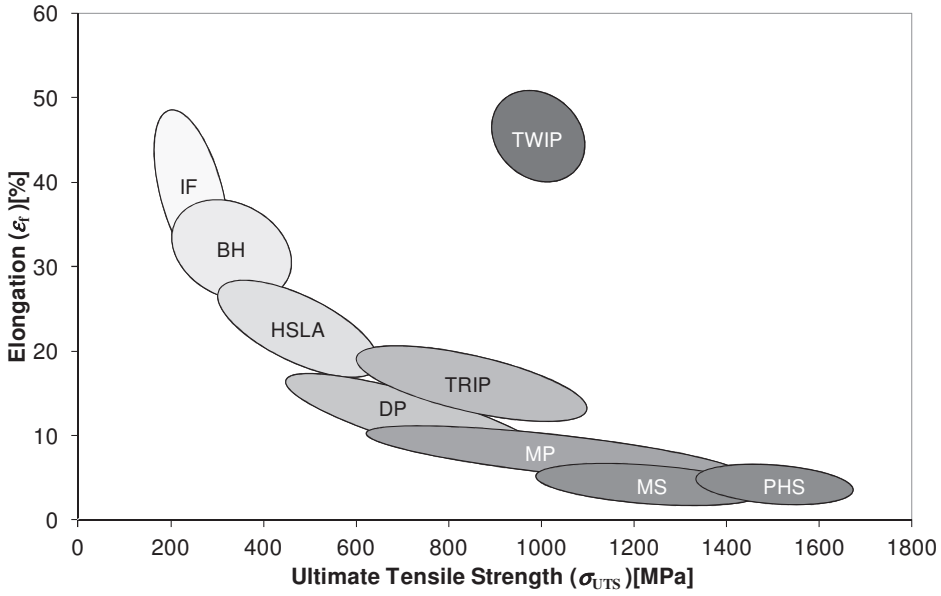

Figure 1.2 Elongation against Ultimate Tensile Strength for Mild Steels, HSS, AHSS and PHS [1].

One of the latest developments in steel grades in the automotive industry is austenitic manganese (Mn)-based TWinning Induced Plasticity (TWIP) steels that combine a high strength with a very high uniform elongation [1, 2] as shown in Figure 1.2. These superior mechanical properties are a result of deformation mechanisms combining slip of dislocations, twinning (TWIP effect) and strain induced martensite transformation (TRIP effect) [3]. The formation of twins and/or strain induced martensite leads to a strongly increased and sustained work-hardening, resulting in very high uniform elongation and high strength [4].

In addition to usual application issues like formability and weldability, a problem encountered with austenitic Mn-based TWIP steels is delayed fracture. This is the phenomenon that even after successful forming, fracture may still occur. The time until fracture can range from seconds to weeks. Figure 1.3 shows an example of delayed fracture after deep drawing. Increased understanding of the phenomenon of delayed fracture would accelerate the introduction of austenitic Mn-based TWIP steels to the automotive industry, enabling further weight reduction and improved safety and fuel economy.

1.1 Phenomenon of delayed fracture

The assessment of delayed fracture in thin sheet material is currently not defined in a universal testing standard. Testing usually comprises deep drawing into a cup with a specific deep drawing ratio (see Figure 1.3a)), and monitoring the appearance of cracks in a specified time frame. Guo et al. [5] observed the delay time to range from seconds to weeks in a stainless steel. Deep drawing is a process where round blanks are formed into cups using press. This is also the main deformation method to be applied in the present research. To accelerate the phenomenon of delayed fracture, more severe and controlled testing conditions can be applied using an active corrosive environment, typically by submerging a deep-drawn sample in water or by H-charging in an electrolytic cell [5]. Figure 1.3 shows an example of delayed fracture after deep drawing. After initiation at the cup edge, the crack advances along the vertical direction and finally proceeds to a length of 19 mm. The top-view image reveals that there are two cracks on opposite sides of the cup. Delayed fracture predominantly occurs close to the transverse direction (TD), i.e. perpendicular to the rolling direction of the original cold rolled sheet. In the course of the delayed fracture process, the shape of the cup edge changes from circular to oval. The two cracks are situated farthermost from one another, drawing up the larger axis of symmetry of the oval.

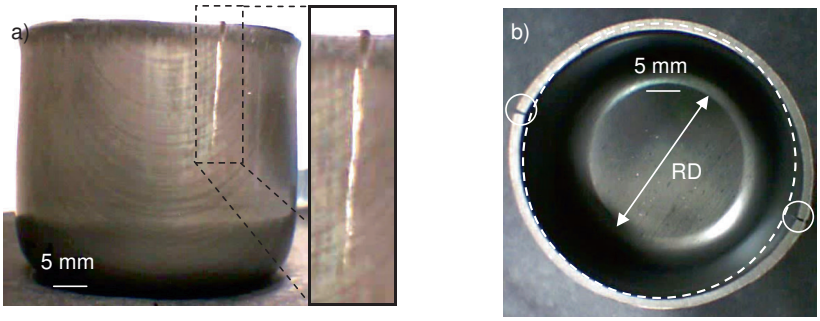

Figure 1.3 a) Side- and b) top-view images of a deep-drawn cup showing delayed fracture. The white-dashed circles indicate the original cup diameter. The white arrows indicate the rolling direction (RD). The white full circles indicate the crack positions.

Most research in the field of delayed fracture has been performed on austenitic stainless steels, like AISI 301 and 304 series [5, 6]. The phenomenon observed in austenitic steels is mainly related to three potential causes: (1) the limited stability of austenite, (2) the residual stress/strain state and (3) the environmental conditions (related to the presence of hydrogen). The first cause - the austenite stability - is associated with the stacking fault energy (SFE). The two other potential causes relate delayed fracture to stress corrosion cracking and hydrogen embrittlement [7]. The combination of hydrogen embrittlement and residual stress strongly influences the behaviour of high strength steels in the presence of water or water vapour.

1.2 Origin and development of austenitic manganese-based steels

Bouaziz [8] and De Cooman [9] gave a comprehensive overview on austenitic Mn-based steels, ranging from the development over the last century to the current knowledge of microstructural effects on the mechanical properties. In 1888, Sir Robert Hadfield invented the first type of Mn-based steels showing very high uniform elongation and high strength [10]. Since then different classes of Mn-based steels have found application as shape memory, damping, seismic-resistant, cryogenic, TRansformation Induced Plasticity and TWinning Induced Plasticity steels [11]. The addition of manganese and carbon is essential to stabilize the austenitic microstructure [12]. Mechanical loading was found to lead to the formation of hard phases which are responsible for the impressive mechanical properties and which were identified as two different kinds of martensite: ε- and α'-martensite [13-14]. The discovery of high work-hardening rate without the transformation to martensite (halfway the 20th century) introduced the mechanism of mechanical twinning [15-17], as confirmed by Transmission Electron Microscopy in the sixties [18-20]. Meanwhile the difficulty of cross slip of dislocations also materialized as the concept responsible for the high strain-hardening [21].

Over time, the composition of Hadfield steels evolved towards higher Mn-contents and lower C-contents. The idea arose that twins function as barriers for dislocation movement based on observed dislocation pile-ups at twin boundaries [22]. Severe twinning at low temperature resulted in excellent mechanical properties, allowing the first cryogenic applications in the '80s [23]. A change in composition moves the temperature region for twinning to room temperature, suitable for application in the automotive industry.

In the automotive industry, the requirements for fuel economy and safety are continuously increasing. Improvements in fuel economy require a lower weight of the vehicle whereas higher standard requirements and improvements in safety often result in additional weight. To resolve this contradiction, the requirements for strength and formability of steel increase continuously. To this purpose, the steel industry develops (A)HSS and PHS. One of the latest developments is fully austenitic Mn-based TWIP steels that combine a high strength with a very high uniform elongation [3]. These superior mechanical properties result from the high work-hardening of these austenitic Mn-based TWIP steels. The main reasons for this high work-hardening are deformation mechanisms combining slip of dislocations with strain induced microtwinning and martensite transformation [3]. The deformation mechanisms relate to the austenite stability and form shear bands like slip bands, twins and/or ε-martensite laths [3], which are obstacles for further dislocation glide, increasing work-hardening. These shear bands divide grains into smaller areas decreasing the dislocation mean free path: the dynamic Hall-Petch effect [9].

1.3 Austenite stability and deformation mechanisms

Figure 1.4 presents the equilibrium Fe-Mn binary phase diagram. A large region of the equilibrium Fe-Mn binary phase diagram has an austenitic phase [24]. At room temperature, the stable microstructure consists of ferrite below 4 wt% Mn, ferrite and austenite from 4 to 28 wt% Mn and austenite between 28 and 53 wt% Mn. Crystal structures like α-, β- and δ-Mn existing at Mn-contents above 53 wt% fall outside the scope of this thesis.

An equilibrium phase diagram does not account for the transformation kinetics, which can result in the presence of metastable phases in the microstructure. Figure 1.5 shows the microstructural phases present in Fe-Mn-C ternary alloys in undeformed condition and after plastic deformation [25]. The martensitic phases are metastable at room temperature after quenching from annealing at 950°C and their presence depends on the Mn- and C-content. A higher Mn- and C-content stabilizes the austenite. At Mn-contents above 10 wt% the metastable martensitic regions increase with plastic deformation due to strain-induced transformation.

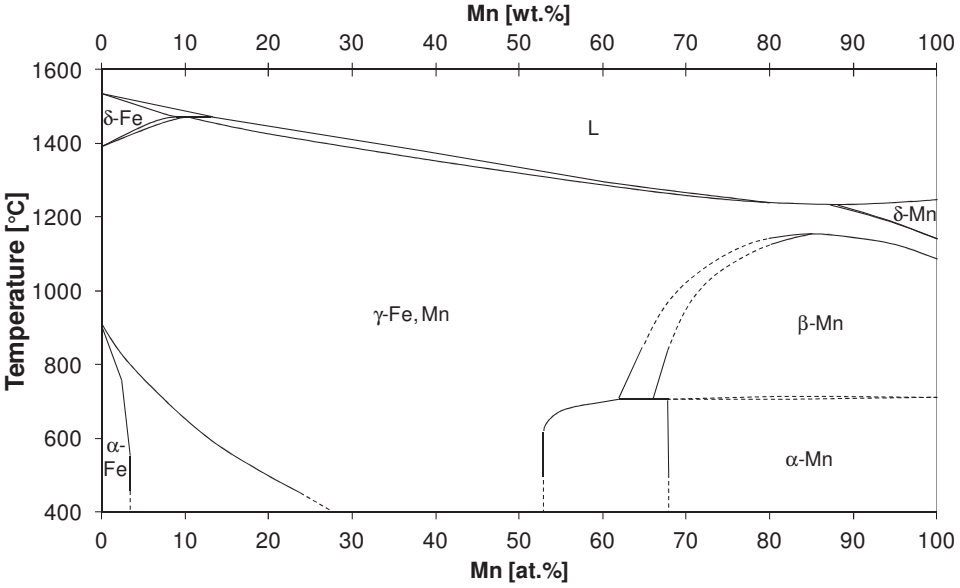

Figure 1.4 Equilibrium binary Fe-Mn phase diagram [24].

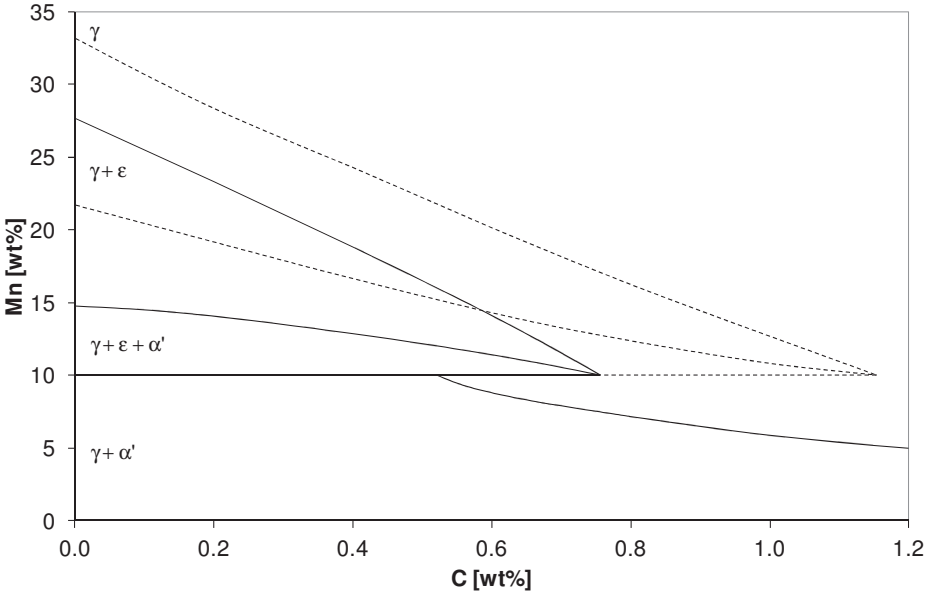

Figure 1.5 Microstructural phases present at room temperature after quenching from annealing at 950°C as a function of Mn- and C-content in undeformed condition and after plastic deformation [25]. The dashed lines indicate the effect of plastic deformation.

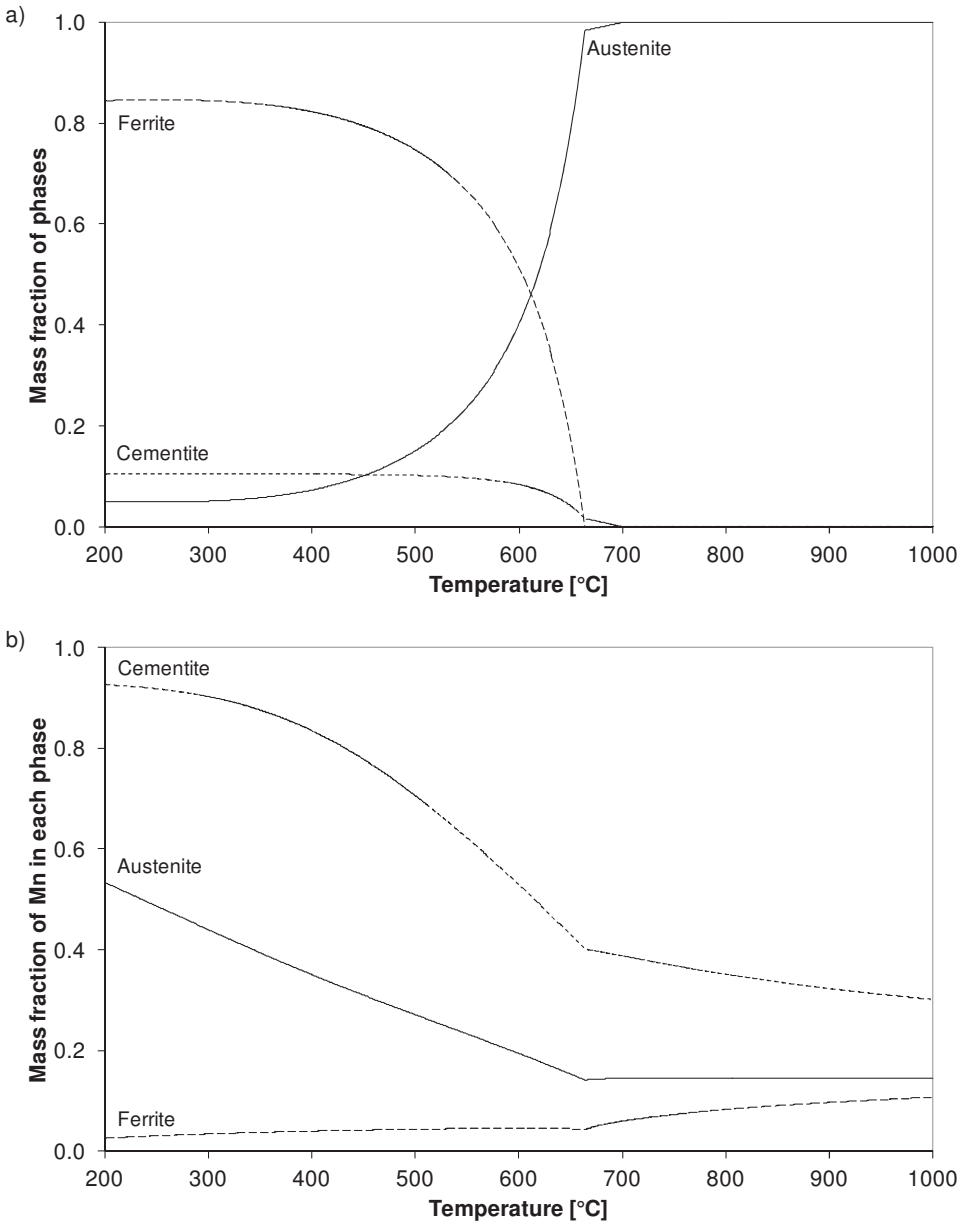

Figure 1.6 a) Equilibrium phase fractions and b) equilibrium Mn-concentration phase compositions in each of the three phases as a function of temperature as calculated by ThermoCalc for one of the Fe-Mn-C-Si-Al grades used in this work, containing 14.55 wt% Mn, 0.71 wt% C, 0.07 wt% Si and 2.93 wt% Al.

Thermodynamic calculations using ThermoCalc software (TCW version 4, TCS Steels/Fe-Alloys database version 6) give the equilibrium phase fractions as a function of temperature for one of the Fe-Mn-C-Si-Al grades used in this work, containing 14.55 wt% Mn, 0.71 wt% C, 0.07 wt% Si and 2.93 wt% Al.

Figure 1.6a) shows the mass fraction of phases in equilibrium as calculated by Thermo-Calc. Above 700°C, the equilibrium microstructure fully consists of austenite. At lower temperatures, ferrite and cementite are present in equilibrium with austenite. Below 400°C, the equilibrium fraction of austenite appears to stabilise at approximately 5%.

Figure 1.6b) shows the Mn-concentration as a function of temperature in the phases ferrite, austenite and cementite, as calculated by Thermo-Calc. The equilibrium Mn-concentration in ferrite does not exceed 5% in the temperature range below 600°C, whereas carbides are strongly enriched in manganese. A strong tendency for Mn-partitioning between ferrite and carbides is therefore expected to occur during the formation of ferrite and carbides from austenite, requiring Mn-diffusion. The diffusion rate of manganese will be of significant importance for the transformation process. Thermocalc calculations also show that the almost 3 wt% Al in the alloy will be subject to partitioning, although to a much lesser extent than manganese (not more than 4% concentration difference between the phases, whereas Figure 1.6b) shows more than 80% difference for manganese). Although the diffusivity of aluminium is slightly lower than that of manganese, due to its much higher content and its much stronger partitioning, manganese is expected to be the dominant alloying element for the phase-transformation kinetics.

The movement of dislocations enables a material to deform plastically. A partial dislocation is a dislocation with a Burgers vector b unequal to the interatomic distance. The glide of a partial dislocation leaves behind an imperfect crystal containing a stacking fault. A stacking fault in Face Centred Cubic (FCC) material is a planar defect on the close packed $\{111\}_\gamma$ planes [26].

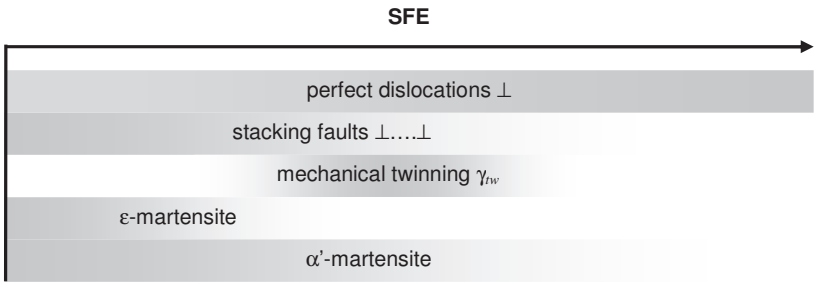

Figure 1.7 Effect of the SFE through composition and temperature on deformation mechanisms, after [27]. The grey scale indicates the presence of the deformation mechanism.

The austenite stability against deformation is related to the Stacking Fault Energy (SFE). The SFE helps to indicate the dominant deformation mechanism during plastic deformation: perfect/partial dislocation glide, twinning, ε-/α'-martensite formation. The SFE depends on the composition and deformation temperature. Manganese, carbon and aluminium increase the SFE, whereas silicon decreases the SFE [24]. Figure 1.7 illustrates the effect of the SFE on the deformation mechanisms. A high SFE leads to the formation of perfect dislocations (or narrow stacking faults). High SFE materials can cross-slip and climb easily, resulting in a rather low strain-hardening. A lower SFE leads to the dissociation of a perfect dislocation into partial dislocations with a stacking fault. Low SFE materials have much more difficulty with cross-slip and climb, increasing work-hardening. The array of stacking faults determines the deformation mechanism at hand: stacking faults, mechanical twinning or ε-martensite. α'-Martensite can form at the intersections of shear bands like slip bands, twins and/or ε-martensite laths [27].

1.3.1 Mechanical twinning

Mechanical twinning is a homogeneous shape deformation of a region of the crystal resulting in a structure identical to the parent structure, but with a different orientation. A twin consists of a crystal with a mirror plane reflection about $\{111\}_\gamma$ or twin boundary. Plastic deformation can induce mechanical twinning in a FCC crystal structure as a consequence of partial dislocation slip on every close packed plane [27] (Figure 1.8).

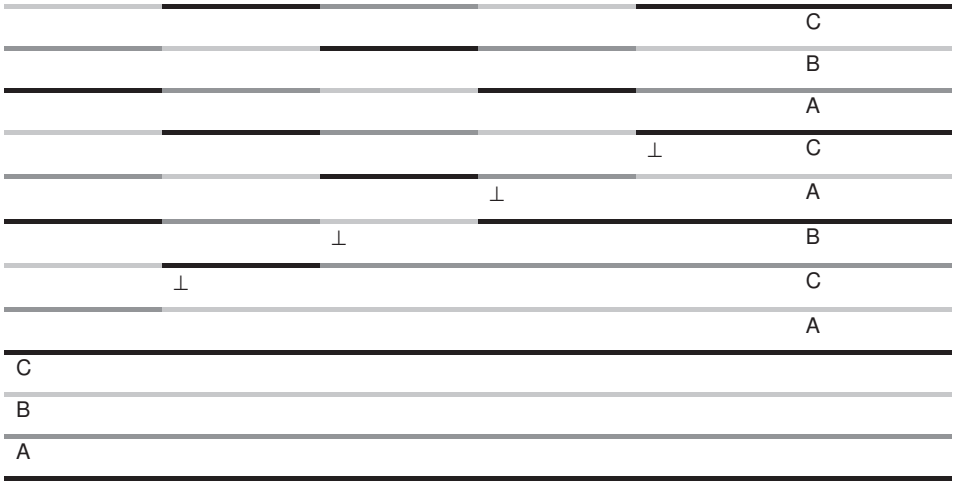

Figure 1.8 Partial dislocation slip on every close packed plane in a FCC crystal structure resulting in the formation of a twinned crystal structure [27].

Figure 1.8 illustrates partial dislocation slip on every close packed plane in a FCC crystal structure, resulting in the formation of a twin. Partial dislocation slip on a close packed plane changes the stacking sequence of the close packed plane from ABC ABC ABC to ABC AC ABC. The slip of four partial dislocations on every close packed plane inverses the initial stacking sequence from ABC ABC ABC to ABC A CBA C ABC, forming a structure identical to the parent structure, but with a different orientation: a twin.

1.3.2 Mechanisms and kinetics of martensitic transformation

Figure 1.9 illustrates partial dislocation slip on every second close packed plane in a FCC crystal structure, resulting in the formation of a HCP crystal structure or ε-martensite. Partial dislocation slip on a close packed plane changes the stacking sequence of the close packed plane from ABC ABC ABC to ABC AB ABC. The slip of several partial dislocations on every second close packed plane changes the initial stacking sequence from ABC ABC to AB AB AB, forming a HCP crystal structure or ε-martensite.

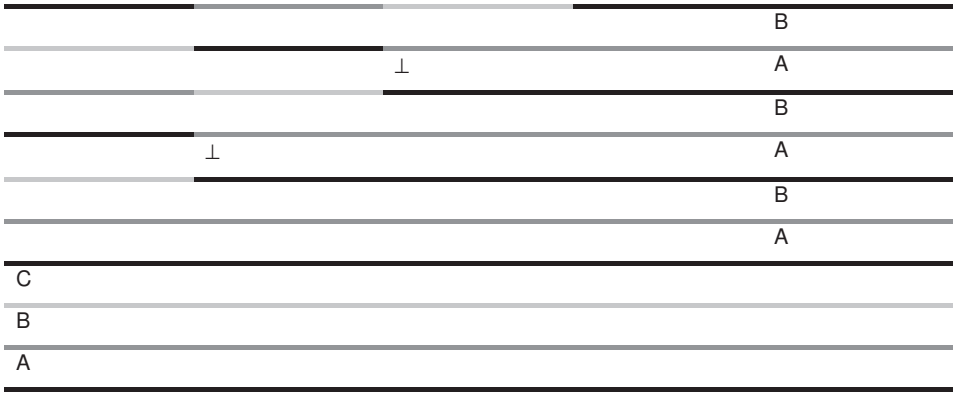

Figure 1.9 Partial dislocation slip on every second close packed plane in a FCC crystal structure resulting in the formation of a HCP crystal structure [27].

α'-Martensite does not form by such a relatively simple slip mechanism, but can form at the intersections of shear bands like slip bands, twins and/or ε-martensite laths [28], due to the high stress concentrations occurring at these intersections [29]. According to Olson and Cohen [28], a low SFE promotes strain-induced nucleation of α'-martensite, without prior formation of ε-martensite. With plastic deformation, the intersected volume can act as very effective nucleation site, allowing the passage of dislocations blocked by bands or laths, inducing the formation of α'-martensite [28] and releasing stress concentrations [29]. It is

worth to note that α'-martensite has a larger volume per atom than austenite, resulting in coherency strains in the austenite.

Figure 1.10 illustrates the possibility for nucleation of α'-martensite at the intersection of two shear bands according to the model developed by Olson and Cohen [28]. This model gives a suitable description of the formation of α'-martensite, but does not give a full explanation of the mechanism of α'-martensite formation. One array consists of one-half FCC twinning shears with $a/6[21\text{-}1]$ partial dislocations every second $\{111\}_\gamma$ plane (denoted as T/2), whereas the other consists of one-third FCC twinning shears with $a/6[211]$ partial dislocations every third $\{111\}_\gamma$ plane (denoted as T/3). Note that T/2 corresponds to the formation of a Hexagonal Close Packed structure, like ε-martensite shown in Figure 1.9. The intersection results in a perfect Body Centred Cubic microstructure.

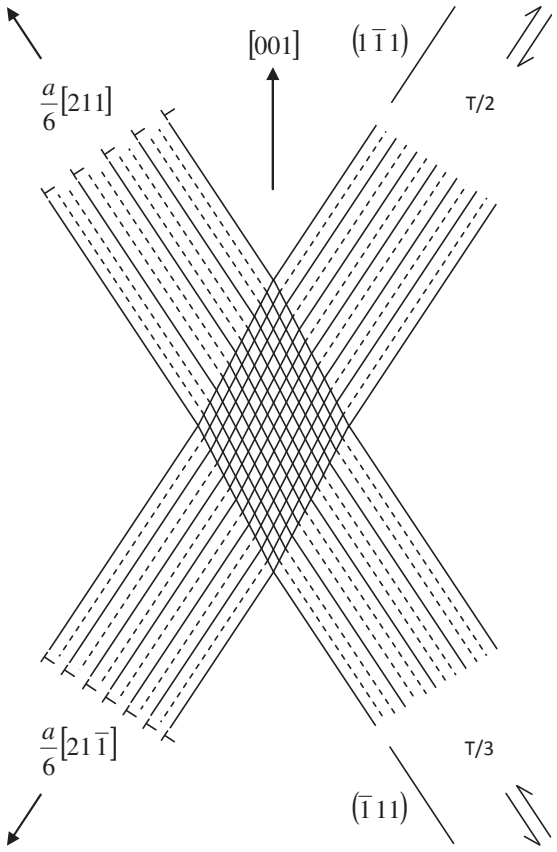

Figure 1.10 Schematic illustration of a shear band intersection for α'-martensite nucleation [28].

Olson and Owen made the following overview of models for deformation induced martensitic transformation as a function of strain [30]. Several approaches are predominantly empirical, resulting in equations like [31, 32]

$$f_{\alpha'} = A \cdot \varepsilon^{B} \cdot f_{\gamma} \tag{1.1}$$

where $f_{\alpha'}$ is the martensite volume fraction, A and B are constants, ε is the strain and f_{γ} is the austenite volume fraction. For stainless steel B is approximately 3. Gerberich [33] suggested

$$f_{\alpha'} = A' \cdot \varepsilon^{1/2} \tag{1.2}$$

Guimaraes [34] observed that the nature of α'-martensite formation as a function of strain changes from initially parabolic to linear. To obtain the sigmoidal behaviour of α'-martensite formation as a function of strain, he proposed

$$f_{\alpha'} = 1 - \exp\left(-k\varepsilon^{z}\right) \tag{1.3}$$

where k and z are constants. For Fe-Ni-C alloys, k and z are 28 and 3.7 respectively. Olson and Cohen [35] introduced a theoretical approach for the transformation kinetics, based on the mechanism for strain-induced nucleation. Their model treats the nucleation kinetics of α'-martensite through the intersection of shear bands as a function of strain and results in

$$f_{\alpha'} = 1 - \exp\left\{-\beta\left[1 - \exp\left(-\alpha \cdot \varepsilon\right)\right]^{n}\right\} \tag{1.4}$$

where α, β and n are constants. α represents the formation of shear bands as a function of strain and is dependent upon temperature through the SFE. β indicates the probability for α'-martensite nucleation at a shear band intersection, which is sensitive to temperature due to the chemical driving force.

1.4 Role of hydrogen

Over the last two decades, the scientific and industrial community dedicated an increasing research effort into austenitic Mn-based steels. The recent interest concentrates on the deformation mechanisms and the relation with crystallographic orientation, work-hardening, and mechanical properties from a conceptual as well as modelling point of view. According to Bouaziz [8], future research efforts should focus on (1) twin volume fraction determination,

(2) the Bauschinger effect, (3) the fundamentals behind twin formation, (4) work-hardening in relation to the C-content, (5) fracture resulting from hydrogen, like stress corrosion cracking, hydrogen embrittlement and delayed fracture and (6) joining to more conventional steels. This thesis concentrates on the stability of the austenitic microstructure against martensitic transformation and diffusional decomposition and its role in the phenomenon of delayed fracture.

The phenomenon of delayed fracture in austenitic Mn-based steels recently received a lot of attention, in particular from Koyama [36-39]. He investigated the effect of different strain rates on delayed fracture and found that a higher strain rate reduces the susceptibility to delayed fracture due to the lower dynamic strain-hardening. The diffusion of carbon influences the hardening mechanism of dynamic strain-hardening and therefore delayed fracture [36]. Besides hydrogen, the diffusion of carbon is also of relevance for delayed fracture.

Another study investigated the introduction of hydrogen into the microstructure [37, 38]. Hydrogen enters the material through diffusion and dislocation activity. The presence of hydrogen affects dislocation slip, reduces the cohesive energy of grain boundaries and promotes mechanical twinning and transformation to martensite, inducing intergranular fracture. Lath-like microstructural features like deformation twins and martensite cause stress concentrations at grain boundaries. Hydrogen-induced mechanical twinning and martensite transformation could result in intergranular fracture [37]. An increasing concentration of mobile hydrogen decreases the fracture stress at which intergranular fracture occurs. The mobile H-content does not affect the work-hardening behaviour. Embrittlement is therefore independent of the H-induced microstructural behavioural change in deformation mechanisms like mechanical twinning and martensite transformation [38].

Other research concentrated on hydrogen cracking at grain and twin boundaries. The observations indicated primarily intergranular fracture and partially transgranular fracture parallel to twin boundaries. Intergranular fracture results from the presence of hydrogen, decreasing grain boundary cohesion. The high stress concentrations occurring at the intersections of primary and secondary twin systems provide crack initiation sites for transgranular fracture. Further crack propagation relates to crystallographic texture. The relation between crack initiation and mechanical twinning is an essential finding, since the superior mechanical properties rely on the deformation mechanisms [11]. Further work on crack initiation showed that cracks initiated at the interception of annealing twin boundaries by strain-induced ε-martensite [39].

Chun [40] also investigated the effect of ε-martensite on the interaction between hydrogen and mechanical properties. Microstructural defects influence the hydrogen embrittlement properties through their interaction with hydrogen as trapping site. Two types

of trapping sites exist, depending on the activation energy for detrapping: (1) mobile trapping sites and (2) non-mobile trapping sites. Mobile traps have a low activation energy for detrapping and comprise grain boundaries, dislocations and coherent carbide interfaces. These traps are responsible for hydrogen embrittlement. Non-mobile traps have a high activation energy for detrapping and consist of inclusions, voids and incoherent carbide interfaces. The introduction of a significant density of non-mobile traps improves the resistance to hydrogen embrittlement. Chun showed that deformation twin boundaries with relatively low coherency function as non-mobile traps, whereas coherent ε-martensite boundaries have a low activation energy for detrapping. Therefore, the presence of ε-martensite increases the susceptibility to hydrogen embrittlement [40].

The stabilization of austenite against martensitic transformations improves the delayed fracture resistance. The BCC microstructure of α'-martensite has a higher H-diffusivity compared to FCC microstructure of austenite. The resistance to delayed fracture further benefits from twinning induced plasticity, providing non-mobile traps in the form of twin boundaries [41].

Other work from Chun investigated the effect of aluminium on the delayed fracture resistance. The microstructural defect morphology resulting from plastic deformation is of critical importance for hydrogen embrittlement, since it provides trapping sites for hydrogen. The addition of aluminium decreases the dislocation density at equal deformation, reducing the number of mobile trapping sites. A higher dislocation density also increases the diffusion rate of hydrogen, further reducing the resistance against delayed fracture [42].

Chin [43] evaluated the deformation mechanisms upon deep drawing in relation to the Al-content. Deep drawing results in an increased twin fraction due to higher strain rates compared to tensile straining. A deep-drawn cup shows highly localized stresses at the inner side of the cup edge. The addition of aluminium increases the SFE, distributing twins more homogenously and lowering stress concentrations [43].

Ronevich [44] focussed on the effects of H-charging on the austenitic microstructure. Due the low diffusivity of hydrogen in austenite a very high H-concentration develops near the surface. This is not observed in a ferritic microstructure due to the higher H-diffusivity. This high hydrogen build-up in FCC can lead to surface cracking [44].

1.5 Scope of thesis

The susceptibility to delayed fracture is a combination of (1) the austenite stability against microstructural defect formation, (2) the internal residual stress and (3) the presence of mobile hydrogen [40]. Most research on delayed fracture concentrates on the role of hydrogen, leaving the austenite stability against defect formation and internal residual stress underexposed. Increasing the austenite stability against microstructural defect formation like

strain-induced transformation improves the resistance against delayed fracture [42]. This work discusses the effect of plastic deformation on the stability of the austenitic microstructure against martensitic transformation and diffusional decomposition and its role in the phenomenon of delayed fracture.

The effect of strain on the microstructural defect morphology has been most intensively investigated for tensile straining [45-48]. The assessment of delayed fracture usually comprises deep drawing. Therefore this work investigates the effect of deep drawing on the generation of structural defects and the austenite stability against strain-induced transformation to α'-martensite. Deep drawing can result in a larger strain path compared to tensile straining, leading to a larger accumulated equivalent strain ($\varepsilon_{eq}{}^{ac}$). The formation of α'-martensite indicates the formation of crack initiation sites, which is discussed as a possible cause of delayed fracture. The martensitic transformation of metastable austenite upon mechanical loading indicates the instability of the austenite which leads to diffusional decomposition of the austenite at intermediate temperatures. The kinetics of austenite decomposition upon reheating and the effect of prior plastic deformation on the kinetics finish this work.

1.6 Outline of thesis

In this thesis, chapter 2 will describe the materials and experimental techniques used throughout this thesis.

Chapter 3 presents an experimental study on the effect of deep drawing on the generation of structural defects in austenitic Mn-based TWIP steels using X-ray diffraction, positron beam Doppler broadening spectroscopy and magnetic measurements. To this purpose, the characteristics of defects were studied along the wall of deep-drawn cups in the transverse direction, representing a gradually changing deformation state.

In chapter 4 the effect of strain on the defect and microstructure evolution in austenitic Mn-based TWIP steels was experimentally investigated using magnetic measurements, X-ray diffraction and positron beam Doppler broadening spectroscopy. The direct formation of α'-martensite from austenite in a deep-drawn austenitic Mn-based TWIP steel with high Stacking Fault Energy was investigated using Transmission Electron Microscopy techniques. The strain evolution during deep drawing was simulated by means of Finite Element Method simulations and a model for α'-martensite volume fraction evolution upon straining is proposed.

Chapter 5 will present the role of α'-martensite in the phenomenon of delayed fracture on austenitic Mn-based TWIP steels after deep drawing, observed by *in-situ* video recording. The formation of α'-martensite indicates the formation of crack initiation sites, which is

discussed as a possible cause of delayed fracture. The transformation of metastable austenite by martensitic mechanisms upon plastic deformation indicates diffusional decomposition of austenite into pearlite in case the material is annealed at temperatures below the A_1-temperature.

Chapter 6 will study this austenite decomposition into pearlite at intermediate temperatures and the effect of prior plastic deformation. The isothermal transformation to pearlite and the role of manganese on the transformation kinetics, in particular Mn-partitioning between pearlitic cementite and ferrite, will be discussed.

Finally, Chapter 7 will finish this thesis with the main conclusions.

2 Materials and experimental

This chapter gives a description of the experimental and simulation techniques extensively used throughout this work. We will present an overview of the materials and deformation modes (deep drawing and tensile straining) studied in this thesis. We will indicate how to determine the examined strain states through Finite Element Method simulations, to calculate the mass fraction of the phases using ThermoCalc and to perform delayed fracture testing. We will explain how direct (Optical, Scanning and Transmission Electron Microscopy) and indirect measurement techniques (magnetic measurements, positron beam Doppler spectroscopy and X-ray diffraction) enable the examination of the microstructure and identification of the defect structure respectively.

2.1 Composition and properties

This work examined three 1.7 mm thick austenitic Fe-Mn-C-Si-Al grades, denoted as A, B and C. The compositions, Stacking Fault Energies (SFEs) and mechanical properties are listed in Table 2.1. The mechanical properties are averaged over three directions, 0°, 45° and 90° to the rolling direction (RD). The SFE was calculated according to the thermodynamical approach proposed by Bleck et al. [49], with empirical correction factors for the Si- (–7 mJ/m^2 per wt% Si) as reported by Gallagher [50] and Al- (+10 mJ/m^2 per wt% Al) content by Oh et al. [51]. Note that the calculated values are expected to be accurate within 10 mJ/m^2 and thus the grades represent a decrease of SFE in the sequence A-B-C.

Table 2.1 Compositions, stacking fault energies (SFEs) and mechanical properties.

Grade	C	Si	Mn	Al	SFE	$\sigma_{0.2}$	σ_{UTS}	ε_{UTS}	ε_f
	[wt%]	[wt%]	[wt%]	[wt%]	[mJ/m^2]	[MPa]	[MPa]	[%]	[%]
A	0.71	0.07	14.55	2.93	52	508	875	42.1	45.9
B	0.69	0.06	14.44	1.41	42	447	959	56.0	61.0
C	0.69	2.69	15.80	2.35	22	645	1028	41.9	45.5

The three grades were produced via a semi-industrial process route, starting from ingots. The investigated materials were in a recrystallised condition after cold rolling. Further information on the processing of the grades is confidential. Tensile straining was performed at room temperature according to the Euro-norm, using standard A80 tensile samples and a Zwick tensile tester. 10% Tensile deformation is small enough to avoid recrystallisation of the austenite in the applied heat treatments at 500°C, 550°C and 600°C.

2.2 Delayed fracture testing

The assessment of delayed fracture in thin sheet material is currently not defined in a universal testing standard. Testing usually comprises deep drawing with a specific deep drawing ratio and monitoring the appearance of cracks in a specified time frame. The insert in Table 2.2 shows a deep-drawn cup.

2.2.1 Deep drawing

The materials were cut into round blanks with a diameter of 102.5 mm (D_b) using water jet cutting technology. The blanks were formed into cups on an Erichsen press, using a punch with a diameter D_p of 50 mm. This resulted in a deep drawing ratio ($R_{dd} = D_b/D_p$) of 2.05. Other relevant deep drawing parameters are shown in Table 2.2.

Table 2.2 Deep drawing parameters.

Blank holder force [kN]	20-30	Die diameter [mm]	54.8
Speed [mm/s]	1.5	Die edge radius [mm]	6.0
Punch diameter [mm]	50	Lubrication	Teflon foil
Punch edge radius [mm]	7.5	Temperature [°C]	20

Figure 2.1 shows an example of a deep-drawn cup. The deep-drawn cups were examined as a function of the position from the cup bottom primarily in the transverse direction (TD) that was originally perpendicular to the sheet RD, the RD and along the circumference of the cup at 35 mm from the cup bottom.

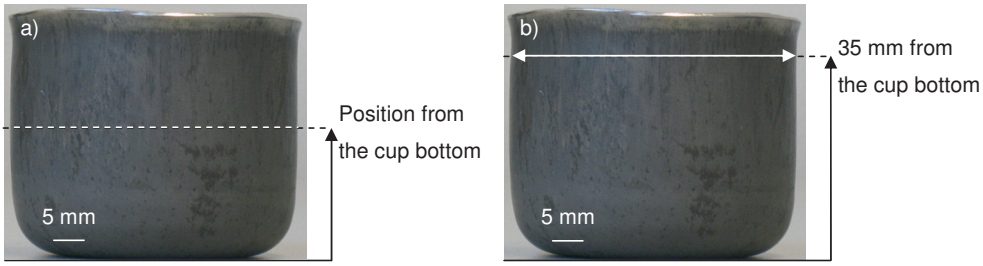

Figure 2.1 Example a deep-drawn cup indicating the position a) from the cup bottom and b) along the circumference of the cup at 35 mm from the cup bottom.

2.2.2 Finite Element Method simulations

Finite Element Method (FEM) simulations were performed to calculate the true local major and minor strain resulting from deep drawing and tensile straining, using the Bergström-Van Liempt hardening rule and Vegter yield locus [52] optimised for conventional steel grades. Pam-Stamp 2G calculations were carried out with the deep drawing parameters given in Table 2.2 and the material input parameters given in Table 2.1. Figure 2.2 shows the strain paths in terms of ε_1, the major true strain in axial direction, and ε_2, the minor true strain in tangential direction, for different degrees of tensile straining and deep drawing at the outside, centre and inside of the cup at 10 mm and at 35 mm from the cup bottom. ε_3 along the cup thickness in radial direction is related to ε_1 and ε_2 according to the constraint

$$\varepsilon_1 + \varepsilon_2 + \varepsilon_3 = 0 \qquad (2.1)$$

With the use of Equation (2.1) the accumulated equivalent strain ($\varepsilon_{eq}{}^{ac}$), which will be used in this thesis as the characteristic strain parameter, is given by [52]

$$\varepsilon_{eq}{}^{ac} = \sqrt{4/3} \cdot \int_0^{\varepsilon} \sqrt{1+\rho+\rho^2}\, d\varepsilon_1 \,,\ \rho = \frac{d\varepsilon_2}{d\varepsilon_1} \tag{2.2}$$

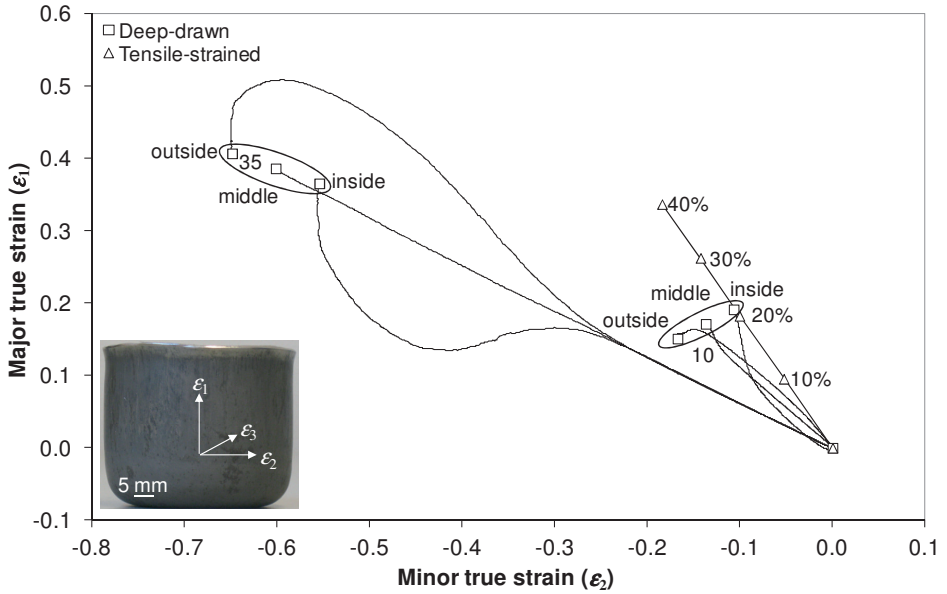

Figure 2.2 Strain paths for tensile straining and deep drawing at 10 and 35 mm from the cup bottom at the inside, middle and outside of the cup. The tensile strain (in %) and the position from the deep-drawn cup bottom (in mm) are indicated. The inset shows an example of a deep-drawn cup and the directions of ε_1 (axial direction), ε_2 (tangential direction) and ε_3 (radial direction).

In addition, values for the cup wall thickness as a function of the position along the wall height are obtained. Figure 2.3 shows the effect of deep drawing on the cup wall thickness, both experimentally and according to the FEM simulation. The thickness, normalized with respect to the original blank thickness (1.7 mm), is plotted as a function of the position from the cup bottom. At the lower part of the cup the material is slightly thinner than the original blank. From approximately 25 mm from the cup bottom, the wall of the cup becomes increasingly thicker due to the compression effect of deep drawing.

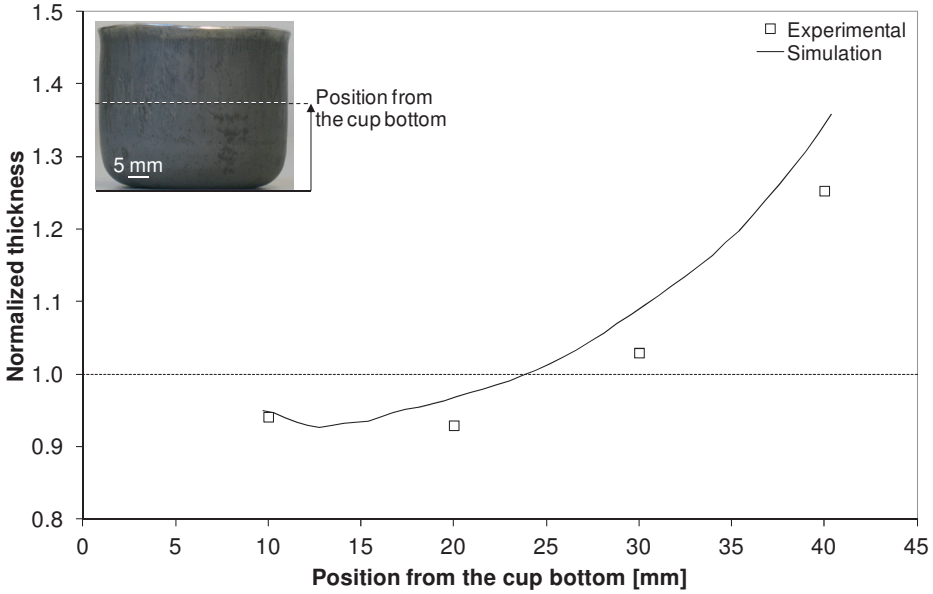

Figure 2.3 The effect of deep drawing on the cup wall thickness, experimentally and according to the FEM simulation. The normalized thickness is plotted as a function of the position from the cup bottom. The inset shows an example of a deep-drawn cup.

The delayed-fracture experiments were performed at room temperature in air for 1680 hours (70 days) and in stagnant tap water for 504 hours (21 days) after deep drawing. Crack initiation was awaited and the crack length and number of cracks was monitored at different time intervals by visual inspection and determined by the average of three simultaneously assessed cups of identical condition. The specimens submersed in stagnant tap water were temporarily taken out of the water for visual inspection. The *in-situ* development of delayed fracture of a cup of grade B was recorded on video.

2.3 Magnetometry

For the magnetization experiments approximately cubic samples with a size of approximately 2 mm × 2 mm × t, where t is the local thickness, were machined from the sheet material, deep-drawn cups and tensile-strained specimens using an electro-discharging machine. The deep-drawn cups were examined as a function of the position from the cup bottom, starting at 10 mm from the cup bottom up to 40 mm with 5 mm intervals. The samples were taken along the cup wall primarily in the transverse direction (TD) that was originally perpendicular to the sheet rolling direction (RD), the RD and along the circumference of the cup at 35 mm from the cup bottom with 30° intervals to the angle with the RD. At 35 mm from the cup

bottom in the TD, a sample was cut into two pieces using an electro-discharging machine: one sample was taken from the inner side of the cup, another sample was taken from the outer side of the cup. The magnetic measurements were performed with a Lake Shore 7307 Vibrating Sample Magnetometer, which includes a furnace for experiments at elevated temperature (See Figure 2.4).

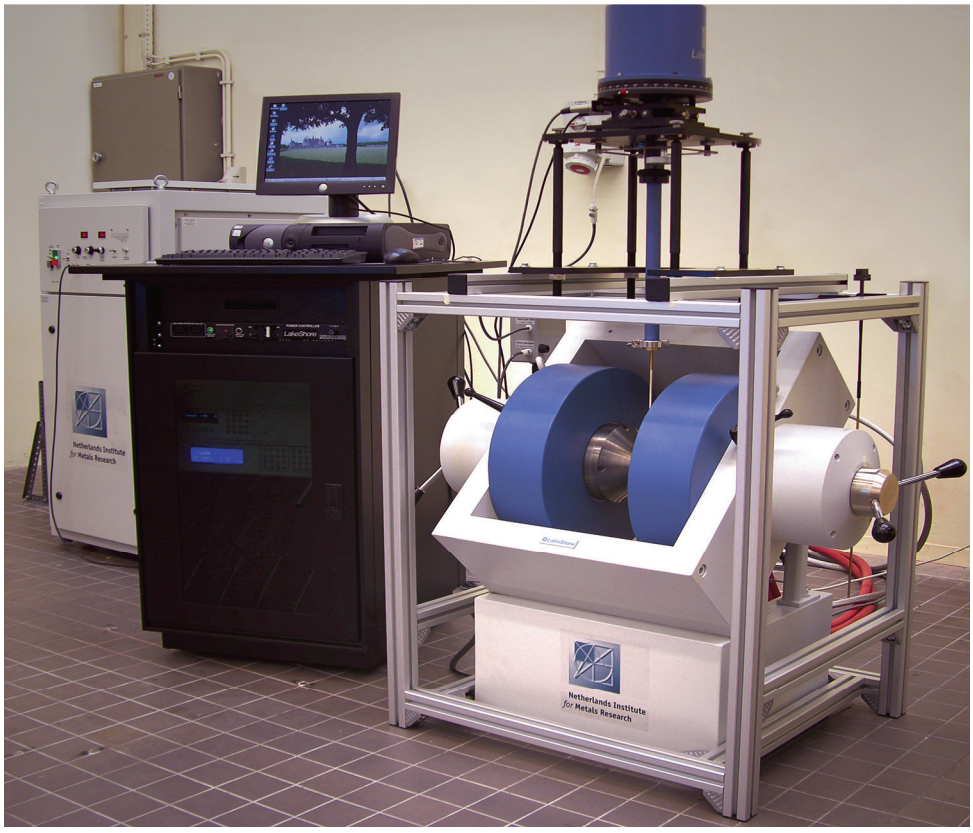

Figure 2.4 Lake Shore 7307 Vibrating Sample Magnetometer.

Before the experiments the Vibrating Sample Magnetometer was calibrated with a standard NIST nickel specimen. Two types of experiments were performed: *in-situ* thermo-magnetic experiments at 500°C, 550°C and 600°C in a magnetic field of 1.0 Tesla, which is high enough to reach the saturation magnetisation [53]. Secondly, *ex-situ* measurements of magnetic hysteresis curves were performed at room temperature, varying the magnetic field from –1.5 Tesla to +1.5 Tesla. Figure 2.5 shows an example of a magnetic hysteresis curve.

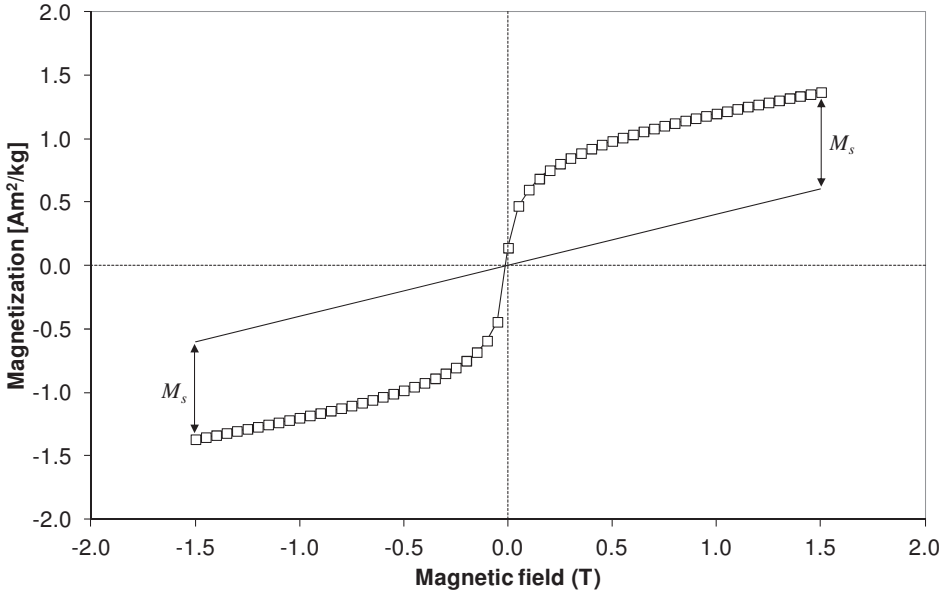

Figure 2.5 Example of a magnetic hysteresis curve measurement varying the magnetic field from −1.5 Tesla to +1.5 Tesla.

The fraction of ferromagnetic phases in the microstructure is derived from the saturation magnetisation by [54]

$$f(\alpha') = \frac{M_s}{x_{Fe} M_{s,Fe}}, \tag{2.3}$$

where M_s is the sample magnetization, calculated from the measured magnetization of the sample minus the contribution of the paramagnetic austenite. The quantity $M_{s,Fe}$ is the saturation magnetization of pure iron at room temperature, which was determined in a separate measurement being 215 Am^2/kg and x_{Fe} represents the atomic fraction of iron in the material. In case of low fractions, the difference between weight and volume fractions can be considered negligible due to the small difference in density between austenite, α'-martensite and pearlite.

The magnetic flux density of the deep-drawn cup at the appropriate positions from the cup bottom was examined with a Gauss meter (RFL Model 912 Gaussmeter, Dowty RFL Industries Inc.) in the radial, axial and tangential plane.

2.4 Positron beam Doppler broadening spectroscopy

The deep-drawn and the tensile-strained samples of grade A were subjected to positron beam Doppler broadening spectroscopy, performed with the Delft Variable Energy Positron (VEP) beam [55]. Four cup conditions were investigated: (i) deep-drawn; (ii) deep-drawn and subsequently annealed in a hot-air furnace for 15 minutes at 400°C; (iii) deep-drawn and subsequently electrolytically hydrogen charged at a current density of 33 A/m^2 for 300 seconds; (iv) deep-drawn, subsequently annealed similar to condition (ii) and electrolytically hydrogen charged similar to condition (iii). Annealing was performed at 400°C for 15 minutes to relieve the residual stresses.

Figure 2.6 gives a schematic illustration of positron beam Doppler broadening spectroscopy. Positrons emitted from a ^{22}Na source are - after moderation to thermal energy and subsequent controlled acceleration - injected in the samples with a kinetic energy of 25 keV. In steels with a density of 7800 kg/m^3, the implantation energy of 25 keV corresponds to an implantation depth of approximately 1 μm. The beam intensity is 10^4 positrons per second and the beam diameter at target is about 8 mm. Note that the deep-drawn samples refer to a complete cup and the tensile-strained samples to the section at the centre of the tensile bar. After having slowed down to thermal energy, each positron eventually annihilates with an electron in the material. The electron involved can either be a relatively free valence electron or a relatively strongly bound core electron. Because of conservation of energy and momentum, the annihilation results in the emission of two annihilation γ-quanta with an energy of about 511 keV each, emitted in (nearly) opposite directions. The positive or negative momentum component of the electron in the direction of the γ-emission ($p_{//}$) Doppler shifts the measured γ-energy by

$$\Delta E = \tfrac{1}{2} c p_{//} \qquad (2.4)$$

with c the speed of light. Here we have neglected the contribution of the positron to the momentum of the annihilating pair. In an annihilation γ-spectrum these shifts lead to a broadening of the 511 keV photo peak. This broadening is quantified by the specific line-shape parameters S and W. The S (sharpness)-parameter is calculated as the ratio of the counts registered in a fixed central momentum window ($|p_{//}| < 3.5 \times 10^{-3}\ m_0 c$, with m_0 the mass of the electron) to the total number of counts in the photo peak, see Figure 2.7. This choice of the momentum window makes the S-parameter sensitive to annihilation with low-momentum valence electrons. Similarly, the W (wing)-parameter is obtained from the high-momentum regions ($1.0 \times 10^{-2}\ m_0 c < |p_{//}| < 2.6 \times 10^{-2}\ m_0 c$) and accounts for annihilation with high-momentum core electrons.

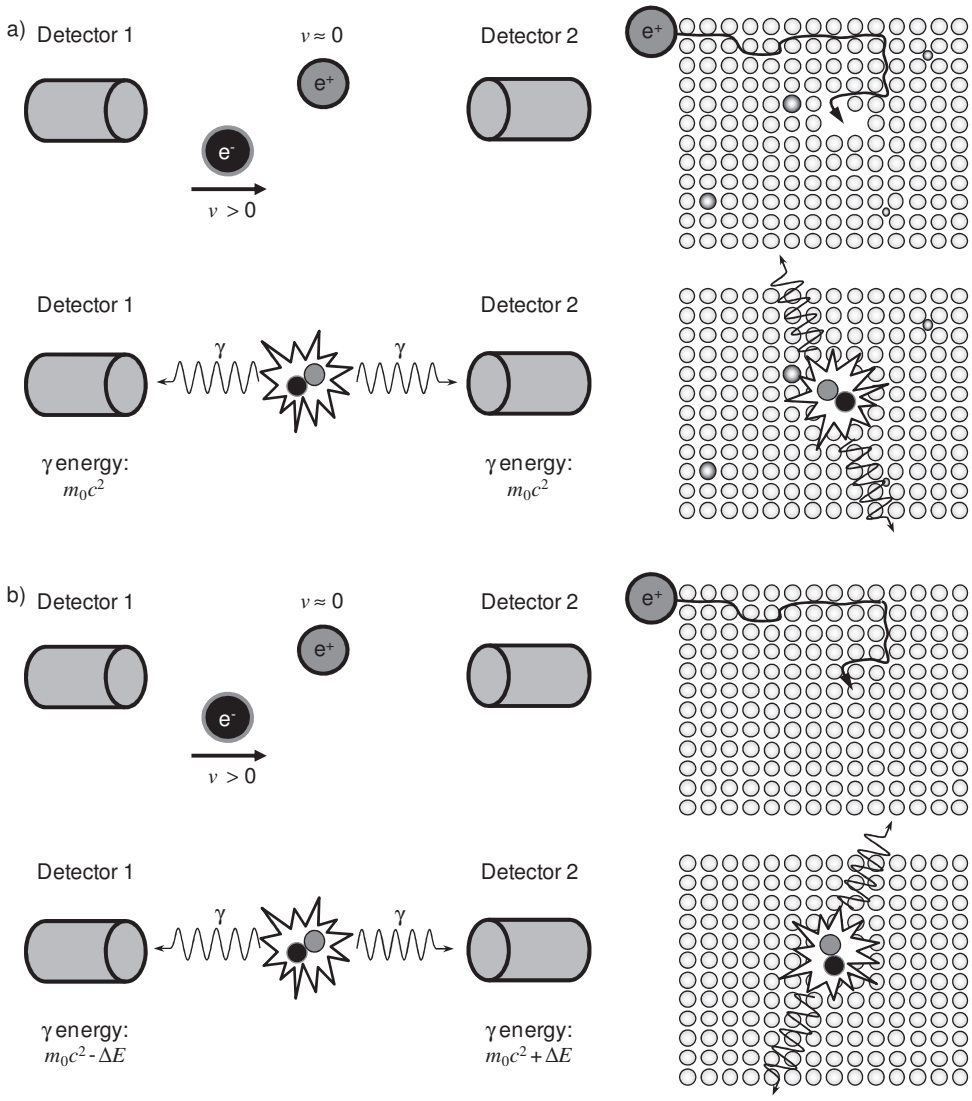

Figure 2.6 Positrons are injected in the samples. After having slowed down to thermal energy, each positron eventually annihilates with an electron in the material. The electron involved can either be a relatively a) free low-momentum valence electron or b) strongly bound high-momentum core electron. Because of conservation of energy and momentum, the annihilation results in the emission of two annihilation γ-quanta with an energy of about 511 keV each, emitted in (nearly) opposite directions. In general, for a positron trapped in a defect (such as a dislocation, a vacancy or vacancy cluster), the probability of annihilation with strongly bound high-momentum core electrons is reduced compared to that for free low-momentum valence electrons.

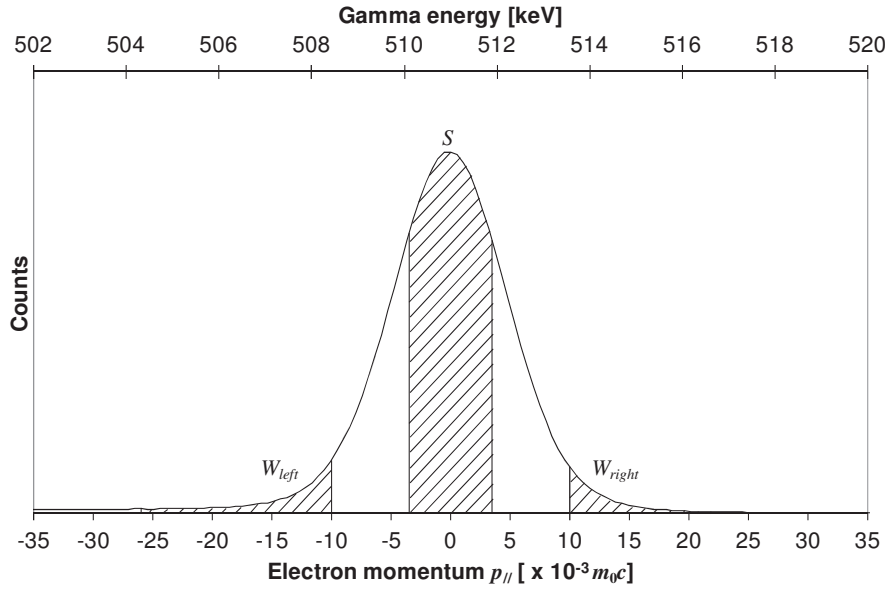

Figure 2.7 The annihilation γ spectrum around the 511 keV photo peak. The specific line-shape parameters S and W are calculated as the ratio's of the counts registered in a fixed central momentum window (S: $|p_{//}| < 3.5 \times 10^{-3}\ m_0c$) or from the high-momentum regions (W: $10 \times 10^{-3}\ m_0c < |p_{//}| < 26 \times 10^{-3}\ m_0c$) to the total number of counts in the photo peak, indicated by the arced areas.

In general, for a positron trapped in a defect (such as a dislocation, a vacancy or vacancy cluster), the probability of annihilation with core electrons is reduced compared to that for valence electrons, resulting in a higher S-parameter and a lower W-parameter value. In case several different types of defects are present the measured S-parameter is

$$S = \left(1 - \sum_{i=1}^{k} \eta_i\right) \cdot S_b + \sum_{i=1}^{k} \eta_i \cdot S_{di} \qquad (2.5)$$

as proposed by [56], where η_i is the fraction of positrons trapped and subsequently annihilated in defects of type i, k is the total number of defect types and S_b and S_{di} are the bulk and defect-specific S-parameters. Equation (2.5) can be defined in an analogous manner for the W-parameter.

The examined positions corresponded to the centre of the positron beam. Three Doppler broadening spectra were obtained for each position to check the reproducibility. This accounted for a minimum of 3×10^6 registered positron annihilations per position.

2.5 Microscopy

2.5.1 Optical Microscopy

The samples for optical microscopy were mechanically polished and electro-polished, followed by electro-etching. Optical bright-field images were taken on a Polyvar microscope. A matrix of 4(x) × 5(y) fields was scanned with a motorized stage, resulting in a total scanned area of 2.6 × 2.4 mm^2. The area fractions were determined by Leica QWin Pro (version V3.5.1) automatic quantitative image analysis software in combination with QUIPS (Quantimet Interactive Programming System). The minimum feature area was 1 µm^2, no maximum feature area was set. An in-house routine was used to determine the area fraction.

2.5.2 Scanning Electron Microscopy

Scanning Electron Microscopy (SEM) was performed on a Zeiss Ultra 55 Field Emission Gun Scanning Electron Microscope to characterize the microstructure. The microscope was equipped with an in-lens electron optic system. Specimens were mounted in Polyfast resin, which was electrically conductive with low emission in the vacuum chamber during examination. All micrographs were obtained using a beam of 15 keV electrons. Figure 2.8 shows the microstructure in the undeformed condition and after deep drawing taken at 20 and 40 mm from the cup bottom. The undeformed microstructure is fully recrystallised, with an equi-axial austenite grain size of about 5 µm. Upon straining, micro shear bands appear in some of the grains. It is believed that the majority of these bands are microtwins, even though a more detailed, diffraction-based study is required to prove this. At 20 mm from the cup bottom the microstructure is dominated by primary shear bands (Figure 2.8b)). At very high strains (Figure 2.8c)), clear distinction between individual shear bands is no longer possible.

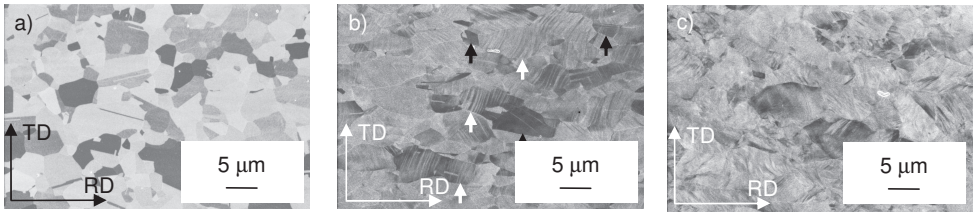

Figure 2.8 Scanning Electron Micrographs: a) prior to deep drawing, b) deep-drawn at 20 mm and c) deep-drawn at 40 mm from the cup bottom. The white thin arrows indicate the TD and RD. The white thick arrows indicate grains with typical shear bands. The black arrows indicate grains essentially without shear bands.

2.5.3 Transmission Electron Microscopy

Transmission Electron Microscopy (TEM) was carried out on a JEOL JEM-2100F transmission electron microscope operating at 200 kV to verify the presence of α'-martensite in the microstructure by electron diffraction. Focus Ion Beam was performed on a FEI Company Quanta 3D FEG to prepare the TEM sample at the position with the highest accumulated equivalent strain, 35 mm from the cup bottom at the inner side of the deep-drawn cup in TD, indicated by the white circle (Figure 2.9). The accumulated equivalent strain was determined by FEM simulations of the cup deep drawing process [57].

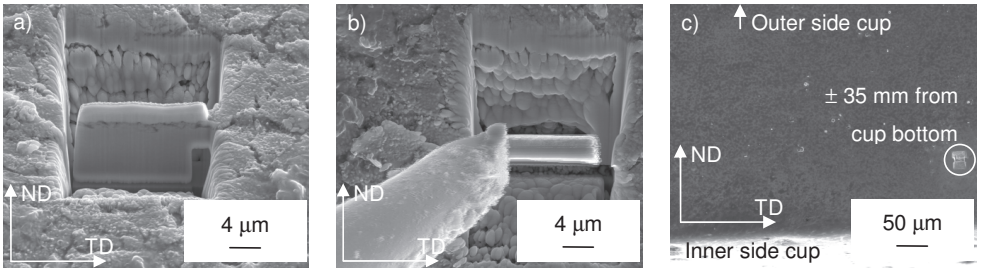

Figure 2.9 Focus Ion Beam: a) cutting and b) removal of the TEM sample from the cross-section c) at the inner side of the deep-drawn cup at 35 mm from the cup bottom in TD, indicated by the white circle.

2.6 X-ray diffraction

X-ray diffraction was performed using a Bruker-AXS D8 Discover diffractometer with Eulerian cradle. CoKα-radiation was used for conventional θ-2θ scans. The diffraction patterns were recorded using a step size of 0.02° in 2θ and the intensity was evaluated by DIFFRAC^{plus} BASIC Evaluation Package 14. The XRD line broadening was determined by the integral breadth of the $\{111\}_\gamma$ reflection.

3 Effect of deep drawing on the generation of structural defects

X-ray diffraction (XRD), positron annihilation Doppler broadening spectroscopy and magnetic measurements have been used to investigate the effect of deep drawing on the generation of structural defects in austenitic manganese-based TWinning Induced Plasticity steels. The effect of plastic deformation and hydrogen on structural defects in austenitic manganese-based TWinning Induced Plasticity steels has not extensively been investigated, leaving the understanding of the effect of the deformation mechanisms involving twinning or plasticity-induced transformation on the structural defects incomplete. XRD measurements show an initial increase in defect concentration with increasing equivalent strain. Positron annihilation Doppler broadening revealed the existence of two defect types, with a different degree of open volume. The interpretation in terms of dislocations, stacking faults and/or twins corroborated with the line broadening results from XRD measurements. Magnetization measurements revealed the formation of α'-martensite, which was related to the fraction of positrons annihilating at the smaller structural defects. The presented findings attribute the larger defect type to perfect dislocations, whereas the smaller defect type is attributed to partial dislocations, and is consequently related to twinning or plasticity-induced transformation.

3.1 Introduction

In this chapter, X-ray diffraction (XRD), positron annihilation Doppler broadening spectroscopy and magnetic measurements were used for an experimental study on the effect of plastic deformation on the generation of structural defects in austenitic manganese (Mn)-based TWinning Induced Plasticity (TWIP) steels. To this purpose, the characteristics of defects were studied along the wall of deep-drawn cups, representing a gradually changing deformation state.

Plastic deformation increases the susceptibility to hydrogen embrittlement due to the formation of structural defects, such as dislocations and vacancies [58, 59]. This interaction has often been related to the phenomenon of delayed fracture [59]. Research on the joint action of hydrogen and defects in metals has been carried out experimentally and theoretically [60, 61]. Still, the direct observation of defects remains difficult, impelling the use of indirect measurement techniques with XRD the most commonly used one. This technique is based on the fact that stress fields around defects, in particular dislocations, distort the lattice and produce line broadening [62]. Positron annihilation Doppler broadening spectroscopy is a more sophisticated indirect technique capable of distinguishing between different open volume defect types. Several positron annihilation studies [63, 64] investigated the effects of plastic deformation, annealing and hydrogen on the structural defects in metals. However, in austenitic Mn-based TWIP steels these effects have not been investigated extensively, leaving the understanding of the effect of the deformation mechanisms involving twinning or plasticity-induced transformation on the structural defects incomplete.

3.2 Characterization of defects

3.2.1 Line broadening

Figure 3.1 shows the integral breadth of the $\{111\}_\gamma$ reflection as a function of the position from the cup bottom. For each examined position, the appropriate equivalent strain resulting from the Finite Element Method (FEM) simulations is given along the horizontal axis. In the XRD-data all observed reflections showed the same trend, so, for clarity only the data for the $\{111\}_\gamma$ reflection is plotted. With increasing strain the deep-drawn sample shows an initial increase in integral breadth, followed by a small decrease.

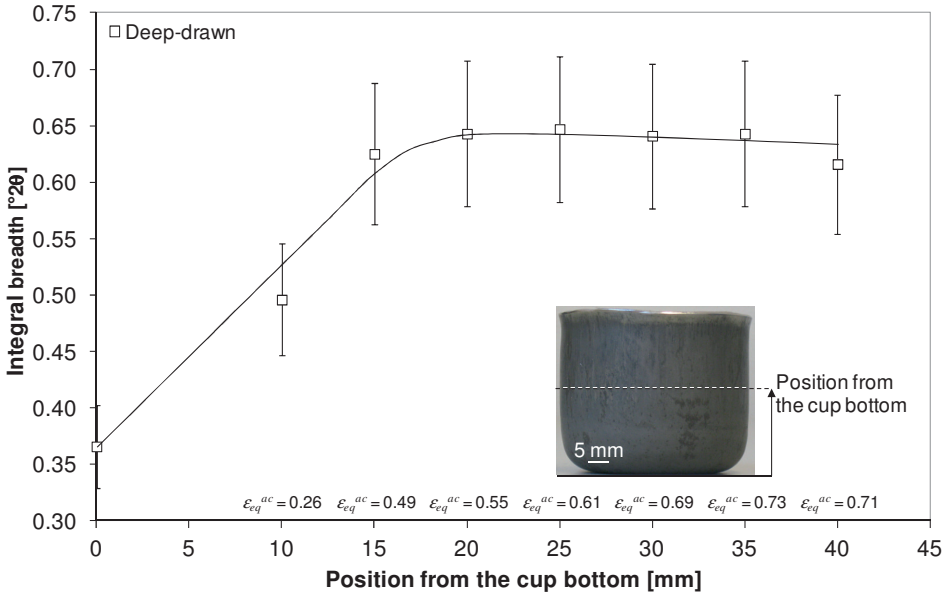

Figure 3.1 The integral breadth of the $\{111\}_\gamma$ reflection as a function of the position from the cup bottom and the appropriate equivalent strain derived from the FEM simulation. The drawn line is to guide the eye.

3.2.2 Line-shape parameters

Figure 3.2 shows the normalized S- and W-parameters as a function of the position from the cup bottom. The normalization is with respect to the reference state of the material, which was accomplished by annealing during 1 hour at 800°C to minimize the defect concentrations. For each examined position, the appropriate equivalent strain resulting from the FEM simulations is given along the horizontal axis. With increasing strain all results show an initial increase in S-parameter, followed by a small decrease for non-annealed cups. The W-parameter shows an initial decrease with increasing strain for all results and eventual saturation for the non-annealed cups. The fraction of positrons trapped and annihilated at defects increases as a result of deep drawing and to a lesser degree from H-charging. Annealing decreases the concentration of defects, thereby lowering the fraction of trapped positrons. As a result the material approaches the low defect concentrations of the reference state at 10 mm from the cup bottom, whereas at higher equivalent strains the applied annealing treatment is not sufficient to fully remove the deformation-induced structural defects. Given the lower fraction of trapped positrons after annealing, the effect of hydrogen is more pronounced.

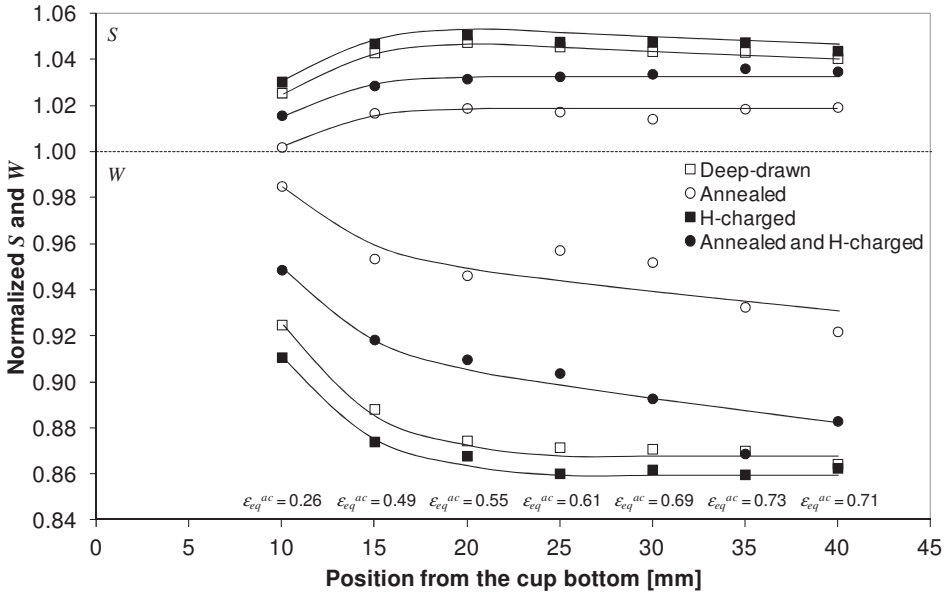

Figure 3.2 The S- and W-parameter as a function of the position from the cup bottom and the appropriate equivalent strain derived from the FEM simulation. The error is approximately the size of the symbols. The drawn lines are to guide the eye.

Figure 3.3 shows the effect of annealing and/or H-charging on the combined *W*-*S*-characteristics as a function of the position from the cup bottom. Starting from reference point R, all curves initially (that is, for low cup heights) are close to the line connecting the points R and D_1. In literature, gradients dW/dS similar to the slope of the line R-D_1 are attributed to the formation of dislocations or vacancy-type defects [65, 66]. With increasing deformation along the cup wall, the W-S-characteristics start to deviate from the line R-D_1. The observed trends for the different cups converge in a second specific point D_2 in the W-S-map. The observed change in slope indicates the development of a different (as seen by the positrons) type of defect along the cup wall. Since the normalized S-values are much smaller than those reported for vacancy type defects [65, 66], both defect types can be associated with dislocations, with the defect type related to point D_2 having the smaller volume as follows from its lower S-value.

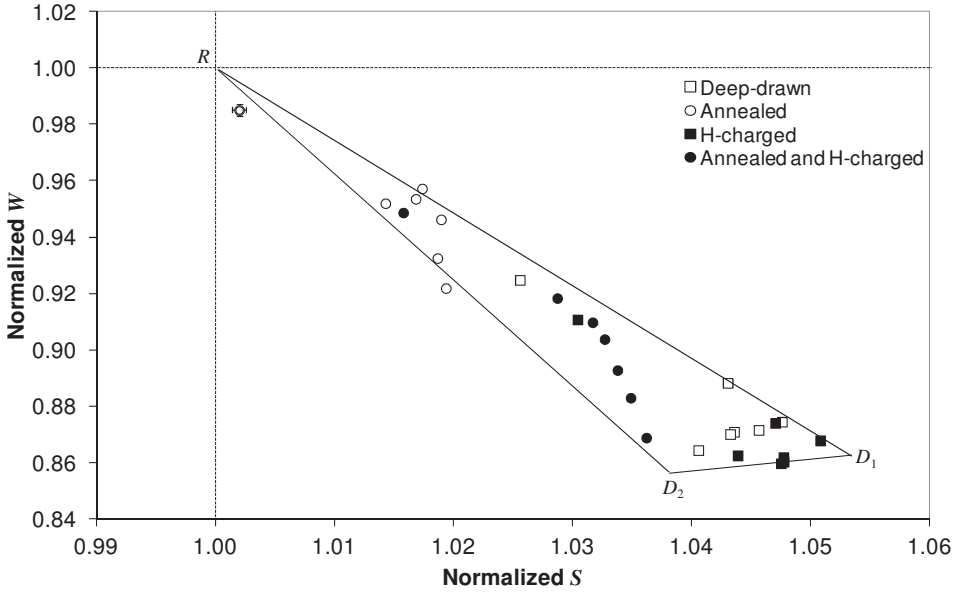

Figure 3.3 *W-S* map for austenitic Mn-based TWIP steel cups as a function of the position from the cup-bottom.

3.2.3 Trapping fractions

Using Equation (2.5), the trapping fractions η_1 *and* η_2 have been calculated, assuming two defect trapping states with characteristic *S-W* values S_1 = 1.052, W_1 = 0.870 for defect D_1 and S_2 = 1.037, W_2 = 0.860 for defect D_2. The result is given in Figure 3.4 as a function of the position from the cup bottom. It is observed that for deformation to relatively low strain levels η_1 initially increases as a function of the position from the cup bottom. For cup heights above 25 mm, positron trapping at the second defect type D_2 starts to increase at the expense of trapping at defect D_1.

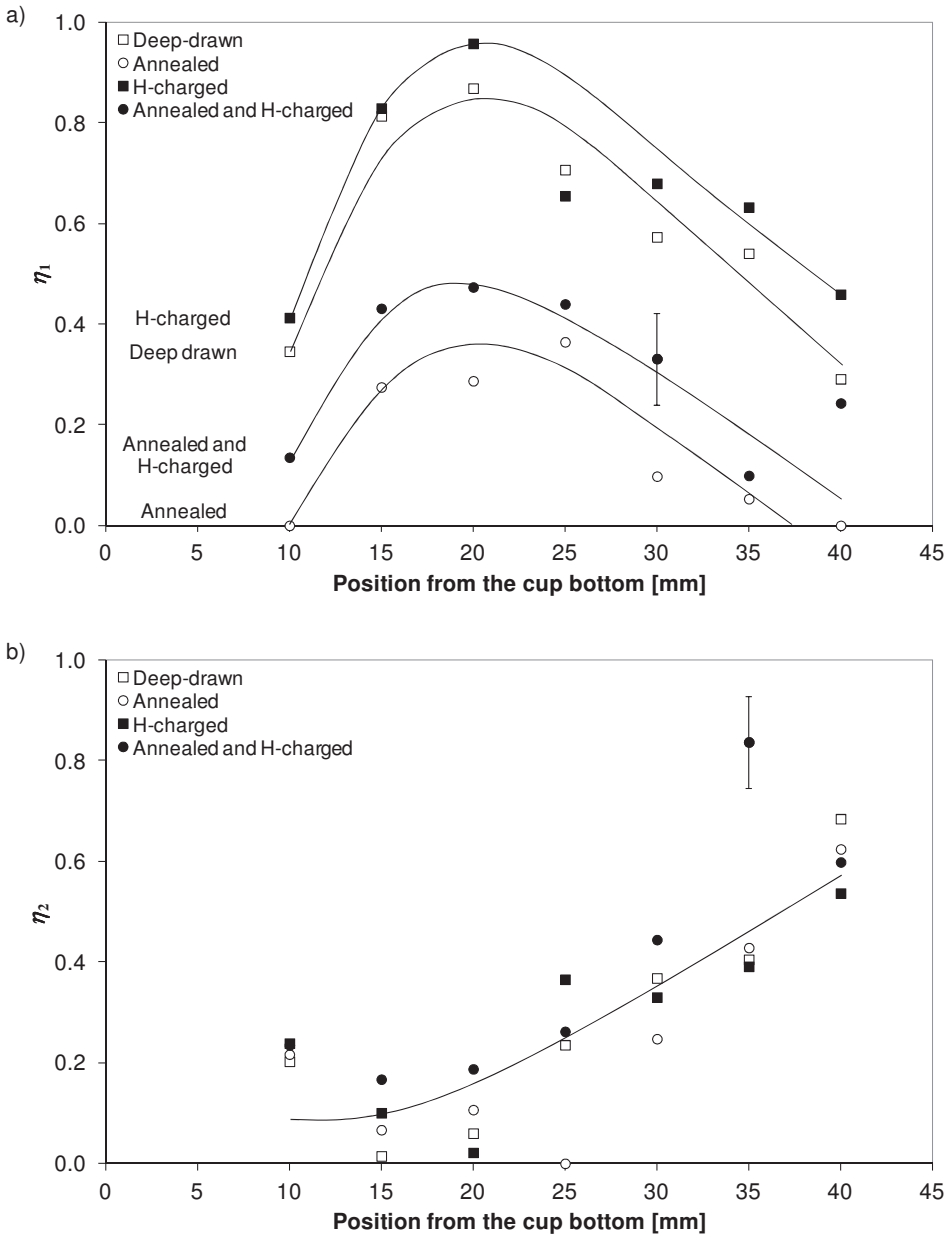

Figure 3.4 a) The fraction (η_1) of positrons trapped at defect type D_1 as a function of the position from the cup bottom. b) The fraction (η_2) of positrons trapped at defect type D_2 as a function of the position from the cup bottom.

On the basis of the observed XRD-line broadening alone (Figure 3.1), it is not possible to distinguish between different defect types. Hence, in Figure 3.5 the total fraction of positrons trapped at the defects $\eta_1 + \eta_2$ is plotted against the integral breadth. From this Figure it is concluded that for the deep-drawn cup the integral breadth varies linearly with the total positron trapping fraction $\eta_1 + \eta_2$.

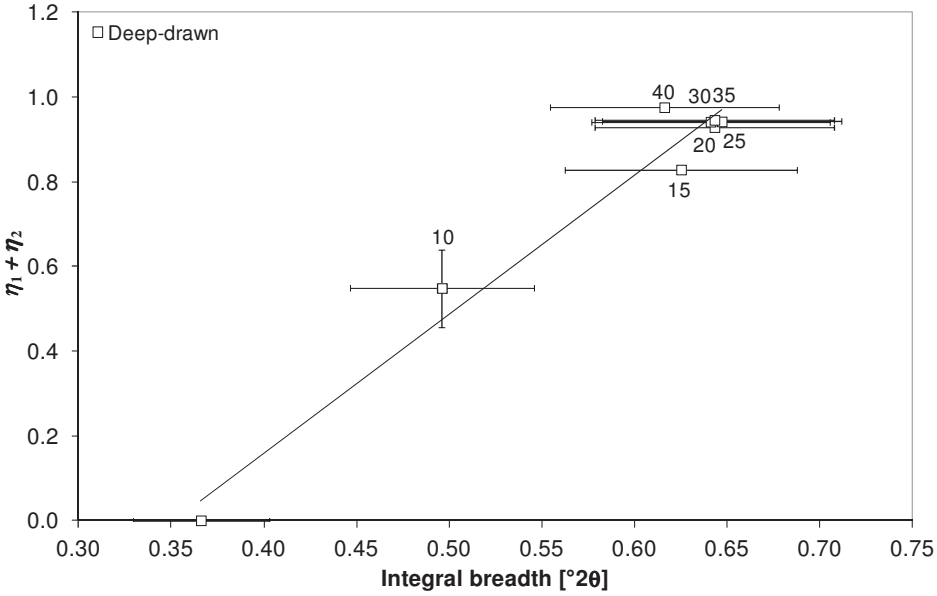

Figure 3.5 The total defect fraction $\eta_1 + \eta_2$ as a function of the integral breadth of the $\{111\}_\gamma$ reflection for the deep-drawn cup. The position from the cup bottom (in mm) is indicated.

3.2.4 Ferromagnetic phase

Magnetic measurements were performed to verify changes in the fraction of ferromagnetic phases, which can reveal the formation of α'-martensite. Figure 3.6 plots the magnitude of the local magnetic flux density caused by local magnetization as a function of η_2 for the deep-drawn cup (at 40 mm the magnetization could not be determined because this position is too close to the cup edge). Clearly, the magnetic flux density increases approximately linearly with increase in η_2. No such relationship could be found when the data was plotted as function of η_1 or $\eta_1 + \eta_2$.

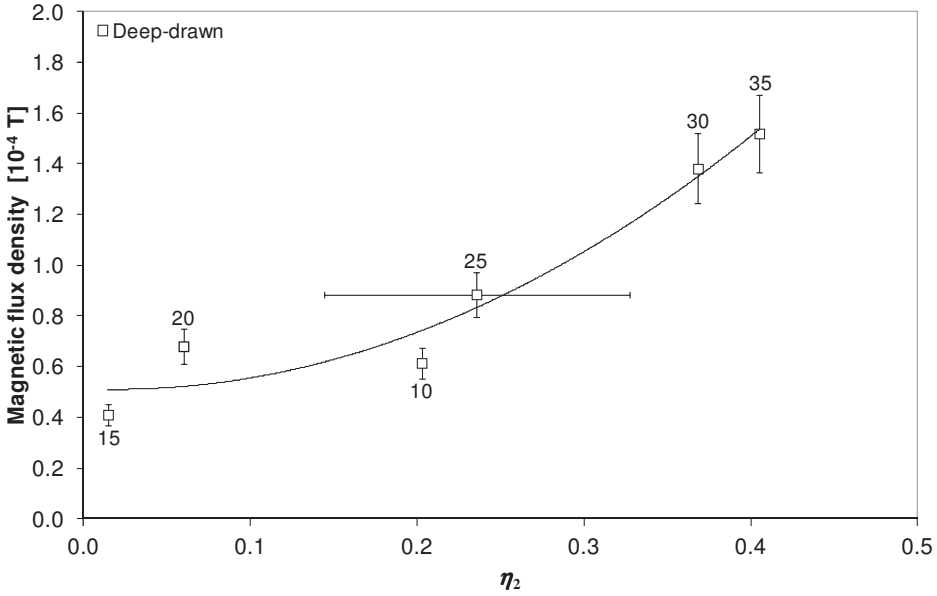

Figure 3.6 Magnetic flux density as a function of positron trapping fraction η_2 for the deep-drawn cup. The position from the cup bottom (in mm) is indicated.

3.3 Discussion of defect characteristics

Three indirect measurement techniques were used to investigate the generation of structural defects in austenitic Mn-based TWIP steels due to deep drawing. With increasing strain, XRD measurements indicate an initial increase in defect concentration, followed by a small decrease starting at 20 mm from the cup bottom. The positron annihilation results reveal that at least two types of positron trapping defects emerge with concentrations depending on the local strain conditions in the cup wall. Finally, magnetization measurements revealed an increase in the fraction of ferromagnetic phases, most likely the α'-martensite content.

3.3.1 Perfect dislocations

The development of the positron annihilation characteristics show that at low strain values the deformation in austenitic Mn-based TWIP steel is facilitated by dislocation slip. The W-S map and the derived trapping fractions, together with the results in literature [65, 66], suggests that η_1 can be related to perfect dislocations. This assumption is further corroborated by the fact that η_1 is sensitive to annealing and H-charging. Indeed annealing shows a similar effect on dislocations as stress relief. The introduction of hydrogen decreases the repulsive force and interaction energy between dislocations, resulting in

increasing dislocation mobility [61, 67]. In combination with the residual stress this may increase the dislocation density, reflected by the increase in the trapping fraction η_1 observed in Figure 3.4a).

3.3.2 Partial dislocations

At higher strain, deviating defect characteristics are observed. Since the S-parameter for defect type D_2 is structurally lower, but otherwise comparable to that of defect type D_1 the related defect can be expected to be also dislocation-like. A partial dislocation is a likely candidate to account for this observation. Partial dislocations play a role in twinning and plasticity-induced transformation and can therefore be expected to be generated in this material. The dissociation of a perfect dislocation into two Shockley partial dislocations (and consequently a stacking fault) is known to evolve differently for tension and compression deformation. According to Christian [68], on average this dissociation is more favourable under compression than under tension. The FEM simulations indicate that above 25 mm from the cup bottom the material is in compression. Partial dislocations have a smaller Burgers vector than perfect dislocations and consequently lead to a smaller normalized S-value. This and the fact that above 25 mm the material is in compression further confirms the suggestion that η_2 is related to partial dislocations. These partial dislocations play a role in twinning and plasticity-induced transformation and can be accompanied by stacking faults, twins, ε- and α'-martensite [27, 69]. Because of their thermal stability [27, 68] and the fact that η_2 is hardly sensitive to annealing (see Figure 3.4b)) we have another reason to relate η_2 to partial dislocations. In addition, the limited sensitivity of η_2 to hydrogen may be due to the smaller defect size, which results in the defect being a less attractive trapping site.

The observed relationship of the XRD-line broadening with the positron annihilation results corroborates the interpretation of the observed effects in terms of dislocations. On the other hand, the magnetization measurements show that α'-martensite formation takes place in the upper half of the cup. The fraction of martensite formed increases with the trapping fraction η_2 (Figure 3.6). It is therefore likely that α'-martensite forms through plasticity-induced transformation. The presence of α'-martensite can be accompanied by ε-martensite and twins [27]. The present findings attribute the defect type related to η_1 to perfect dislocations, whereas the defect type related to η_2 is attributed to partial dislocations and defects related to twinning or plasticity-induced transformation, which is shown to lead to the formation of α'-martensite. It is interesting to emphasize that the trapping fraction η_2 is found to show increasing values above a cup height of 20–25 mm (see Figure 3.4b)). It is at this cup height that the deformation state undergoes a transition from tensile to compressive. The formation of α'-martensite, as observed in magnetization measurements (Figure 3.6), can

therefore be concluded to correlate to the mode of deformation, being stronger in compression.

3.4 Conclusions

The presented investigation on the effect of deep drawing on defect generation in austenitic Mn-based TWIP steels leads to the following conclusions:

1. Positron annihilation detects that two different defect types result from plastic deformation during deep drawing. The two defect types can be expected to be perfect dislocations and partial dislocations.
2. Magnetic field measurements reveal the formation of α'-martensite which correlates with the density of the defects identified as partial dislocations. Martensite formation only takes place in those regions of the deep-drawn cup that are subjected to compressive deformation.

4 Effect of strain on the formation of α'-martensite

The effect of strain on the deformation mechanisms in deep-drawn and tensile-strained austenitic manganese-based TWinning Induced Plasticity steel is investigated using *ex-situ* magnetic measurements, X-ray diffraction, positron beam Doppler Spectroscopy, Transmission Electron Microscopy (TEM) and Finite Element Method simulations. The experimental observations reveal the formation of small fractions of α'-martensite at specific degrees of deformation, despite the high Stacking Fault Energy of the material (52 mJ/m^2). To understand the formation of α'-martensite in high Stacking Fault Energy TWinning Induced Plasticity steel deformed in the deep drawing mode, the existing phases were investigated using TEM. TEM revealed the formation of α'-martensite at shear band and twin intersections. The observed fraction α'-martensite is consistent with the estimated fraction of intersected shear bands acting as preferred nucleation sites for α'-martensite formation as a function of accumulated equivalent strain.

4.1 Introduction

In this chapter the effect of both deep drawing and tensile straining on the defect and microstructure evolution in austenitic manganese (Mn)-based TWinning Induced Plasticity (TWIP) steels was experimentally investigated using *ex-situ* magnetic measurements, X-ray diffraction (XRD) and positron beam Doppler Spectroscopy. The direct formation of α'-martensite from austenite in a deep-drawn austenitic Mn-based TWIP steel with high Stacking Fault Energy (SFE) is investigated using Transmission Electron Microscopy (TEM) techniques. The strain evolution during deep drawing was simulated by means of Finite Element Method simulations.

The superior mechanical properties of austenitic Mn-based TWIP steels are a result of deformation mechanisms involving twinning or plasticity-induced transformation [3, 45-48, 70] related to the austenite (γ) stability. The deformation mechanisms in these Mn-based TWIP steels have been most intensively investigated for tensile straining [45-48], leaving the role of large strain on the twinning or transformation-induced plastic deformation mechanism less exposed [71].

Austenite with a relatively low stability can transform to α'-martensite by means of the γ (Face Centred Cubic, FCC) → ε (Hexagonal Close Packed, HCP) → α' (Body Centred Cubic, BCC) sequence of martensitic transformations. Suppression of the strain-induced γ → ε-martensite transformation is therefore considered to imply stability against α'-martensite formation [8]. It has been argued on the basis of thermodynamic considerations [27, 51, 72] that Mn-based TWIP steel with a SFE higher than approximately 18 mJ/m^2 will not undergo strain-induced ε-martensite formation. Olson [28, 35] and other authors [57, 73-76] suggested the possibility of a direct α'-martensite formation from austenite without the intermediate transformation to ε-martensite. The material examined in the present contribution did not show any evidence of α'-martensite formation when tested in a conventional uni-axial test [57]. Direct experimental evidence for the γ → α'-martensite transformation has never been reported for Mn-based TWIP steel [77].

4.2 Microstructural evolution upon plastic deformation

It is important to note that positron beam Doppler spectroscopy and XRD only probe the outer side of the cup (penetration depths 1 μm and 10 μm, respectively) at a specific position from the cup bottom, whereas the magnetization measurements concern the full thickness of the cup. For that reason, magnetization results are related to the average accumulated equivalent strain ε_{eq}^{ac} over the cup thickness, whereas the XRD and positron annihilation results are related to ε_{eq}^{ac} at the outer side of the cup.

4.2.1 Formation of α'-martensite

Figure 4.1 shows the α'-martensite fraction as a function of ε_{eq}^{ac} averaged over the sample thickness measured by Vibrating Sample Magnetometry. There is an initial α'-martensite fraction of approximately 0.2%. Tensile straining does not affect the α'-martensite fraction. Deep drawing promotes the formation of α'-martensite. Straining at $\varepsilon_{eq}^{ac} \geq 0.6$ results in the formation of strain-induced α'-martensite. At 35 mm from the cup bottom in the TD, a sample was taken and cut into two pieces by spark erosion: one sample was taken from the inner side of the cup, another sample was taken from the outer side of the cup. For the sample at the inner side of the cup the accumulated equivalent strain was approximately 0.85. The maximum volume fraction of 1.2% α'-martensite was measured at this position, an amount too small to be detected by XRD.

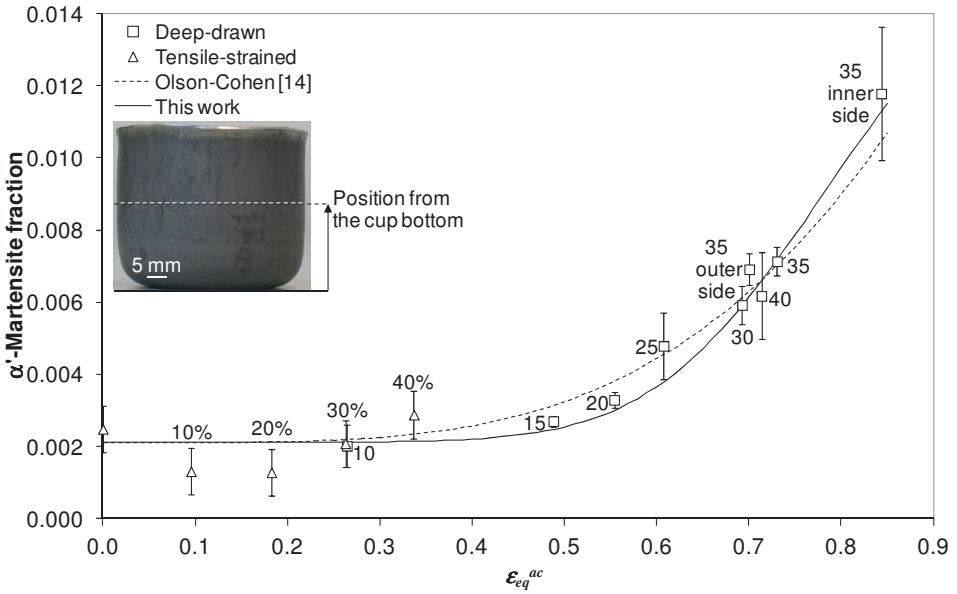

Figure 4.1 α'-Martensite fraction, determined by *ex-situ* magnetic measurements, for deep drawing and tensile straining as a function of ε_{eq}^{ac} averaged over the cup thickness. The tensile strain (in %) and the position from the deep-drawn cup bottom (in mm) are also indicated. At 35 mm from the cup bottom in the TD, a sample was taken and cut into two pieces by spark erosion: one sample was taken from the inner side of the cup, another sample was taken from the outer side of the cup. The labels 'inner side' and 'outer side' refer to these two samples.

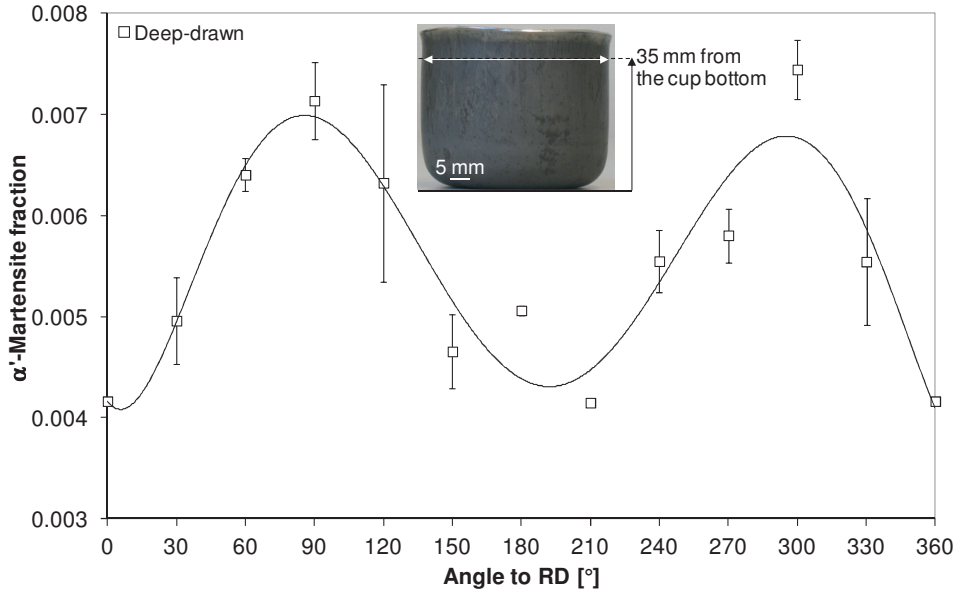

Figure 4.2 α'-Martensite fraction in a deep-drawn cup at a distance of 35 mm from the cup bottom as a function of the angle to the RD.

Figure 4.2 shows the α'-martensite fraction as a function of the angle to the rolling direction (RD). The measurements were made on the deep-drawn cup at 35 mm from the cup bottom where the accumulated equivalent strain was about 0.73. The results indicate a systematic trend as a function of the angle to the RD. The maximum α'-martensite fraction in the material can be found located in the transverse direction (TD) from the original centre of the blank, which most probably is related to the development of texture.

4.2.2 Dislocation multiplication and twinning

Figure 4.3 presents the integral breadth of the $\{111\}_\gamma$ XRD reflection, the most accurately determined reflection, as a function of ε_{eq}^{ac} at the outer side of the cup. The increase of tensile strain clearly increases the integral breadth. Increased straining during deep drawing initially increases the integral breadth in a similar way, followed by saturation for $\varepsilon_{eq}^{ac} \geq 0.6$. This increase in integral breadth prior to the formation of α'-martensite (see Figure 4.1) indicates dislocation multiplication and/or twinning. Straining at $\varepsilon_{eq}^{ac} \geq 0.5$ induces the formation of α'-martensite by allowing the passage of previously blocked dislocations [28, 35]. At $\varepsilon_{eq}^{ac} \geq 0.6$ α'-martensite formation increases more significantly, which does not cause further increase of the integral breadth. Later in this chapter positron beam Doppler data will enable to distinguish the different deformation mechanisms already indicated in Figure 4.3.

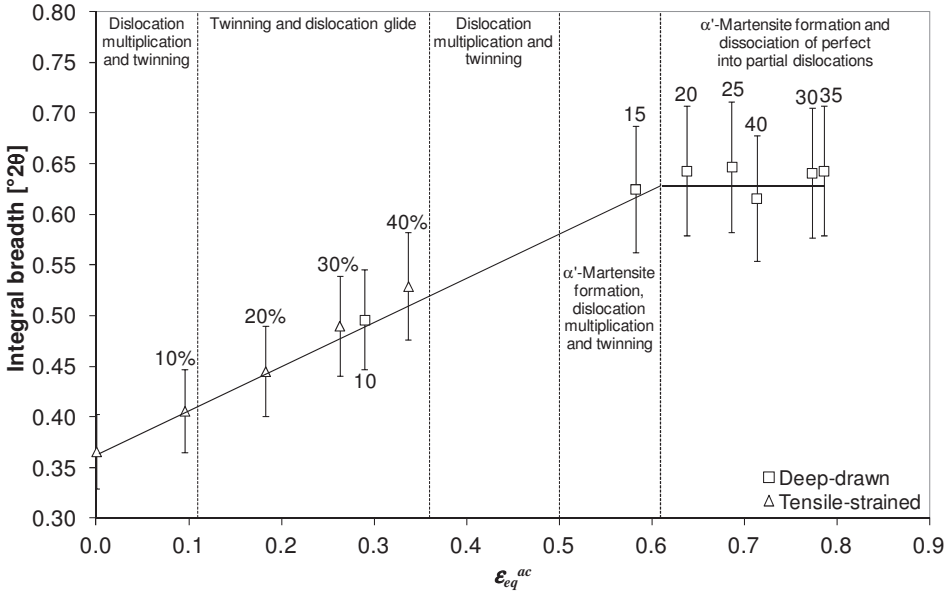

Figure 4.3 Integral breadth of the $\{111\}_\gamma$ reflection in XRD for deep drawing and tensile straining as a function of ε_{eq}^{ac} at the outer side of the cup. The tensile strain (in %) and the position from the deep-drawn cup bottom (in mm) are also indicated. Deformation mechanisms are schematically indicated.

4.2.3 Dislocation glide and dissociation into partial dislocations

Figure 4.4 shows the W-S map for deep drawing and tensile straining in which the S- and W-parameters are normalized with respect to the annealed material, S_b and W_b. Chapter 3 on positron beam Doppler spectroscopy on the present steel revealed the existence of two defect types D_1 and D_2 [76]. With characteristic S-W values (S_{D1}/S_b = 1.052, W_{D1}/W_b = 0.870) for defect D_1 and (S_{D2}/S_b = 1.037, W_{D2}/W_b = 0.860) for defect D_2 the fractions of positrons trapped at these defects η_1 and η_2 have been calculated, assuming two defect trapping states and using Equation (2.5). Equation (2.5) can be defined in an analogous manner for the W-parameter. In chapter 3 the larger defect type D_1 was attributed to perfect dislocations, whereas the smaller defect type D_2 was attributed to partial dislocations [76].

The positron annihilation results enable a further distinction of deformation mechanisms prior to and during α'-martensite formation. Figure 4.5 shows η_1 and η_2 as a function of ε_{eq}^{ac} at the outer side of the cup. At $\varepsilon_{eq}^{ac} \approx$ 0.1-0.4, positron annihilation reveals no change in trapping fractions η_1 and η_2, excluding dislocation multiplication and indicating twinning and dislocation glide as the dominant deformation mechanisms [27]. These twins

and their intersections act as barriers for further dislocation glide and eventually immobilize dislocations. Further straining requires dislocation multiplication and results in high stress concentrations at shear bands and their intersections, as evidenced by an increasing trapping fraction η_1 at ε_{eq}^{ac} up to 0.6. Once these high stress concentrations enable the passage of previously blocked (immobilized) dislocations and induce α'-martensite formation (see Figure 4.1), there is no need for further dislocation multiplication (as observed in Figure 4.3). At this stage, the positron annihilation results disclose that the formation of α'-martensite leads to a decreasing η_1. The simultaneous increase in η_2 indicates the formation of energetically more favourable partial dislocations enabling further relaxation of the internal stresses caused by the α'-martensite formation due to the lower density of α'-martensite in comparison to the original microstructure. These partial dislocations could originate from the dissociation of perfect dislocations, since both the integral breadth and the total defect fraction $\eta_1 + \eta_2$ remain constant with increasing α'-martensite fraction.

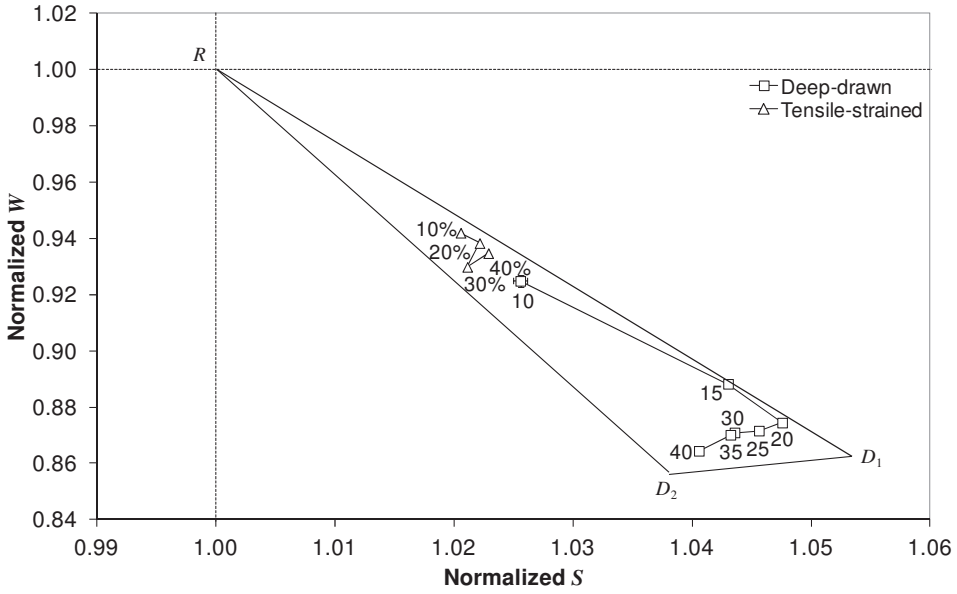

Figure 4.4 *W-S* map for austenitic Mn-based TWIP steel cups for deep drawing and tensile straining. R is the reference point, D_1 and D_2 are defect types [55]. The tensile strain (in %) and the position from the deep-drawn cup bottom (in mm) are also indicated.

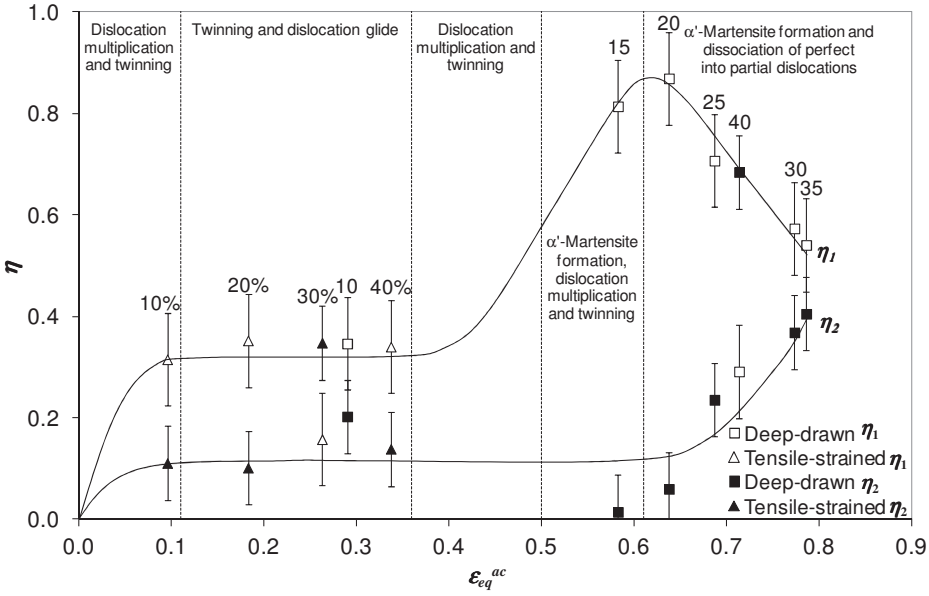

Figure 4.5 Fraction (η_1 and η_2) of positrons trapped at defect type D_1 (perfect dislocation [76]) and D_2 (partial dislocation [76]) resulting from positron beam Doppler spectroscopy as a function of ε_{eq}^{ac} at the outer side of the cup for deep drawing and tensile straining. The tensile strain (in %) and the position from the deep-drawn cup bottom (in mm) are also indicated.

4.2.4 Observation of α'-martensite

Figure 4.5 shows Bright Field (BF) images and related Selected Area Diffraction Patterns (SADP) from the TEM sample taken at 35 mm from the cup bottom on the inner side of a deep-drawn cup in TD. For the sampling the reader is referred to section 2.5.3 and Figure 2.9. The plasticity mechanisms were found to consist of a pronounced planar dislocation glide and the formation of planar features and bands related to the overlapping of multiple planar stacking faults, i.e. shear bands and narrow twins. The SADPs clearly indicate that not all narrow planar features in the highly deformed TWIP steel are twins. In fact many band-type features are found to be shear bands rather than twins. None of the diffraction patterns indicates the presence of ε-martensite. Considering the SFE of the alloy, the absence of ε-martensite and the presence of shear bands is expected.

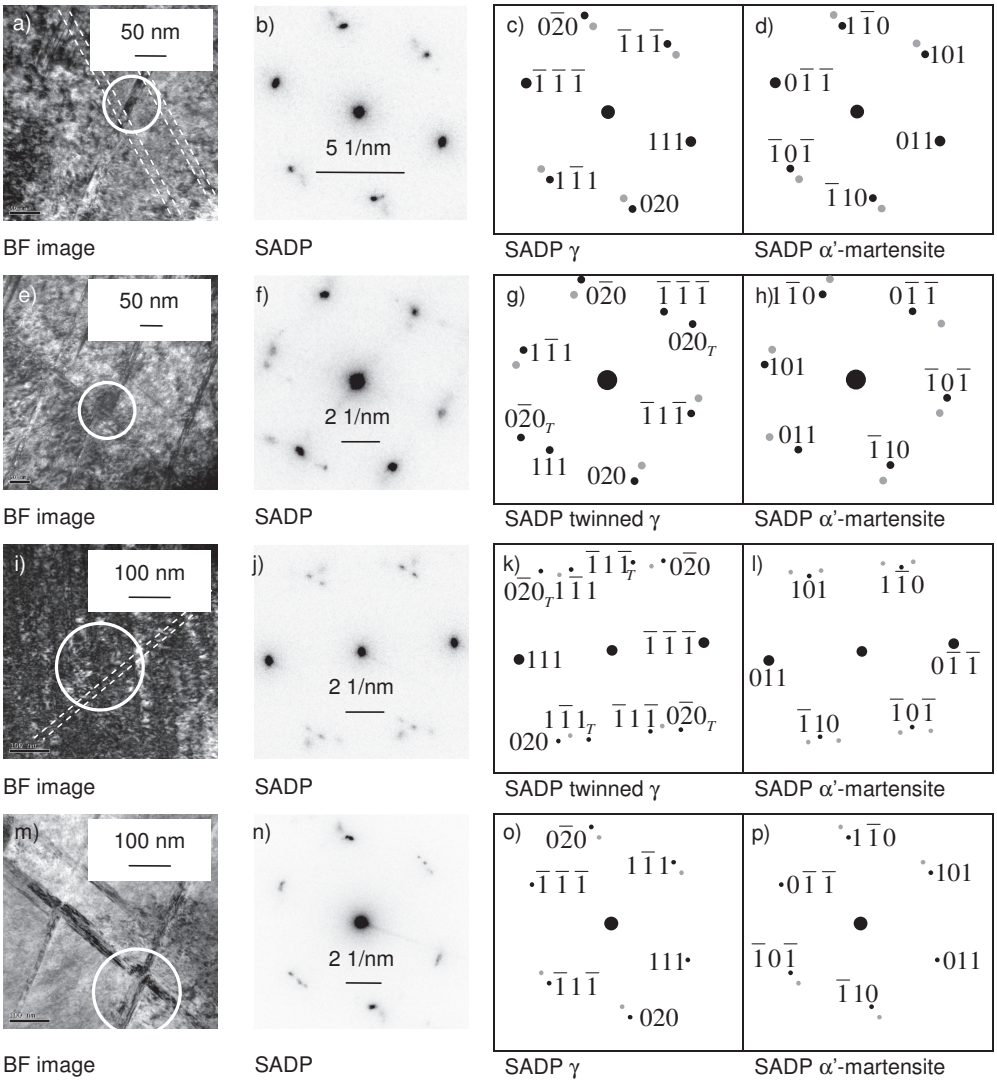

Figure 4.6 α'-Martensite at intersection of a)-d) shear bands, e)-h) twin and shear band, i)-l) twins, m)-p) shear bands. The TEM sample was taken 35 mm from the cup bottom on the inner side of the deep-drawn cup. The Figures a), d), i) and m) indicate the BF images, the Figures b), e), j) and n) indicate the SADPs, the Figures c), f), k) and o) indicate the SADPs, BF images. The white circles indicate the positions where the SADPs were taken. The dashed white lines in a) and i) indicate the position of shear bands with a low contrast. The black diffraction spots in the schematic SADPs in the third column are for the γ phase and include the relevant twin reflections. The black diffraction spots in the schematic SADPs in the fourth column are for the α'-martensite. The grey spots in the schematic SADPs indicate the diffraction spots of the other phase.

The orientation relationships between austenite and α'-martensite obey the Kurdjumov-Sachs orientation relationship between α'-martensite and austenite:

$$\{111\}_{\gamma} // \{110\}_{\alpha'}$$
$$\langle 110\rangle_{\gamma} // \langle 111\rangle_{\alpha'} \quad (4.1)$$

The micrograph in Figure 4.6a) shows a highly dislocated microstructure containing one clear band. The SADP reveals the band to be a shear band, rather than a twin, and shows the presence of α'-martensite. A secondary shear band system is also present, indicated by dashed white lines. The BF image (Figure 4.6e) and the corresponding SADP (Figure 4.6f) are for the two shear band systems and their intersection. The microstructure is severely deformed and contains a high dislocation density. The diffraction pattern reveals the presence of α'-martensite at the intersection between twins and shear bands. The high defect concentration at this type of intersections makes them very effective nucleation sites for strain-induced transformation [28, 35, 51]. Figures 4.6i)-n) show additional BF images and corresponding SADPs from the TEM sample. Due to the intense deformation, the deformation bands have a low diffraction contrast and the dashed white lines indicate the position of parallel shear bands, which are not clearly visible. The diffraction pattern however clearly reveals the presence of α'-martensite. The BF image in Figure 4.6m) shows two intersecting shear band systems, which are clearly visible despite the high dislocation density. The SADPs clearly reveal the presence of α'-martensite at shear band-shear band intersections.

4.3 Martensitic transformation

It has been reported that the deformation mechanisms responsible for the mechanical properties of austenitic Mn-based TWIP steels are related to the austenite (γ) stability and involve dislocation slip, twinning and plasticity-induced transformation to martensite [3, 45-48, 70]. With increasing ε_{eq}^{ac}, deformation is facilitated initially by dislocation multiplication, followed by twinning and/or martensitic transformations, providing barriers for further dislocation slip [3, 45-48, 70, 71].

4.3.1 Strain-induced nucleation of α'-martensite

Austenite with a relatively low stability can transform by means of $\gamma \rightarrow \varepsilon \rightarrow \alpha'$ martensitic transformations, resulting in a high work-hardening rate. Stability against the $\gamma \rightarrow \varepsilon$-

martensite transformation is usually considered to imply stability against the $\gamma \rightarrow \alpha$'-martensite transformation [8], since ε-martensite laths form as an intermediate phase. The present magnetic measurements indicate strain-induced α'-martensite formation by revealing a small volume fraction of α'-martensite when the accumulated equivalent strain is 0.5 or higher. TEM foil preparation does not induce such high accumulated equivalent strains and will therefore not be the origin for α'-martensite formation. The formation of α'-martensite is a three-dimensional phenomenon, being observed by TEM through thin sections. The widely held view is that α'-martensite must have ε-martensite as a precursor in Mn-based steels with Mn-contents above 10 wt% (see Figure 1.5) [8]. In Mn-based TWIP steels, α'-martensite is known to form at the intersections of shear bands like slip bands, twins and/or ε-martensite laths [28, 35]. The sequential nature of the $\gamma \rightarrow \varepsilon \rightarrow \alpha$' martensitic transformation at intersected ε-martensite laths and the increasing volume fraction of α'-martensite upon straining implies the simultaneous presence of ε- and α'-martensite. According to Olson and Cohen [28, 35], the sequential $\gamma \rightarrow \varepsilon \rightarrow \alpha$' martensitic transformation requires the intersection of at least one ε-martensite lath, which was not observed (Figure 4.6). ε-Martensite could only have been a precursor of α'-martensite formation in case of complete $\varepsilon \rightarrow \alpha$'-martensite transformation. Transformation from ε-martensite laths would have led to α'-martensite formation outside the intersected regions and higher α'-martensite fractions, which was not observed. The presence of ε-martensite as an intermediate phase at the intersected regions is untraceable after complete transformation to α'-martensite. We can conclude that the present observations question the $\gamma \rightarrow \varepsilon \rightarrow \alpha$' martensitic transformation as described by Olson and Cohen [28, 35]. The results strongly indicate that strain-induced nucleation of α'-martensite does not necessarily require the intermediate formation of ε-martensite laths.

In Mn-based TWIP steels with low SFE, α'-martensite is known to form at the intersections of bands like shear bands, twins and/or ε-martensite laths [28, 35] as seen in Figures 4.6e) and 4.6m). These intersected bands can be very effective as nucleation sites, allowing the passage of previously blocked dislocations, inducing the formation of α'-martensite [28, 35] and releasing stress concentrations [51]. Also in the Figures 4.6a) and 4.6i) secondary band systems have been observed, although less clearly as in the Figures 4.6e) and 4.6m).

4.3.2 Relation to the development of crystallographic texture during deep drawing

The results show that the formation of α'-martensite in the bulk material is related to both the accumulated equivalent strain and the crystallographic texture. One can assume the crystallographic texture components of the examined material to be a function of the angle to

the RD. The formation of α'-martensite in the material relates to the location of the material with respect to the RD. This observation is indicative of a relation between the formation of α'-martensite and the development of crystallographic texture during deep drawing. Similar Mn-based TWIP steels do not show planar anisotropy [78], suggesting subtle texture effects leading to anisotropy in strain-induced martensite formation. The TD has apparently a more favourable crystallographic texture for α'-martensite formation than the RD. Lo et al. [79] mentioned that twin-matrix lamellae, generated by heavy rolling deformation, are often oriented along the RD. Slip along the $\{111\}_\gamma$ planes in the RD and twinning is gradually suppressed as deformation proceeds, but slip along the $\{111\}_\gamma$ planes that are not parallel to the lamellae is activated. Deep-drawn material shows a high accumulated strain. It is also known that tensile deformation of medium SFE FCC metals or alloys favours the formation of twins in grains oriented with a <111> direction parallel to the tensile axis. It is therefore possible that straining in the TD can also activate the formation of strain induced martensitic transformation along the TD.

4.4 Evolution of α'-martensite volume fraction upon straining

The α'-martensite formation can be attributed to the magnitude of $\varepsilon_{eq}{}^{ac}$, providing the required density of shear band intersections and high stress concentrations. Liang et al. [47] also indicated the importance of the strain path for the microstructural evolution. Oh et al. [51] also observed the sequential formation of deformation twins and α'-martensite, which corresponds to the occurrence of intersections and consequent α'-formation at larger $\varepsilon_{eq}{}^{ac}$ (in the present study due to deep drawing). The strain occurring in tensile straining (also in case of 'deep drawing' at 10 mm from the cup bottom) is too small to induce α'-formation.

4.4.1 The Olson and Cohen model

As the intersections only account for a small fraction of the material, a relatively low α'-martensite fraction is formed, as observed in Figure 4.1. Based on their theory of embryo formation by strain, Olson and Cohen [35] proposed the following relation for the evolution of α'-martensite volume fraction upon straining

$$f_{\alpha'}{}^{OC} = 1 - \exp\left\{-\beta^{OC}\left[1 - \exp\left(-\alpha^{OC} \cdot \varepsilon_{eq}{}^{ac}\right)\right]^n\right\} + f_0 \qquad (4.2)$$

where α^{OC} and β^{OC} are two physically-significant, temperature-dependent parameters, $\varepsilon_{eq}{}^{ac}$ is the accumulated equivalent strain, n is a fixed exponent, with a suggested value n = 2 and f_0 is the initial α'-martensite fraction. We introduce f_0 in order to consider the initial α'-martensite

fraction. The orientation of the shear bands will not be random, but will tend to be initially parallel until secondary shear systems start to form. The formation of primary and secondary shear systems is not arbitrary and shows a sequential nature upon straining increasing the number of intersections exponentially. Olson and Cohen [35] claim that this behavior can be approximated by applying a higher exponent than n = 2 and found that β^{OC} = 1.18 and n = 4.5 gave the best overall result. Using their β^{OC} and n, Figure 4.1 shows that for α^{OC} = 0.48 the fit is in good agreement with the experimental results. Note that the fit includes an initial α'-martensite fraction of $f_0 = 2 \times 10^{-3}$.

4.4.2 The sequential behavior upon straining

We propose a similar approach for α'-martensite volume fraction evolution upon straining, in particular the sequential nature of the formation of primary and secondary shear systems upon straining. The proposed model describes the same physical process, but with slightly different approach, making the use of n > 2 as artificial approximation of the sequential behaviour of primary and secondary shear systems upon straining redundant. Figure 4.7 gives a schematic illustration for the formation of intersections of deformation shear-bands. The intersected area A_{int} is defined as

$$A_{\text{int}} = \frac{d^2}{\sin(\theta)} \tag{4.3}$$

with d the average width of a shear band (slip band, twin and/or ε-martensite lath) and θ the angle between the primary and secondary shear systems (see Figure 4.7).

The volume fraction of intersected shear bands $f_{\text{int}}{}^{sb}$ can be estimated by

$$f_{\text{int}}{}^{sb}(d,l) = \left(\frac{d}{d+l}\right)^2 \tag{4.4}$$

where l is the average distance between two shear bands of an shear system and g is the grain size, which is cancelled out in Equation (4.4). The volume fraction of intersected shear bands is related to the ratio between d and l and is independent of their absolute values. According to Elhami et al. [80], the deformation mode influences the number and size of twins. In literature [8], the mean twin width is assumed to be 0.03 μm, leaving the average distance between two shear bands of a shear system as remaining parameter. As Olson and Cohen [35] pointed out, the formation of primary and secondary shear systems is not arbitrary and shows a sequential nature upon straining. This sequential behavior requires the

introduction of Equation (4.5). Equation (4.4) can therefore be rewritten as α'-martensite volume fraction evolution upon straining

$$f_{\alpha'}^{\ sb} = f_0 + p\left(\frac{d}{d+l_1}\right)\cdot\left(\frac{d}{d+l_2}\right) \tag{4.5}$$

where l_1 is the average distance between two shear bands of the primary shear system, l_2 is the average distance between two shear bands of the secondary shear system and p is the probability for nucleation of α'-martensite at the shear band intersection. Taking into account the sigmoidal shape of α'-martensite formation upon straining, l_1 and l_2 can be defined as

$$l_1 = g\cdot\exp\left(-\alpha^{sb}\cdot\varepsilon_{eq}^{\ ac}\right) \tag{4.6}$$

and

$$l_2 = g\cdot\exp\left(-\alpha^{sb}\cdot\left(\varepsilon_{eq}^{\ ac}-\varepsilon_{\alpha'}\right)\right),\ \varepsilon_{eq}^{\ ac} > \varepsilon_{\alpha'} \tag{4.7}$$

where α^{sb} is a fitting parameter and ε_2 the strain at which α'-martensite formation starts. Fitting the experimental results of Figure 4.1 for d = 0.03 µm [8], g = 5 µm, α^{sb} = 9 and $\varepsilon_{\alpha'}$ = 0.2 leads to a probability p = 0.03.

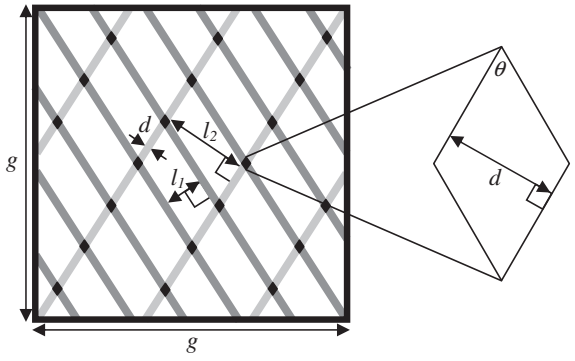

Figure 4.7 Schematic illustration for the formation of intersections of deformation shear-bands with (1) deformation shear-bands and (2) grain boundaries. The dark grey shear-bands indicate the primary shear-band system and the light grey shear-bands indicate the secondary shear-band system.

The comparison between the proposed model and the Olson-Cohen model does not proclaim a clear preference. However, the proposed model does not require the artificial approximation of the sequential behaviour upon straining, but describes this behaviour according to the geometrical model put forward by Olson and Cohen [28]. Fitting this model reveals a very low probability for nucleation of α'-martensite at shear band intersections, confirming the physical meaning of this approach.

The accumulated equivalent strain ε_{eq}^{ac} is suggested as a relevant measure of strain enabling the comparison between tensile straining and deep drawing. With increasing ε_{eq}^{ac}, deformation is facilitated by dislocation multiplication, dislocation glide and twinning, providing the required intersections of shear bands for eventual α'-martensite formation at high ε_{eq}^{ac}. It is therefore suggested that the appropriate deformation mechanisms, in particular the formation of α'-martensite, can be related to ε_{eq}^{ac}.

4.5 Conclusions

The presented investigation of the relation between the strain and the deformation mechanisms (in particular the formation of α'-martensite) in austenitic Mn-based TWIP steel in tensile and deep drawing deformation leads to the following conclusions:

1. Despite its high SFE (52 mJ/m^2), deep drawing deformation results in the formation of α'-martensite, which is attributed to the accumulated equivalent strain and crystallographic texture.
2. The presence of α'-martensite at shear band and twin intersections is observed and questions the sequential $\gamma \rightarrow \varepsilon \rightarrow \alpha'$ martensitic transformation. The results indicate that the formation of α'-martensite in a high SFE FCC alloy does not necessarily require the intermediate formation of ε-martensite laths.
3. A model for α'-martensite volume fraction evolution upon straining is proposed and the estimated fraction of intersected shear bands - the preferred nucleation sites for α'-martensite formation - as a function of accumulated equivalent strain is in good agreement with the experimentally determined α'-martensite fraction.

5 Role of α'-martensite in the phenomenon of delayed fracture

The phenomenon of delayed fracture in three austenitic manganese-based TWinning Induced Plasticity steels is investigated by means of video observation and *ex-situ* magnetic measurements. Delayed fracture is observed in the direction perpendicular to the rolling direction, in coincidence with the highest α'-martensite fraction in a deep-drawn cup. The formation of a small fraction of α'-martensite, irrespective of the chemical composition examined, is indicative for the formation of crack initiation sites. We propose an intermittent crack propagation concept and model for the phenomenon of delayed fracture.

5.1 Introduction

This chapter investigates the role of α'-martensite in the phenomenon of delayed fracture on austenitic manganese (Mn)-based TWinning Induced Plasticity (TWIP) steels after deep drawing, observed by *in-situ* video recording. *Ex-situ* magnetic measurements have been used to systematically measure the fraction of α'-martensite. The formation of α'-martensite indicates the formation of crack initiation sites, which is discussed as a possible cause of delayed fracture.

McCoy and Gerberich [81] showed that in case of TRansformation Induced Plasticity (TRIP) steel it is the α'-martensite which is susceptible to hydrogen embrittlement. The slow crack growth in TRansformation Induced Plasticity steel involves the diffusion of hydrogen through the α'-martensite. Cathodic charging injects the hydrogen at the surface of the material, embrittling the α'-martensite in the surface layer. The coalescence of cracks initiated at the embrittled α'-martensite into a macrocrack results in slow crack growth from the surface inward consisting of discontinuous jumps. According to McCoy and Gerberich [81], the presence of α'-martensite in combination with a sufficient H-concentration results in embrittlement.

The α'-martensite fraction strongly affects the delayed fracture susceptibility [6]. Chapter 4 [82] investigates the formation of α'-martensite after deep drawing a blank into a cup. It shows that the maximum α'-martensite fraction occurs in transverse direction (TD) close to the surface at the edge of the deep-drawn cup, enhancing the risk for embrittled α'-martensite. Deformation along the rolling direction (RD) leads to a higher fraction of grains orientated for deformation twinning than in the TD [8]. Material at the RD in the cup has a higher twinning rate and volume fraction of twins than material at the TD, due to the higher density of grains suitably orientated for deformation twinning [83]. This chapter investigates the phenomenon of delayed fracture of three austenitic Mn-based TWIP steel grades and measured the α'-martensite fraction.

5.2 Susceptibility to delayed fracture and the presence of α'-martensite

5.2.1 Visual observations of delayed fracture

To reveal the phenomenon of delayed fracture, Figure 5.1 shows some examples of side-view images from the video observation of delayed fracture in air of material B. After initiation at the cup edge after 37 hours, the crack advances along the vertical direction and finally proceeds to a length of approximately 19 mm after 60 hours. The top-view images reveal that there are two cracks and the observed crack in the side-view images is the second crack to

occur. The crack growth of the first one was not monitored by the equipment. Delayed fracture predominantly occurs close to the TD, i.e. perpendicular to the RD of the cold rolled sheet. In the course of the delayed fracture process, the shape of the cup edge changes from circular to oval. The two cracks are situated farthermost from one another, drawing up the larger axis of symmetry of the oval.

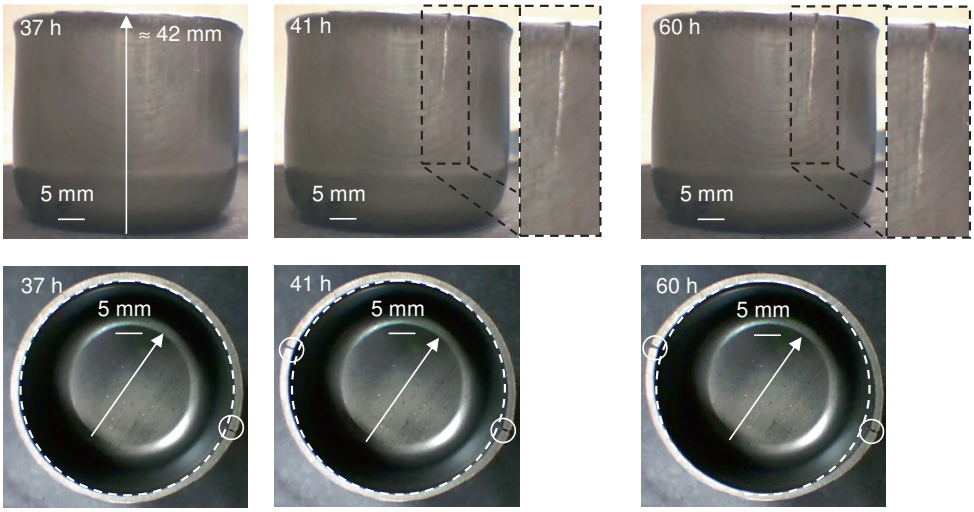

Figure 5.1 Side-(upper) and top-(lower) view images from the video observation of delayed fracture in air after 37, 41 and 60 hours of testing for material B. The labels on the lower left corner of the images denote the time after deep drawing. The white-dashed ellipsoids indicate the original cup diameter. The white arrows indicate the RD. The white full circles indicate the crack positions.

The observed crack growth is also shown in Figure 5.2, where the crack length is determined by image analysis. The fracture consists of three stages [5]: an incubation period, an active period and an inert period. After the incubation period, fracture is first observed at t_0 and proceeds intermittently to t_1 (active period) and eventually stagnates at a final crack length L^{f} (inert period). The final crack length observed for the crack in Figure 5.1 is 19 mm. The incubation period refers to the delay time in fracture. All delayed fracture monitoring results are elaborated in this manner to enable comparison. The macroscopic crack growth has an intermittent character resembling the crack growth behaviour in [81].

All delayed fracture results are summarized in Figure 5.3 and Table 5.1. Figure 5.3a) shows the crack length L as a function of time for grades A, B and C in air and in tap water. The crack length here is the average of three simultaneously assessed cups of identical conditions. The order of delayed fracture in terms of the final crack length L^{f} is B > A > C in

air and C > B > A in water. The order of delayed fracture in terms of delay time t_0 and active-period length t_1 - t_0 is B > A > C in air and water. The difference between the grades is more distinct in air than in water. For all three grades, submersion in tap water results in a shorter average incubation period, a shorter average active period and a larger average crack length. Grade C does not show fracture in the entire period of 1680 hours of testing in air, but shows the largest crack length when submersed in tap water.

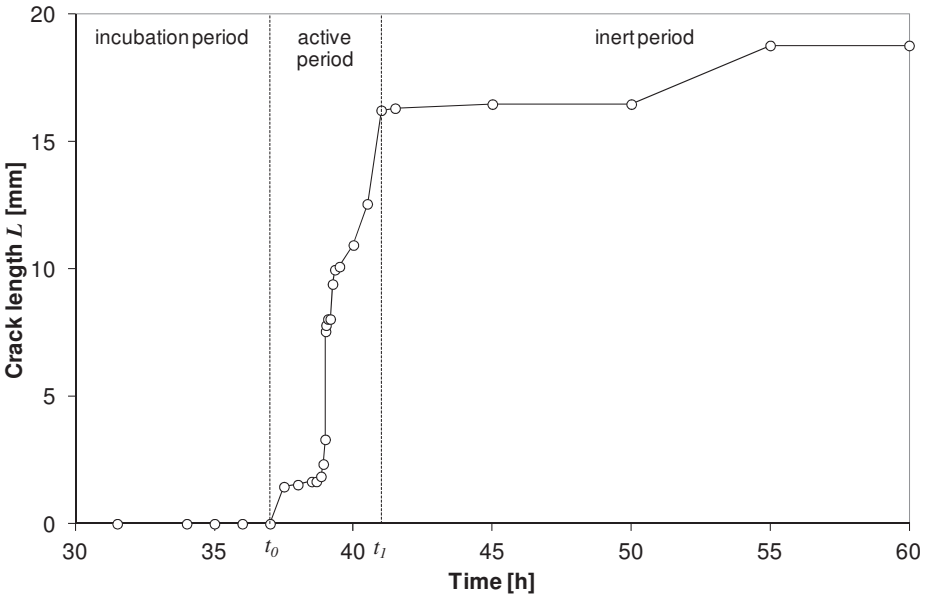

Figure 5.2 Crack length as a function of time of material B in air.

Figure 5.3b) shows the number of cracks n as a function of time for grades A, B and C in air and in tap water. The number of cracks is the average of three simultaneously assessed cups of identical conditions. Grade C in air does not show delayed fracture. The order of delayed fracture in terms of the final number of cracks n^f is B > A > C in air and in water. For all three grades, submersion in tap water results in a higher average number of cracks. The number of cracks saturates after a certain time for all grades and conditions, except n_B^f in water which continues to increase with time.

Table 5.1 summarizes the delayed fracture results of Figure 5.3. The time t_0 indicates the average time until first observation of fracture (incubation period, start of active period) and the time t_1 indicates the average time until stagnation of the crack (end of active period, start of inert period). The given t_0- and t_1-values are based on the average of three simultaneously assessed cups of identical conditions. The order of delayed fracture

susceptibility in terms of crack length L, delay time t_0 and active-period duration t_1 - t_0 is B > A > C, except for the order in terms of the crack length in water.

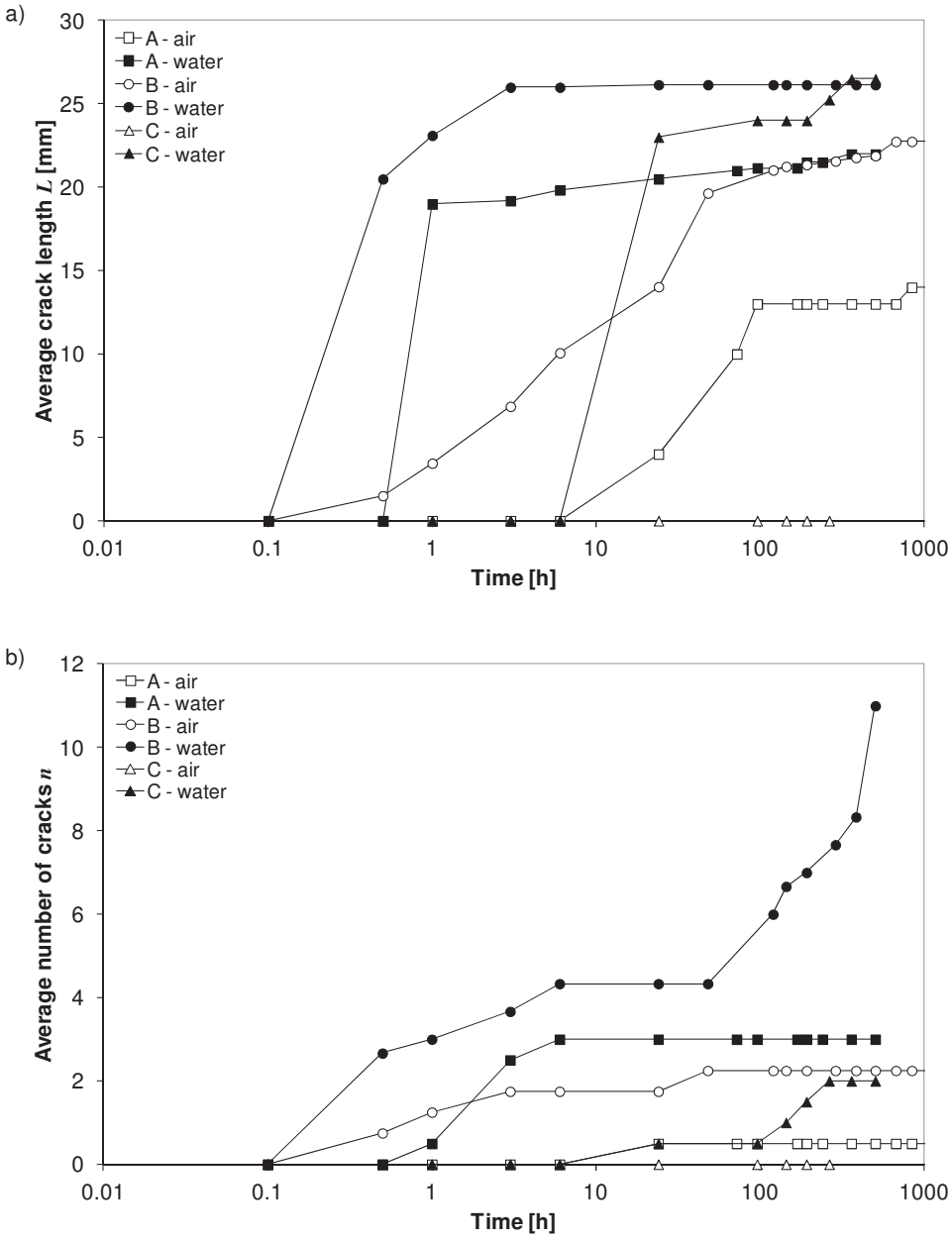

Figure 5.3 a) Average crack length as a function of time for grade A, B and C in air and water. b) Number of cracks as a function of time for grade A, B and C in air and water.

Table 5.1 Summary of delayed fracture results.

Grade	Air					Water				
	t_0	t_1	t_1 - t_0	L^f	n^f	t_0	t_1	t_1 - t_0	L^f	n^f
	[h]	[h]	[h]	[m]		[h]	[h]	[h]	[mm]	
A	6.0	96.0	90.0	14	0.5	0.5	1.0	0.5	22	3.0
B	0.1	24.0	23.9	23	2.3	0.1	0.5	0.4	26	11.0
C	>1680	-	-	0	0.0	6.0	24.0	18.0	27	2.0

5.2.2 Stacking Fault Energy and the formation of α'-martensite

The magnetic saturation, from which the small α'-martensite fraction is determined [53], was measured along the cup wall at the TD for all grades and also at the RD for Grade A.

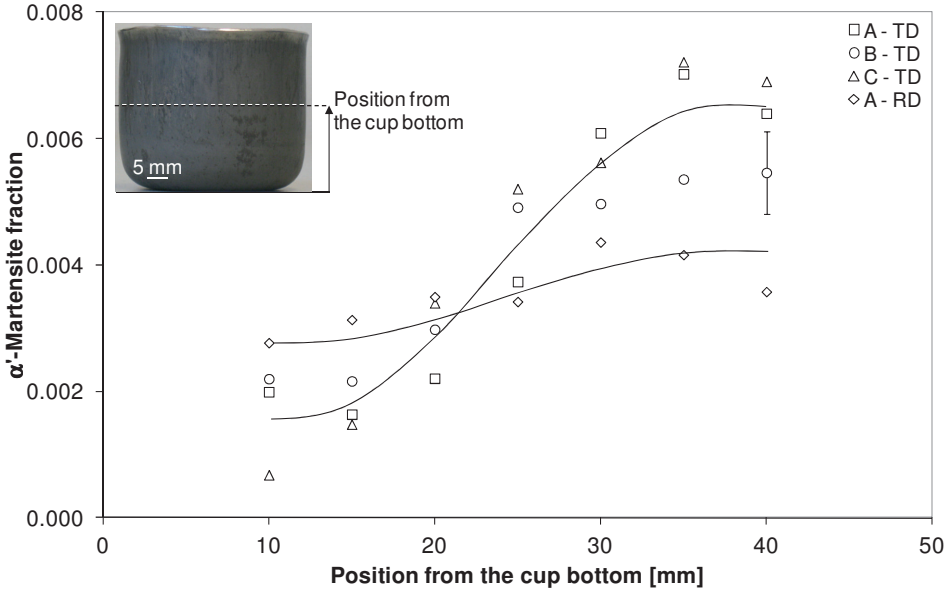

Figure 5.4 α'-Martensite fraction after deep drawing as a function of the position from the cup bottom for grade A, B and C at the TD and for grade A at the RD. The full and dashed lines are to guide the eye.

Figure 5.4 shows that after deep drawing a very small α'-martensite fraction ($f_{\alpha'}$ < 0.007) is present as a function of the position from the cup bottom for all three grades and it is worthy to note that the fraction in all cases is less than 0.7%. The α'-martensite fraction starts to increase at 15 mm from the cup bottom as a result from deep drawing. No significant differences in the α'-martensite fraction are found for the different grades, despite their

difference in Stacking Fault Energy (SFE). Figure 5.4 shows that the α'-martensite fraction at a higher position from the cup bottom is higher at the TD than at the RD.

5.3 Proposed mechanism for delayed fracture

This chapter investigated the phenomenon of delayed fracture of three austenitic Mn-based TWIP steel grades and measured the α'-martensite fraction. For all three grades, submersion in tap water results in a shorter average incubation period, a shorter average active period, a larger average crack length and a higher average number of cracks. A small fraction of α'-martensite is detected (less than 0.7%), which increases with the position from the cup bottom and is higher in material at the TD than at the RD. Delayed fracture is observed in the direction perpendicular to the RD, in coincidence with the highest α'-martensite fraction in a deep-drawn cup.

5.3.1 Role of α'-martensite

One of the influencing factors for the phenomenon of delayed fracture in TWIP steels is reported to be the austenite stability [6], often indicated by the SFE. It is well known that the SFE predominantly determines the deformation mechanisms, but its role with respect to austenite stability per se has to be put in perspective [2-4]. Rather than the SFE as such, the formation of α'-martensite indicates the (meta-)stability of the austenite [82]. α'-Martensite is shown to form at the intersections of slip bands, twins and/or ε-martensite laths [4, 28], due to the high stress concentrations occurring at these intersections [51, 82, 84]. Chapter 4 [82], using TEM techniques, confirmed the presence of α'-martensite after deep drawing in the high SFE steel grade A. The magnetic experiments indeed reveal no significant difference in α'-martensite fraction between the examined compositions, indicating that the formation of α'-martensite is rather a geometrical mechanism of intersecting shear bands than governed by the SFE in the range covered by the steels in this study. This is in agreement with Chapter 4 [82, 84], stating that the formation of α'-martensite does not require the formation of intermediate ε-martensite laths [82] and is a function of the estimated fraction of intersected shear bands [84].

Intersected shear bands can be very effective as nucleation sites, allowing the passage of previously blocked dislocations, inducing the formation of α'-martensite and releasing stress concentrations [51], indicating the link between the presence of α'-martensite and the residual stress. Berrahmoune [6] showed that the highest tangential stresses were approximately halfway the cup height. These results apply to the deep drawing of a cup in general, irrespective of the occurrence of delayed fracture. For that reason the residual stress is not of more importance than the presence of α'-martensite.

Koyama [11] observed the formation of crack initiation sites at twin boundaries resulting from high stress concentrations at intersections of grain and twin boundaries with deformation twins in TWIP steel. Intersections of twin boundaries with deformation twins are potential nucleation sites for α'-martensite [28]. The α'-martensite fraction is an indication for the formation of crack initiation sites.

5.3.2 Intermittent crack propagation concept

To reveal the delayed fracture mechanism observed, Figure 5.5 gives a schematic view of the intermittent crack propagation concept. Crack initiation sites form at potential nucleation sites for α'-martensite [11] and coalesce into a macrocrack. A higher α'-martensite fraction relates to a higher density of potential crack initiation sites and easier coalescence. Cracking is most likely to occur first at locations with a relatively high α'-martensite fraction, advancing until the density of crack initiation sites is too low for further crack propagation. Crack arrest is likely to occur at shear band intersections.

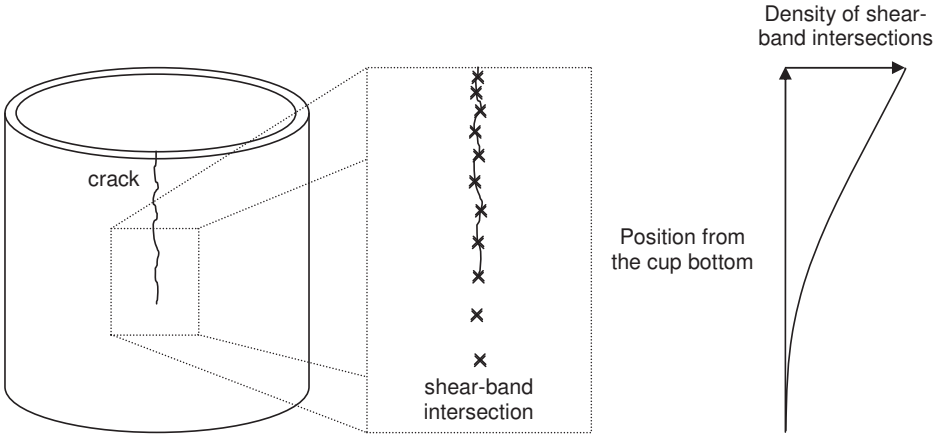

Figure 5.5 Schematic illustration of the proposed intermittent crack propagation concept. Crack propagation occurs through the coalescence of microcracks from shear-band intersection to shear-band intersection. The density of shear-band intersections increases with the position from the cup bottom.

5.3.3 Evolution of crack initiation sites upon straining

Based on the geometrical model introduced in Chapter 4 [84], we adapt the model for crack initiation site evolution upon straining through the accumulated interface length per unit grain area of intersections of deformation shear-bands with (1) deformation shear-bands and (2)

grain boundaries. A schematic illustration for the formation of intersections of deformation shear bands deformation with shear bands and grain boundaries is shown in Figure 4.6.

The density of crack initiation sites as a function of strain is related to the accumulated interface density I_{total}^{ac}, which can be written as

$$I_{total}^{ac} = \frac{4d}{g\sin(\theta)}\left(\frac{g}{(d+l_1)(d+l_2)} + \frac{1}{d+l_1} + \frac{1}{d+l_2}\right) \tag{5.1}$$

with d the average width of shear bands, g the grain size, θ the angle between the primary and secondary shear-band systems, l_1 the average distance between shear bands of the primary shear-band system (see Equation (4.6)) and l_2 the average distance between shear bands of the secondary shear-band system (see Equation (4.7)). The first term between the parentheses of Equation (5.1) accounts for the accumulated interface density of shear-band intersections $I_{sb\text{-}sb}^{ac}$. The second and third term between the parentheses of Equation (5.1) consider the accumulated interface density of intersections of grain boundaries with deformation shear bands $I_{gb\text{-}sb}^{ac}$.

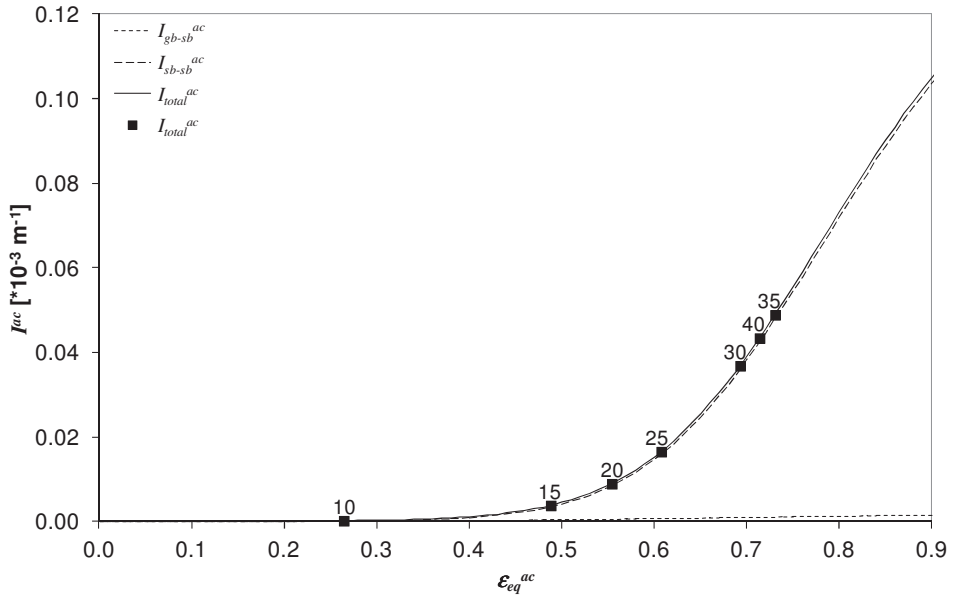

Figure 5.6 Accumulated interface density of intersections of grain boundaries with deformation shear bands ($I_{gb\text{-}sb}^{ac}$), of shear band intersections ($I_{sb\text{-}sb}^{ac}$) and total (I_{total}^{ac}) as a function of strain. The position from the deep-drawn cup bottom (in mm) are indicated.

Figure 5.6 shows $I_{gb\text{-}sb}{}^{ac}$, $I_{sb\text{-}sb}{}^{ac}$ and $I_{total}{}^{ac}$ as a function of strain, using θ = 70°, d = 30 nm, g = 5 µm, α^{sb} = 9 and ε_2 = 0.2 obtained in [84]. Straining results in the formation of crack initiation sites, leading to a significant increase of $I_{total}{}^{ac}$ for $\varepsilon_{eq}{}^{ac} \geq 0.4$. The contribution of $I_{gb\text{-}sb}{}^{ac}$ to $I_{total}{}^{ac}$ is very limited, $I_{sb\text{-}sb}{}^{ac}$ is mainly responsible for the increase in $I_{total}{}^{ac}$, indicating that the density of intersections of the secondary shear-band systems with the primary shear-band system controls the evolution of crack initiation sites upon straining. Figure 5.6 indicates the position from the deep-drawn cup bottom, based on the Finite Element Method simulations of the cup deep drawing process performed in [84]. The highest $I_{total}{}^{ac}$ is achieved at 35 mm from the deep-drawn cup bottom.

Figure 5.7 shows $I_{total}{}^{ac}$ for austenite grain sizes g = 50, 10, 5 and 1 µm. Chapter 2 and 4 [84] indicated that the initial grain size is approximately 5 µm. The calculations show that a larger grain size can significantly reduce $I_{total}{}^{ac}$. Crack propagation occurs parallel to primary and secondary shear-band systems [11]. The length increase l' for cracks to propagate from one shear band to another can be written as

$$l' = \frac{l}{\sin(\theta)} \tag{5.2}$$

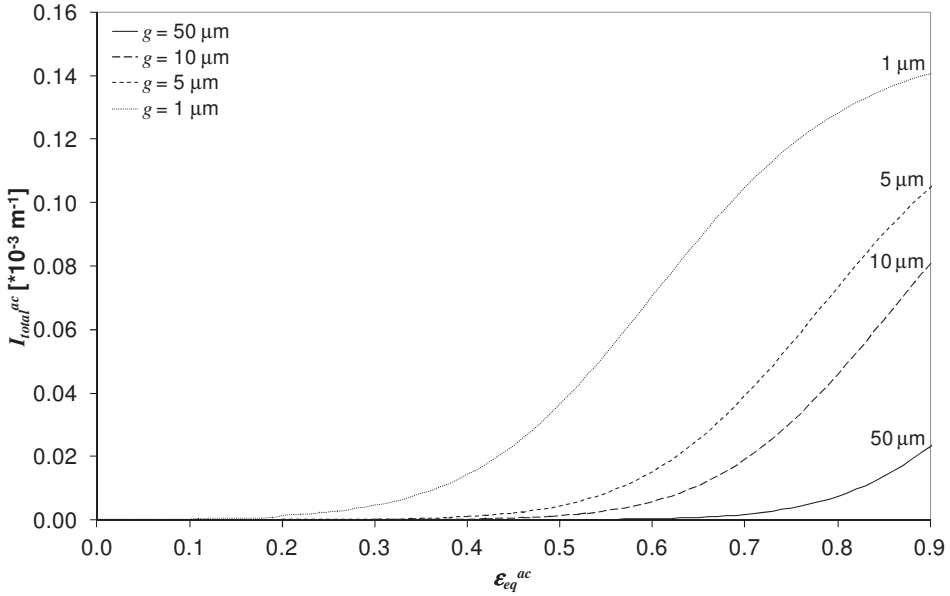

Figure 5.7 Total accumulated interface length per unit area for g = 50, 10, 5 and 1 µm, using θ = 70°, d = 30 nm, α^{sb} = 9 and ε_2 = 0.2 obtained in [84].

Figure 5.8 shows l' for the primary and secondary shear-band system as a function of strain. l' decreases upon straining, easing crack coalescence. The strain ε_2 at which the secondary shear-band system starts to form is key for the formation of shear-band intersections. Crack coalescence from crack initiation sites at intersections uses both shear-band systems, crossing different lengths, resulting in discontinuous jumps and explaining the observed intermittent crack growth behaviour.

The results of Figure 4.1b) and 5.4 show that α'-martensite formation in the material relates to the direction at which the material is with respect to the RD in the blank, indicating a relation of the shear-band intersections with respect to the RD. As reported, there is a higher density of grains suitably orientated for deformation twinning resulting in a higher twin production rate and twin volume fraction at the RD than at the TD [83]. In order to facilitate deformation in material at the TD, the secondary shear-band system will be activated at lower strain ε_2, resulting in more shear band intersections. Figures 5.6 and 5.8 show the importance of the secondary shear-band system for the formation of crack initiation sites with increasing strain and therefore for delayed fracture. Delayed fracture predominantly occurs close to the TD, where the highest α'-martensite fraction is detected, providing further proof for this concept.

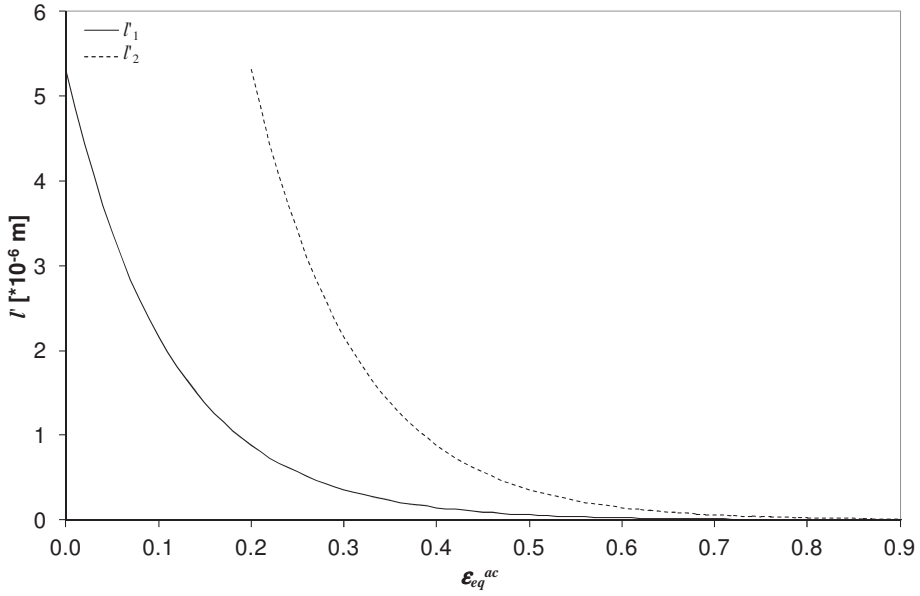

Figure 5.8 Crack propagation length for the primary and secondary shear-band system, using θ = 70°, d = 30 nm, α^{sb} = 9 and ε_2 = 0.2 obtained in [84].

The order in SFE (grade A > B > C) does not correspond to the order in delayed fracture susceptibility (grade B > A > C) and does not affect the formation of α'-martensite. The formation of α'-martensite indicates the presence of crack-initiation sites, which are formed during deep drawing. The coalescence of these microcracks might be responsible for the delay time. A higher density of crack-initiation sites eases crack coalescence and could influence the delay time. The α'-martensite fraction of the three steel grades covered in this study are equal and represent an equal density of crack-initiation sites. This cannot explain the difference in delayed fracture susceptibility between these three steel grades. The difference is attributed to two other factors influencing crack coalescence: (1) the residual stress and (2) the resistance against crack propagation.

5.4 Conclusions

The presented investigation of delayed fracture in three austenitic Mn-based TWIP steels after deep drawing leads to the following conclusions:

1. Delayed fracture occurs along the TD where the α'-martensite fraction is the highest. An intermittent crack propagation concept and model is proposed based on the coalescence of initial cracks into a macrocrack. A higher α'-martensite fraction indicates a higher density of shear-band intersections, resulting in more potential crack-initiation sites and easier coalescence.
2. The order of delayed fracture susceptibility in terms of crack length L, delay time t_0 and duration of the active period of crack growth t_1 - t_0 is B > A > C, except for the order in terms of crack length L in water. This indicates no direct relation with the SFE.
3. The SFE in the SFE range tested does not affect the formation of α'-martensite.

6 Effect of prior plastic deformation on the kinetics of austenite decomposition

In this chapter, pearlite formation in undeformed and deformed austenitic manganese-based TWinning Induced Plasticity steel is investigated by means of *in-* and *ex-situ* magnetisation measurements and optical and scanning electron microscopy. The metastable austenitic microstructure partially transforms to pearlite upon isothermal aging in the temperature range 500-600°C on a time scale of tens of hours. The observed transformation kinetics and microstructure development are interpreted in terms of the nucleation and growth of pearlite colonies. Preferential nucleation sites for pearlite formation are grain boundaries and prior plastic deformation increases the density of nucleation sites. Mn-partitioning between the ferrite and cementite lamellae in pearlite appears to control the growth rate, which is the underlying reason for the slow transformation kinetics.

6.1 Introduction

The austenitic phase in TWinning Induced Plasticity (TWIP) steel with 14 wt% Mn is metastable at room temperature, and is seen to transform to martensite by means of stress-induced γ (Face Centred Cubic, FCC) $\rightarrow$ ε (Hexagonal Close Packed, HCP) $\rightarrow$ α' (Body Centred Cubic, BCC) martensitic transformations [57, 76, 82, 84]. The mere occurrence of this $\gamma \rightarrow \alpha$'-martensite transformation indicates the austenite not to be stable at room temperature, but metastable [77]. Mn-contents below approximately 20 wt% form the basis for this meta-stability at room temperature, allowing the study of a broad domain of deformation and temperature conditions [85]. Whereas the metastable austenite transforms by martensitic mechanisms upon mechanical loading, diffusional decomposition of austenite into pearlite is expected when the material is annealed at temperatures below the A_1-temperature. This diffusional growth of pearlite has been subject of research for steels with relatively low Mn-contents (less than 1.8 wt%) [86, 87], studying the role of manganese during austenite to pearlite transformation in particular Mn-partitioning between pearlitic cementite and ferrite. The present work investigates the austenite decomposition at intermediate temperatures into pearlite in Mn-based steels with 14 wt% Mn.

Pearlite nucleates preferentially at prior austenite grain boundaries, compared to the grain interior, due to the interfacial energy [88]. Plastic deformation increases the stored energy within the austenite grains and of the austenite grain boundaries, enhancing the density of effective nucleation sites [89]. According to Xiao et al. [89], isothermal transformation of austenite results from the combined effect of short distance Fe-diffusion across the interface and long distance C-diffusion, with plastic deformation predominantly accelerating the latter.

Plastic deformation introduces microstructural defects like dislocations, twin boundaries and deformation bands within the austenite grains which are preferential nucleation sites for ferrite [85, 88-91] and pearlite [91, 92]. The number density of potential nucleation sites therefore increases with prior plastic deformation. Beladi et al. suggest that this process is static, providing more favourable nucleation conditions, but not affecting the transformation process itself [85]. In this chapter, using *in-situ* thermo-magnetic techniques and *ex-situ* magnetic techniques, optical microscopy and scanning electron microscopy, the nucleation and growth of the pearlite colonies in undeformed and deformed condition are systematically investigated. From observations on the pearlite fraction and the size distribution and number density of pearlite colonies, the characteristics of the austenite-to-pearlite transformation are derived.

6.2 Isothermal transformation

6.2.1 Formation of ferromagnetic phases

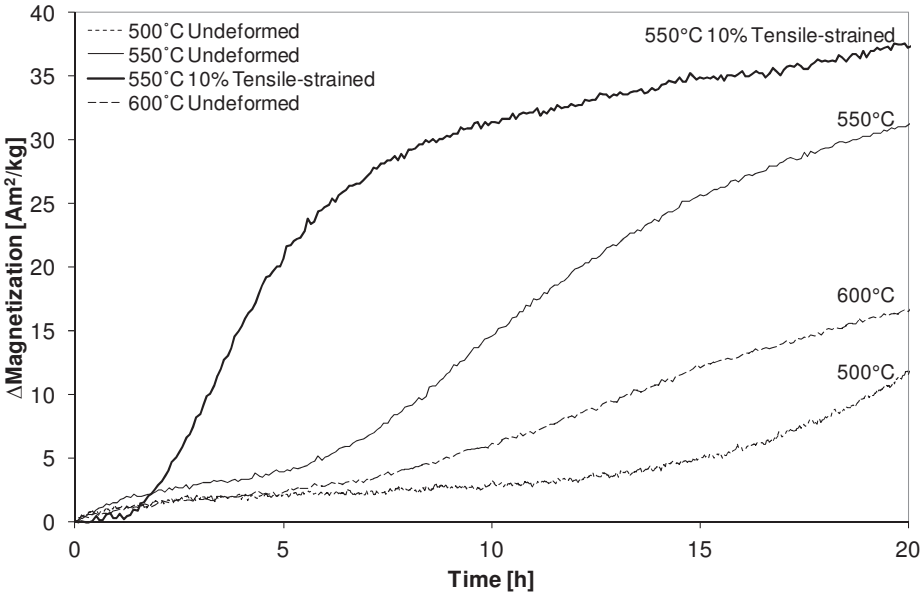

Figure 6.1 The change in magnetization during isothermal annealing at 500°C, 550°C and 600°C in undeformed condition and at 550°C in tensile-strained condition.

Figure 6.1 shows the change in magnetization in a field of 1.0 Tesla during *in-situ* isothermal annealing at 500°C, 550°C and 600°C in undeformed condition and at 550°C after 10% tensile straining. Isothermal annealing experiments performed at 400°C show no ferromagnetic phases to form within 20 hours. At the higher temperatures shown in Figure 6.1, initially the magnetization as a function of time remains low, but later increases more rapidly, indicating the formation of ferromagnetic phases. Note that the time scale of the transformation is on the order of 10 hours, which is orders of magnitude slower than for conventional pearlite formation. Isothermal annealing at 550°C displays the fastest transformation kinetics of the three studied temperatures, reaching the highest magnetization in the first 20 hours. Figure 6.1 also compares the magnetization during isothermal annealing at 550°C in undeformed condition and after tensile straining. Prior plastic deformation enhances the overall transformation rate and increases the degree of transformation reached within 20 hours. The curves in Figure 6.1 show the temperature dependence of the transformation kinetics that is also reflected in the well-known C-shaped curves in Temperature-Time-Transformation diagrams, with the transformation being slow at high temperature because of limited driving force and at low temperature because of limited

atomic mobility. Prior plastic deformation, in this case not more than 10% tensile straining, causes a significant shift to shorter times.

6.2.2 Formation of pearlite

SEM micrographs in Figure 6.2 show that pearlite is formed in isolated colonies with an internal lamella thickness in the order of tens of nanometres and give examples in which nucleation has taken place at grain boundaries.

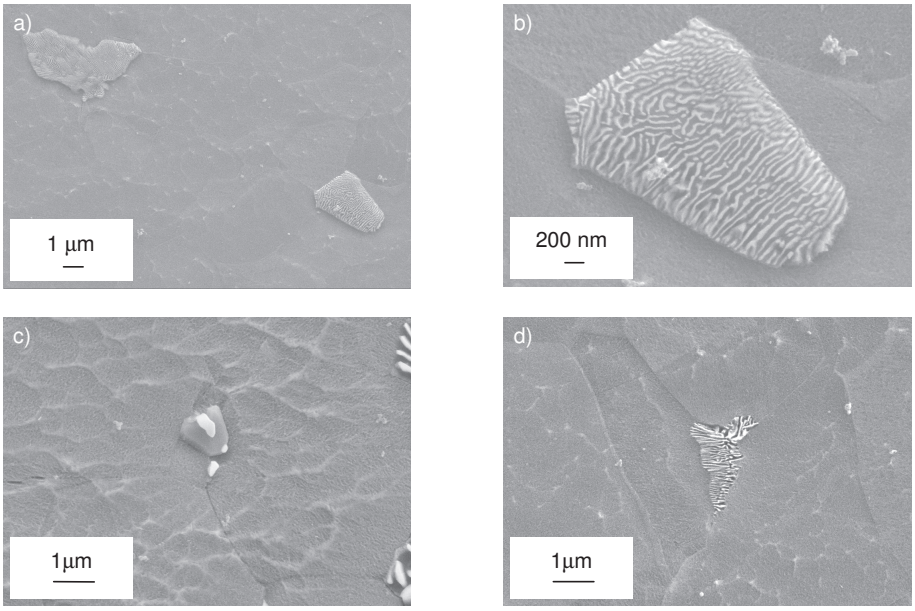

Figure 6.2 Scanning Electron Micrographs of the a) and b) ferromagnetic pearlite phase and c) and d) nucleation of a pearlite colony at (intersections of) grain boundaries in undeformed condition after 6 hours of isothermal annealing at 550°C.

Figure 6.3 shows the pearlite fraction from magnetisation measurements at room temperature after isothermal annealing at 550°C for different time intervals in undeformed condition and after 10% tensile straining. These room-temperature measurements were performed to obtain a more accurate quantification of the phase fractions. Also in these *ex-situ* measurements, prior plastic deformation is shown to enhance the formation rate of pearlite and to lead to a higher eventual fraction. Isothermal annealing during 70 hours at 550°C results in the formation of approximately 30% pearlite. The difference with the equilibrium fraction of 67% given by ThermoCalc (Figure 1.6) can be related to incomplete partitioning of manganese (see also the Transformation kinetics section of this chapter).

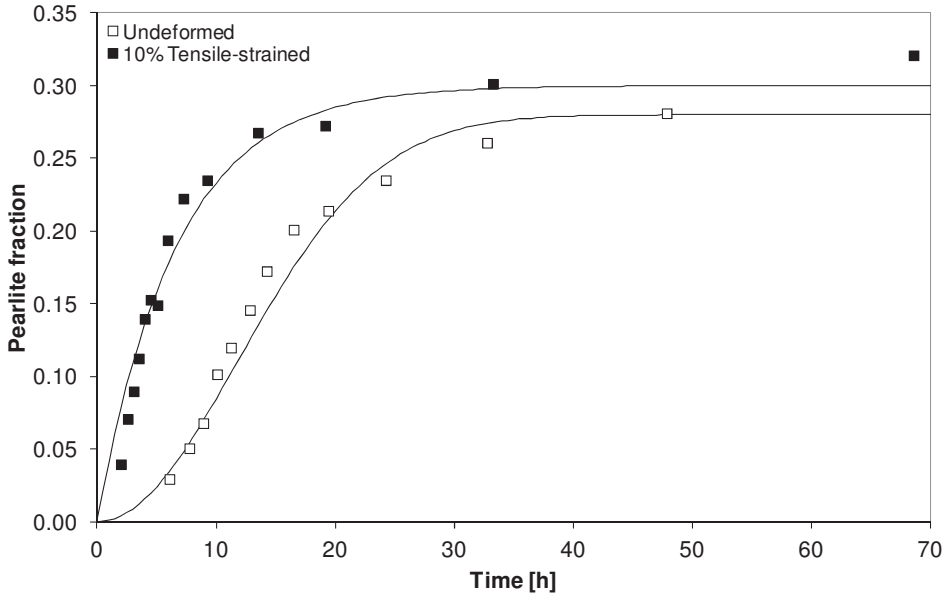

Figure 6.3 Pearlite fraction at room temperature after isothermal annealing at 550°C as a function of time in undeformed condition and after 10% tensile straining. The solid lines represent the fits of the Johnson-Mehl-Avrami Equation (6.1) [93-95].

The pearlite fraction as a function of holding time can be described by the Johnson-Mehl-Avrami Equation [93-95], adapted for the final ferrite fraction, given by

$$f(\alpha) = f_{\alpha}^{\,f}\left(1-\exp\left(-(kt)^{n}\right)\right) \quad , \tag{6.1}$$

where f_{α}^{f} is the final pearlite fraction at which saturation occurs, k is the rate parameter, n is the Avrami coefficient and t is the isothermal annealing time at 550°C. The parameters k and n reflect the nature of transformation. Figure 6.3 shows that the fit is in good agreement with the experimental results for f_{α}^{f} = 0.28, k = 0.06 s^{-1} and n = 2 in undeformed condition and f_{α}^{f} = 0.30, k = 0.17 s^{-1} and n = 1 for transformation after tensile straining.

6.2.3 Nucleation and growth of pearlite colonies

Figure 6.4a)-d) show microstructures of the undeformed and tensile-strained samples after isothermal annealing at 550°C. Isothermal annealing at 550°C results in the formation of pearlite colonies in the otherwise austenitic microstructure. The number density and size of pearlite colonies increase with isothermal annealing time. Prior plastic deformation is seen in the microstructures to increase the number density of pearlite colonies compared to the

undeformed condition for equal pearlite fractions. This observation is in agreement with the enhanced transformation kinetics, as expressed by the Avrami parameters resulting from Figure 6.3, an effect that is also presumably due to more effective nucleation [89, 96]. The decrease in the Avrami coefficient n due to prior deformation indicates nucleation to take place predominantly in the initial stage of the transformation, since the dimensionality of pearlite growth is not affected.

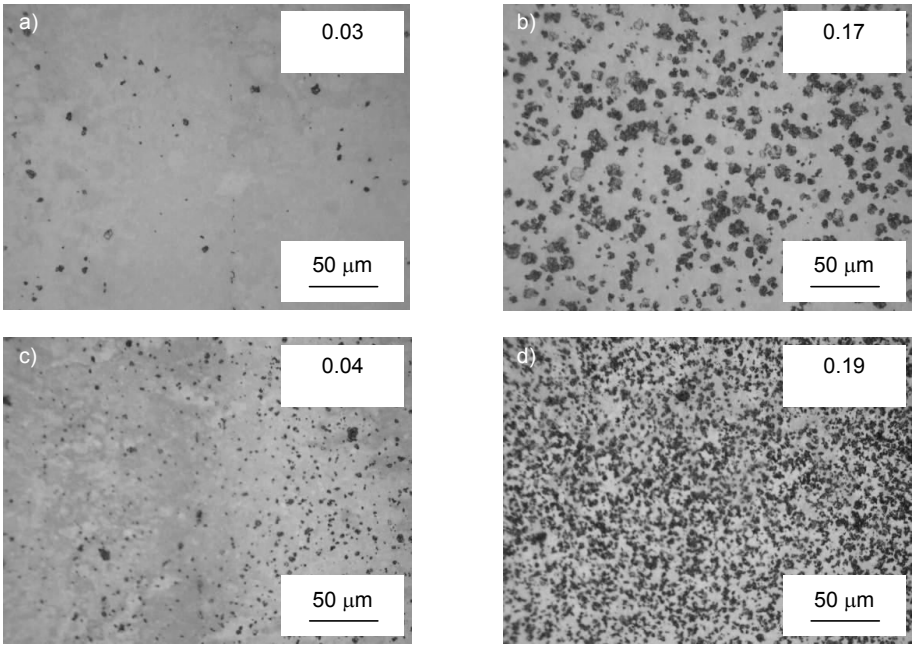

Figure 6.4 Optical micrographs of austenite (light grey) and pearlite (black) in undeformed condition after a) 6.1 hours and b) 14.3 hours of isothermal annealing at 550°C and in tensile-strained condition after c) 2.0 hours and d) 5.9 hours of isothermal annealing. The number in the top-right boxes indicates the pearlite fraction.

The optical micrographs were systematically analysed to quantify the number density of pearlite colonies during the transformation. In this analysis only those microstructures were considered in which all colonies could be distinguished separately. Figure 6.5 shows the number density of pearlite colonies in 2D micrographs against pearlite fraction in undeformed condition and after tensile straining.

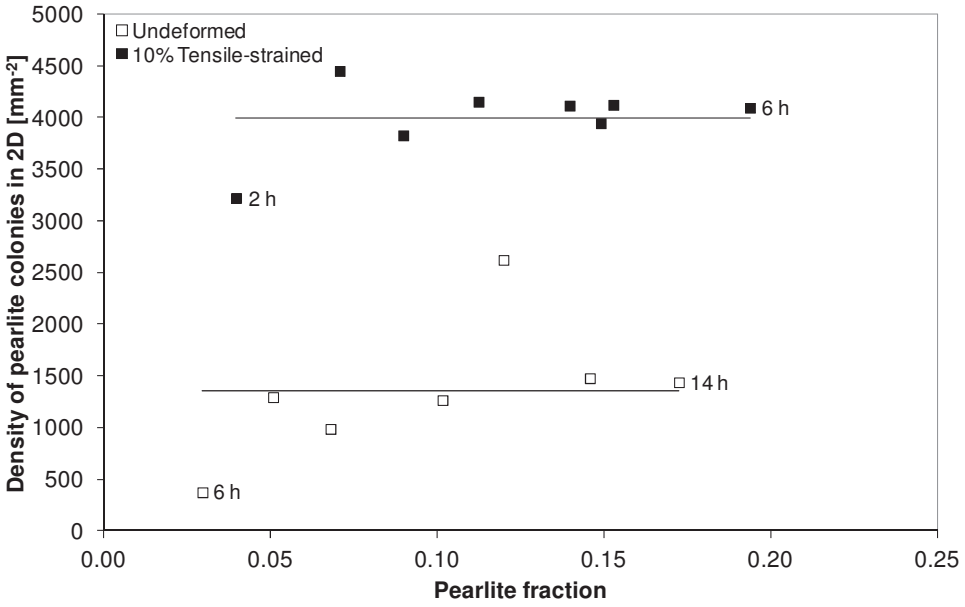

Figure 6.5 Density of pearlite colonies in 2D micrographs versus pearlite phase fraction.

Nucleation takes place within the first 5% of the transformation, where prior plastic deformation is shown to increase the density of pearlite colonies by approximately a factor three. The nucleation rate decreases to zero at a pearlite phase fraction of 5% for both the undeformed and the deformed microstructure. The nucleation rate can be expressed as [97, 98]

$$\dot{N} = \omega \cdot C_1 \cdot \exp\left(-\frac{\psi}{k_B T \left(\Delta G_c + E_s \right)^2} \right) \tag{6.2}$$

in which ω is a factor including the atom vibration frequency and critical nucleus area, C_1 reflects the density of potential nucleation sites, ψ is a constant related to the creation and annihilation of interfaces during nucleation, k_B the Boltzmann constant, T the temperature, ΔG_c the free-energy difference between austenite and pearlite and E_s the deformation energy stored in the austenite.

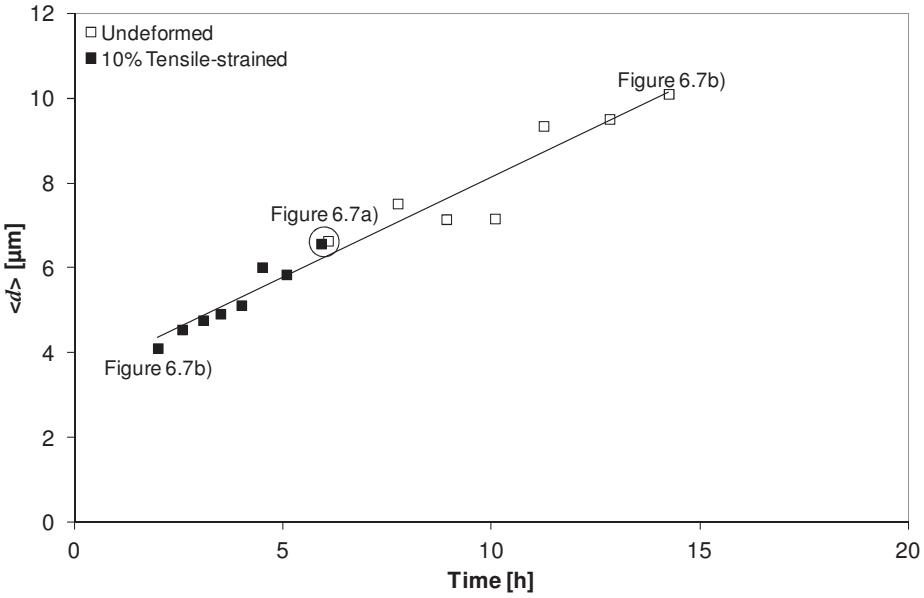

Figure 6.6 Experimental average equivalent diameter <*d*> of pearlite colonies as a function of time in undeformed condition and after tensile straining. The solid line is a linear fit of all data points. The samples taken for Figure 6.7a) and b) are indicated.

Figure 6.6 shows the experimental average equivalent diameter <*d*> of pearlite colonies as a function of time in undeformed condition and after tensile straining. The results show a constant average growth rate that is equal for both conditions. The initial average growth rate is significantly higher than the constant average growth rate shown by the data in Figure 6.6, since at $t = 0$ no pearlite colonies were present in the microstructure. An effect of prior plastic deformation on the initial average growth rate of the nuclei cannot be distinguished from the results of Figure 6.6.

The growth rate is represented by the interface velocity v [97], which can be expressed as

$$v = M_0 \cdot \exp\left(-\frac{Q}{k_B T}\right) \cdot \left(\Delta G + E_s\right) \tag{6.3}$$

where M_0 is the pre-exponential factor for the mobility and Q is the activation energy for interface motion [99]. Considering the interface velocity in relation to the free-energy difference (rather than in relation to undercooling) enables incorporation of the stored energy, showing the effect of prior deformation.

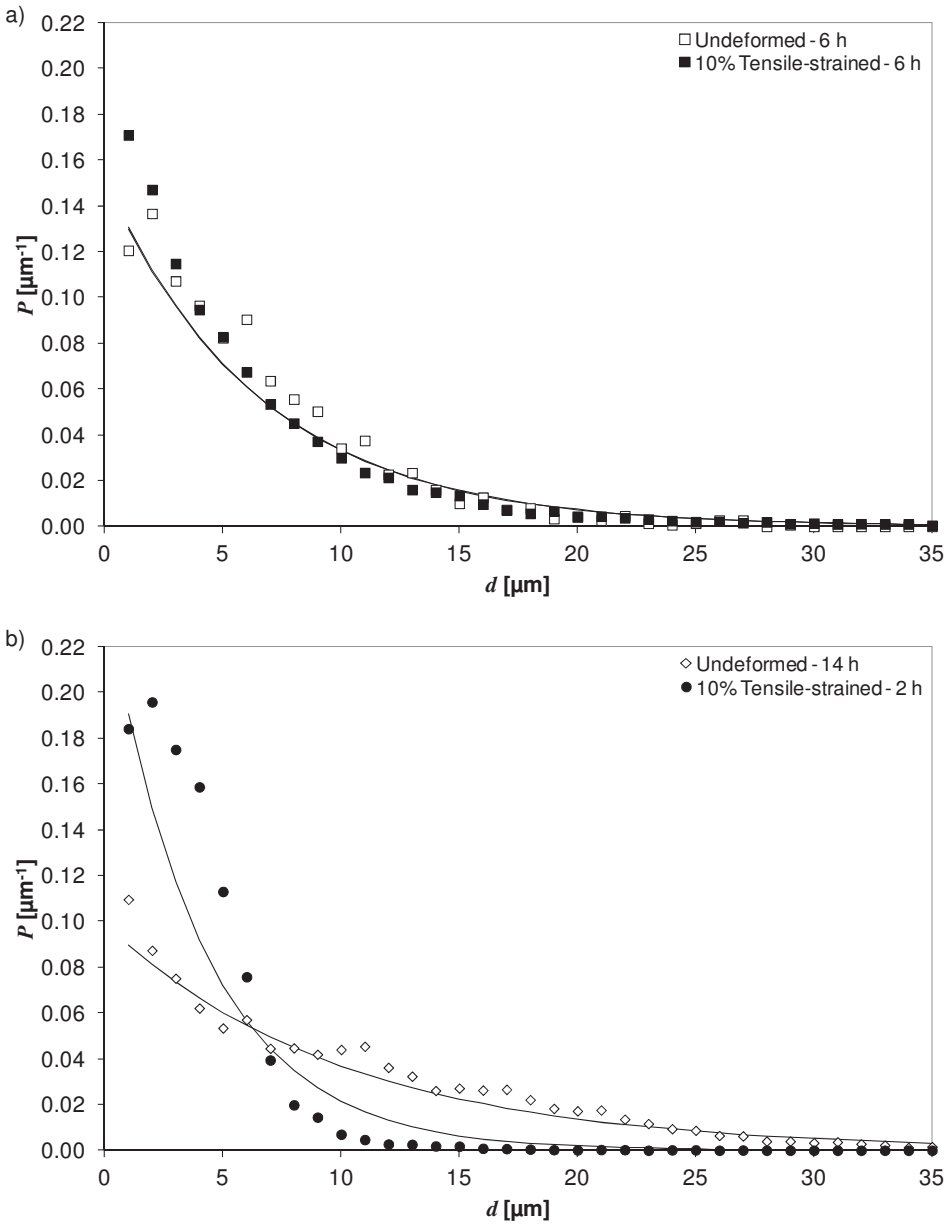

Figure 6.7 a) Distribution P of the equivalent diameter of pearlite colonies in undeformed condition and after tensile straining after 6 hours of isothermal annealing at 550°C. The corresponding pearlite fractions are 0.03 and 0.19, respectively. The minimum detected equivalent diameter for a pearlite colony is 1 µm. b) Distribution P of the equivalent diameter of pearlite colonies in undeformed condition after 14 hours annealing and after tensile straining and 2 hours annealing.

Whereas Figure 6.6 shows the average colony size, Figure 6.7 shows the size distribution P of pearlite colonies in some of the microstructures. The size distribution can in all cases be approximated by

$$P = \frac{1}{\langle d \rangle} \cdot \exp\left(-\frac{d}{\langle d \rangle} \right) \tag{6.4}$$

where d is the equivalent diameter of the pearlite colony and $<d>$ represents the average equivalent diameter of the pearlite colonies. Equation (6.4) is in good agreement with the experimental results of Figure 6.7. In Figure 6.7a) the size distribution is shown for the microstructures after 6 hours of isothermal annealing at 550°C, both in undeformed condition and after tensile straining. The phase fractions at this point are approximately 3% in undeformed condition and 20% after tensile straining (see Figure 6.3). The Figure shows that there is no significant difference between the size distributions for the undeformed and tensile-strained condition after 6 hours of isothermal annealing at 550°C, confirming the conclusion from Figure 6.6, namely that prior plastic deformation does not significantly affect the growth kinetics. Note that the number density of pearlite colonies differs by almost a factor 10 between these two conditions (see Figure 6.5). Figure 6.7b) shows that the description of the size distributions of the pearlite colonies by Equation (6.4) consistently applies also for the smallest (after 2 hours annealing in deformed condition) and largest size (after 14 hours annealing in undeformed condition).

The results of Figures 6.5-6.7 show that the increase in pearlite fraction due to prior plastic deformation is primarily a result of a higher density of potential nuclei and not a higher nucleation rate and/or a higher growth rate.

6.3 Transformation kinetics

The aim of this chapter is to investigate the pearlite formation in undeformed and deformed Mn-based TWIP steels, in particular the nucleation and growth of pearlite colonies, using magnetic measurements at room temperature and elevated temperature and optical microscopy. Isothermal annealing at 550°C results in a microstructure consisting of austenite and pearlite, which is a three-phase assembly as predicted by ThermoCalc (Figure 1.6). The presented observations show that a fully austenitic microstructure for this Mn-based TWIP steel grade is in a metastable state at temperatures below 600°C.

6.3.1 Manganese partitioning

Figure 6.8a) shows a schematic illustration of the Gibbs free energy as a function of the Mn-concentration for the three phases ferrite, austenite and cementite. This representation is just

schematic, because the C-concentrations in the three phases are distinctly different: very low in ferrite, initially equal to the overall concentration (0.71 wt%) in the austenite and 6.7 wt% in the cementite. This is depicted in Figure 6.8b), in which the equilibrium concentrations from ThermoCalc (Figure 1.6b)) are used. The open symbol in Figure 6.8b) indicates the overall composition of the steel, equal to the austenite composition before the transformation. The decomposition of austenite into ferrite and cementite according to equilibrium, indicated by the arrows, involves partitioning of both carbon and manganese between the three phases. Evidently at the time scale of this transformation complete partitioning of the carbon can be assumed. To indicate the length scales involved in the phase transformation, the diffusion distance of manganese in ferrite and austenite has been calculated for 10 hours of isothermal annealing at a temperature of 550°C, with a diffusivity of 4×10^{-22} m^2/s for austenite and 2×10^{-19} m^2/s for ferrite [90]. After 10 hours annealing the diffusion distances are in the order of 5 nm in austenite and 100 nm in ferrite. These distances indicate that Mn-partitioning between the ferrite and cementite lamellae within the pearlite can be accomplished (see the internal pearlite structure in Figure 6.2b), but significant partitioning between pearlite and austenite would involve much larger distances, see for instance Figure 6.4, and therefore much longer times (for instance 4×10^5 hours for 1 μm diffusion distance for manganese in austenite). Ortho-equilibrium conditions will therefore be reached between ferrite and cementite, but diffusion of manganese in the austenite over length scales on the order of 10 nm prevents accomplishing ortho-equilibrium between all three phases. The equilibrium state that is reached at the present time scales is therefore a combined condition of ortho-equilibrium between ferrite and cementite and para-equilibrium between pearlite and austenite. Since pearlite consists of two phases, the latter condition is characterised by the Mn-concentration in the austenite being equal to the *average* Mn-concentration of ferrite and cementite. The composition of the austenite is estimated by the triangle in Figure 6.8b). The corresponding austenite fraction is approximately 0.65, which is much higher than the equilibrium fraction of 0.25 given by ThermoCalc for equilibrium (see Figure 1.6). Figure 6.3 indicates that the austenite fraction approaches saturation at a value that is still somewhat larger than the fraction of 0.55 estimated from Figure 6.8b). This deviation is caused by the ferrite and cementite also assuming different concentrations in this combined equilibrium conditions, which cannot be accurately quantified from the present observations. The plastically deformed austenite phase will have a slightly higher free energy than the undeformed phase (see Figure 6.8a)), which causes its equilibrium fraction to be slightly lower. This is experimentally observed, as is shown in Figure 6.3.

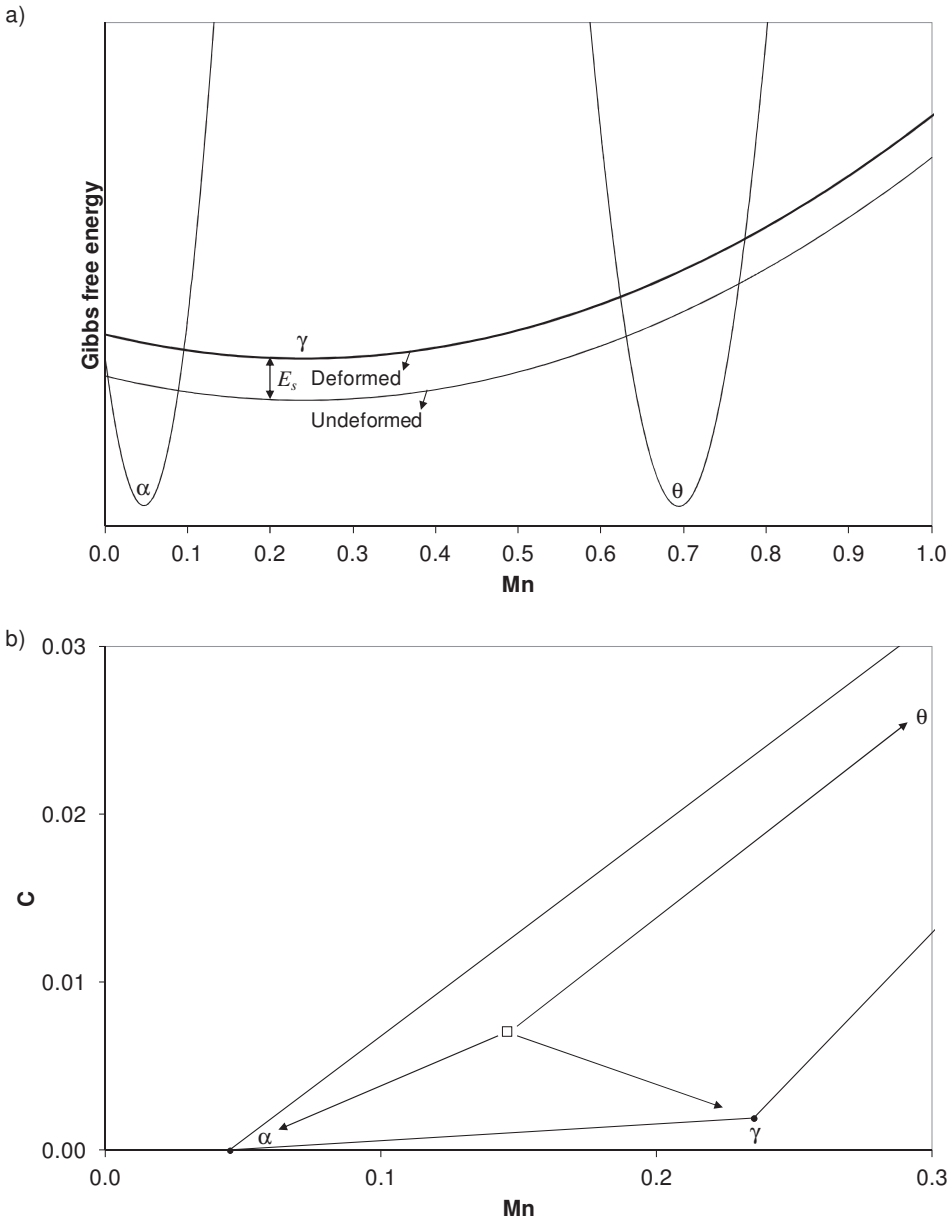

Figure 6.8 a) Schematic illustration of the Gibbs free energy for austenite, ferrite and cementite as a function of the Mn-content at 550°C. Note that the C-concentration of the three phases is different (see Figure 6.8b). b) The three phase region austenite-ferrite-cementite in the ternary Fe-C-Mn phase diagram. The open square is the average composition.

6.3.2 Effect of prior plastic deformation

The main effect of prior plastic deformation is to enhance the transformation rate from austenite to pearlite. According to Equations (6.2) and (6.3) prior plastic deformation will affect both the nucleation rate and the growth rate through the stored energy E_s. The stored energy can be determined by [100]

$$E_s = \alpha \frac{(\sigma - \sigma_{0.2})^2}{\mu} \tag{6.5}$$

where α is a constant, $\sigma_{0.2}$ the yield stress, σ the flow stress after deformation, and μ the shear modulus. After 10% tensile straining E_s equals 5.35 J/mol, using α = 2.3 [89] and μ = 72 GPa [101]. This value is distinctly lower than the chemical driving force ΔG, which is on the order of kJ/mol [102]. The stored energy E_s is therefore negligible as a contribution to the driving force for transformation and does not significantly affect the nucleation rate or growth rate in the observed timescale, as evidenced by the experimental results (Figures 6.5-6.7).

The increase in transformation rate is primarily due to a higher density of nuclei (Figure 6.5). During the transformation the nucleation rate is practically zero, so site saturation (*i.e.* nucleation taking place only in the initial stage of the transformation) governs the nucleation behaviour. As a consequence, the nucleation kinetics cannot be analysed from the present data (Figure 6.5). However, 10% tensile straining does not result in a heavily deformed microstructure [84], indicating that the density of potential nucleation sites at the grain boundaries will not significantly increase. The increased nucleation is therefore likely to result, on the one hand, from microstructural defects like dislocations, twin boundaries and deformation bands within the austenite grains (increasing C_1 in Equation (6.2)), on the other hand from an increased nucleation potency at grain boundaries (decreasing Ψ in Equation (6.2)). The presented results correspond to the static nucleation process proposed by Beladi et al. [85] and the growth rate being independent of prior plastic deformation as evidenced by Schmidt et al. [92].

In Mn-based TWIP steel, strain-induced α'-martensite is known to form at the intersections of shear bands such as slip bands, twins and/or ε-martensite laths [28, 35]. This indicates that these intersections are efficient nucleation sites for a body centred structure due to their incoherency and locally high stored deformation energy. For the same reason, (intersections of) grain boundaries and shear bands can be preferential nucleation sites for the formation of pearlite colonies. The presence of α'-martensite potentially facilitates the formation of ferrite within pearlite. Thus, prior plastic deformation results in the formation of

incoherent sites with locally high stored energy, which enhance the nucleation potential of pearlite.

The consequences of the transformation behaviour of this steel for controlling its microstructure and mechanical properties can be significant. The formation of pearlite colonies in the microstructure can form an additional strenghtening factor, the effect of which can be tailored through the number density of pearlite colonies by applying a small degree of prior deformation. Secondly, partial transformation of austenite to pearlite will enhance the stability of the austenite, reducing the susceptibility to α'-martensite formation, which is believed to be at the basis of delayed cracking in this material [57]. Finally, the C-concentration in the austenitic phase is significantly reduced during the phase transformation.

6.4 Conclusions

The presented investigation on the austenite stability in a Mn-based TWIP steel, using magnetic measurements at room and elevated temperature and optical microscopy leads to the following conclusions:

1. The austenitic microstructure of Mn-based TWIP steel is metastable and partly transforms to pearlite during isothermal annealing at temperatures in the range of 500-600°C.
2. The transformation kinetics are governed by Mn-partitioning between ferrite and cementite within the pearlite. Mn-diffusion is too slow to allow partitioning between pearlite and austenite, and a mixed equilibrium condition is established of ortho-equilibrium between ferrite and pearlite and para-equilibrium between pearlite and austenite. Nucleation of pearlite takes place only in the initial stages of the transformation.
3. Prior plastic deformation enhances the formation rate of pearlite from austenite and increases the number density of pearlite colonies, primarily through increased nucleation efficiency. Prior plastic deformation does not significantly affect the nucleation rate or growth rate in the observed timescale.

7 Conclusions

This thesis studies the effect of plastic deformation on the stability of the austenitic microstructure against martensitic transformation and diffusional decomposition and its role in the phenomenon of delayed fracture in austenitic manganese based TWinning Induced Plasticity steels. The transformation to α'-martensite and diffusional decomposition into pearlite shows the austenite to be metastable. An increase in the austenite stability is expected to improve the resistance against delayed fracture, based on these conclusions:

1. Positron annihilation detects that two different defect types result from plastic deformation during deep drawing. The two defect types can be expected to be dislocations and partial dislocations. Magnetic field measurements reveal the formation of α'-martensite which correlates with the density of the defects identified as partial dislocations.
2. The formation of α'-martensite is attributed to the accumulated equivalent strain and crystallographic texture. A model for α'-martensite volume fraction evolution upon straining is proposed and the estimated fraction of intersected shear bands - the preferred nucleation sites for α'-martensite formation - as a function of accumulated equivalent strain is in good agreement with the experimentally determined α'-martensite fraction.
3. The presence of α'-martensite at shear band and twin intersections is observed and questions the sequential $\gamma \rightarrow \varepsilon \rightarrow \alpha$' martensitic transformation. The Stacking Fault Energy (SFE) in the SFE range tested does not affect the formation of α'-martensite.
4. Delayed fracture occurs along the transverse direction where the α'-martensite fraction is the highest. An intermittent crack propagation concept and model is proposed based on the coalescence of initial cracks into a macrocrack. A higher α'-martensite fraction indicates a higher density of shear-band intersections, resulting in more potential crack-

initiation sites and easier coalescence. The order of delayed fracture susceptibility in terms of crack length L, delay time t_0 and duration of the active period of crack growth t_1 - t_0 indicates no direct relation with the SFE.

5. The austenite decomposition into pearlite upon annealing at intermediate temperatures is governed by Mn-partitioning between ferrite and cementite within the pearlite. Nucleation of pearlite takes place only in the initial stages of the transformation. Prior plastic deformation enhances the formation rate of pearlite from austenite and increases the number density of pearlite colonies, primarily through increased nucleation efficiency. Prior plastic deformation does not significantly affect the nucleation rate or growth rate in the observed timescale.

Bibliography

[1] www.worldautosteel.org, 2013.

[2] G. Frommeyer and O. Grässel, High strength TRIP/TWIP and superplastic steels: Development, properties, application, Revue de Metallurgie, Cahiers D'Informations Techniques, vol. 95, no. 3, pp. 1299-1310, 1998.

[3] C. Scott, N. Guelton, S. Allain and M. Faral, The development of a new Fe-Mn-C austenitic steel for automotive applications, Material Science and Technology, pp. 127-138, 2005.

[4] L. Bracke, G. Mertens, J. Penning, B.C. De Cooman, M. Lieberherr and N. Akdut, High manganese austenitic twinning induced plasticity steels: A review of the microstructure properties relationships, Metallurgical and Materials Transactions A, vol. 37, pp. 307-317, 2006.

[5] X. Guo, J. Post, M. Groen and W. Bleck, Stress oriented delayed cracking induced by dynamic martensitic transformation in meta-stable austenitic stainless steels, Steel Research International, vol. 81, no. 13, pp. 1-8, 2010.

[6] M.R. Berrahmoune, S. Bervieller, K. Inal and E. Patoor, Delayed cracking in 301LN austenitic steel after deep drawing: Martensitic transformation and residual stress analysis, Materials Science and Engineering A, vol. 262, pp. 438-440, 2006.

[7] A.W. Thompson, Current status of the role of hydrogen in stress corrosion cracking, Materials Science and Engineering A, vol. 43, pp. 41-46, 1979.

[8] O. Bouaziz, S. Allain, C.P. Scott, P. Cugy and D. Barbier, High manganese austenitic twinning induced plasticity steels: A review of the microstructure properties relationships, Current Opinion in Solid State and Materials Science, vol. 15, pp. 141-168, 2011.

[9] B.C. De Cooman, L. Chen, Y. Estrin, S.K. Kim and H. Voswinckel, Microstructure and texture in steels and other materials, State-of-the-Science of high Manganese TWIP steels for automotive applications, Part II, Springer, pp. 165-183, 2009.

[10] S.J. Harris, N.R. Nag, Effect of warm working on the precipitation of vanadium carbide in a medium carbon austenitic steel, Journal of Materials Science, vol. 11, no. 7, pp. 1320-1329, 1976.

[11] M. Koyama, E. Akiyama, T. Sawaguchi, D. Raabe and K. Tsuzaki, Hydrogen-induced cracking at grain and twin boundaries in an Fe-Mn-C austenitic steel, Scripta Materialia, vol. 66, pp. 459-462, 2012.

[12] W. Tofaute, K. Linden, Die Umwandlung im festen Zustande bei Manganstählen mit Gehalten bis 1,2% C and 17% Mn, Archiv für das Eisenhüttenwesen, vol. 10, pp. 515-524, 1936.

[13] W. Schmidt, Röntgenographische Untersuchungen über das System Eisen-Mangan, Archiv für das Eisenhüttenwesen, vol. 3, pp. 293-300, 1929-1930.

[14] A.R. Troiano, F.T. McGuire, A study of the iron-rich iron-manganese alloys, Transactions of the ASM, vol. 31, pp. 340-364, 1943.

[15] H.C. Doepken, Tensile properties of wrought austenitic manganese steel, Journal of Metals, pp. 166-170, 1952.

[16] H.M. Otte, The formation of stacking faults in austenite and its relation to martensite, Acta Materialia, vol. 5, pp. 614-627, 1957.

[17] C.H. White, R.W.K. Honeycomb, Structural changes during the deformation of high-purity iron-manganese-carbon alloys, Journal of the Iron and Steel Institute, vol. 200, pp. 457-466, 1962.

[18] K.S. Raghavan, A.S. Sastri, M.J. Marcinkovski, Nature of work-hardening behaviour in Hadfield's manganese steel, Transactions of the Metallurgical Society of AIME, vol. 245, no. 7, pp. 1569-1575, 1969.

[19] W.N. Roberts, Deformation Twinning in Hadfield Steel, Transactions of the Metallurgical Society of AIME, vol. 230, pp. 372-377 1964.

[20] A.S. Sastri, Strengthening of commercial austenitic manganese steel by mechanical and thermal treatment, Proceedings of the 3rd International Conference on the Strength of Materials, Cambridge, England, 1973.

[21] G. Colette, C. Crussard, A. Kohn, J. Plateau, G. Pomey, M. Weiz, Contribution á l'étude austenites a 12% Mn, Revue de Metallurgie, Cahiers D'Informations Techniques, vol. 54, no. 6, pp. 433-486, 1957.

[22] L. Rémy, Ph.D. thesis, Université de Paris-Sud, Orsay, France, 1975.

[23] J. Charles, A. Berzhegan, A. Lutts, P.L. Dancoisne, New cryogenic materials – Fe-Mn-Al alloys, Metal progress, vol. 119, no. 6 ,pp. 71-74, 1981.

[24] O. Kubashevski, Iron Binary Phase Diagrams, Verlag Stahleisen Gmbh, Düsseldorf, Germany, 1982.

[25] H. Schumann, Martensitische Umwandlungen in austenitischen Mangan-Kohlenstoff-Stählen, Neue Hütte, vol. 17, pp. 605-609, 1972.

[26] D. Hull and D.J. Bacon, Introduction to dislocations, Department of Engineering, Material Science and Engineering, University of Liverpool, Liverpool, United Kingdom, 2001.

[27] L. Bracke, Deformation behaviour of austenitic Fe-Mn alloys by Twinning and Martensitic Transformation, Ph.D. thesis, University of Ghent, Ghent, Belgium, 2007.

[28] G.B. Olson and M. Cohen, A mechanism for the strain-induced nucleation of martensitic transformations, Journal of the Less-Common Metals, vol. 28, pp. 107-118, 1972.

[29] B.W. Oh, S.J. Cho, Y.G. Kim, W.S. Kim and S.H. Hong, Effect of aluminium on deformation mode and mechanical properties of austenitic Fe-Mn-Cr-Al-C alloys, Materials Science and Engineering A, vol. 197, pp. 147, 1995.

[30] G.B. Olson and W.S. Owen, Martensite A Tribute to Morris Cohen, ASM International, 1992.

[31] T. Angel, Formation of martensite in metastable austenite, Journal of the Iron and Steel Institute, vol. 177, pp. 165-174, 1954.

[32] D.C. Ludwigson and J.A. Berger, Plastic behaviour of metastable austenitic stainless steels, Journal of the Iron and Steel Institute, vol. 207, pp. 63-69, 1969.

[33] W.W. Gerberich, G. Thomas, E.R. Parker and V.F. Zackay, Metastable austenites: Decomposition and strength, 2nd International Conference Strength of Metals and Alloys, Pacific Grove, California, United Stated of America, vol. 3, pp. 894-899, 1970.

[34] J.R.C. Guimaraes, The deformation-induced martensitic reaction in polycrystalline Fe 30.7 Ni - 0.06C, Scripta Metallurgica, vol. 6, pp. 795-798, 1972.

[35] G.B. Olson and M. Cohen, Kinetics of nucleation strain-induced martensitic nucleation, Metallurgical and Materials Transactions A, vol. 6, pp. 791-795, 1975.

[36] M. Koyama, E. Akiyama and K. Tsuzaki, Hydrogen-induced delayed failure of a Fe-22Mn-0.6C steel pre-strained at different strain rates, Scripta Materialia, vol. 66, pp. 947-950, 2012.

[37] M. Koyama, E. Akiyama and K. Tsuzaki, Hydrogen embrittlement in a Fe-Mn-C ternary twinning-induced plasticity steel, Corrosion Science, vol. 54, pp. 1-4, 2012.

[38] M. Koyama, E. Akiyama and K. Tsuzaki, Effect of hydrogen content on the embrittlement in a Fe-Mn-C twinning-induced plasticity steel, Corrosion Science, vol. 59, pp. 277-281, 2012.

[39] M. Koyama, T. Sawaguchi and K. Tsuzaki, Premature Fracture Mechanism in a Fe-Mn-C Austenitic Steel, Metallurgical and Materials Transactions A, vol. 43, pp. 4063-4074, 2012.

[40] Y.S. Chun, J.S. Kim, K.-T. Park, Y.-K. Lee and C.S. Lee, Role of ε martensite in tensile properties and hydrogen degradation of high-Mn steels. Materials Science and Engineering A, vol. 533, pp. 87-95, 2012.

[41] Y.S. Chun, J. Lee, C.M. Bae, K.-T. Park and C.S. Lee, Caliber-rolled TWIP steel for high-strength wire rods with enhanced hydrogen-delayed fracture resistance, Scripta Materialia, vol. 67, pp. 681-684, 2012.

[42] Y.S. Chun, K.-T. Park and C.S. Lee, Delayed static failure of twinning-induced plasticity steels, Scripta Materialia, vol. 66, pp. 960-965, 2012.

[43] K.-G. Chin, C.-Y. Kang, S.Y. Shin, S. Hong, S. Lee, H.S. Kim, K.-h. Kim and N.J. Kim, Effects of Al addition on deformation and fracture mechanisms in two high manganese TWIP steels, Materials Science and Engineering A, vol. 528, pp.2922-2928, 2011.

[44] J.A. Ronevich, S.K. Kim, J.G. Speer and D.K. Matlock, Hydrogen effects on cathodically charged twinning-induced plasticity steel, Scripta Materialia, vol. 66, pp. 956-959, 2012.

[45] C. Efstathiou and H. Sehitoglu, Strain hardening and heterogeneous deformation during twinning in Hadfield steel, Acta Materialia, vol. 58, pp. 1479-1488, 2010.

[46] D. Barbier, N. Gey, S. Allain, N. Bozzolo and M. Humbert, Analysis of the tensile behavior of a TWIP steel based on the texture and microstructure evolutions, Materials Science and Engineering A, vol. 500, pp. 196-206, 2009.

[47] X. Liang, J.R. McDermid, O. Bouaziz, X. Wang, J.D. Embury and H.S. Zurob, Microstructural evolution and strain hardening of Fe-24Mn and Fe-30Mn alloys during tensile deformation, Acta Materialia, vol. 57, pp. 3978-3988, 2009.

[48] S. Curtze and V.-T. Kuokkala, Dependence of tensile deformation behavior of TWIP steels on stacking fault energy, temperature and strain rate, Acta Materialia, vol. 58, pp. 5129-5141, 2010.

[49] W. Bleck, K. Phiu-on K, C. Heering C, G. Hirt, Hot workability of as-cast high Manganese-high Carbon steels, Steel Research International, vol. 78, no. 7, pp. 536-545, 2007.

[50] P.C.J. Gallagher, The influence of alloying, temperature, and related effects on the stacking fault energy, Metallurgical Transactions, vol. 1, pp. 2429-2461, 1970.

[51] B.W. Oh, S.J. Cho, Y.G. Kim, W.S. Kim and S.H. Hong, Effect of aluminium on deformation mode and mechanical properties of austenitic Fe-Mn-Cr-Al-C alloys, Materials Science and Engineering A, vol. 197, pp. 147-156, 1995.

[52] H. Vegter and A.H. van den Boogaard, A plane stress yield function for anisotropic sheet material by interpolation of biaxial stress states, International Journal of Plasticity, vol. 22, pp. 557-580, 2006.

[53] L. Zhao, N.H. van Dijk, A.J.E. Lefering and J. Sietsma, Magnetic detection of small fractions of ferromagnetic martensite within the paramagnetic austenite matrix of TWIP steel, Journal of Materials Science, vol. 48, pp. 1474–1479, 2013.

[54] L. Zhao, N.H. van Dijk, E. Brück, J. Sietsma, S. van der Zwaag, Magnetic and X-ray diffraction measurements for the determination of retained austenite in TRIP steels, Materials Science and Engineering A, vol. 313, pp. 145-152, 2001.

[55] H. Schut, A variable energy positron beam facility with applications in materials science, Ph.D. thesis, Delft University of Technology, Delft, The Netherlands, 1990.

[56] R. Krause-Rehberg and H.H. Leipner, Positron annihilation in semiconductors: Defect studies, Springer, Berlin, Germany, 1999.

[57] R.T. van Tol, L. Zhao and J. Sietsma, Effect of strain on the deformation mechanism in austenitic Mn-based TWIP steels, The 1st International Conference on High Mn TWIP Steels HMnS2011, Seoul, South Korea, 2011.

[58] V.G. Gavriljuk, V.N. Bugaev, Y.N. Petrov, A.V. Tarasenko and B.Z. Yanchitski, Hydrogen-induced equilibrium vacancies in fcc iron-base alloys, Scripta Materialia, vol. 34, pp. 903-907, 1996.

[59] M. Nagumo, Hydrogen related failure of steels - a new aspect, Material Science and Technology, vol. 20, pp. 940-950, 2004.

[60] F. Besenbacher, S.M. Myers and J.K. Norskov, Interaction of hydrogen with defects in metals, Nuclear Instruments and Methods in Physics Research B, vol. 7-8, pp. 55-66, 1985.

[61] P.J. Ferreira, I.M. Robertson and H.K. Birnbaum, Hydrogen effects on the interaction between dislocations, Acta Materialia, vol. 46, pp. 1749-1757, 1998.

[62] J.-D. Kamminga and L.J. Seijbel, Diffraction line broadening analysis if broadening is caused by both dislocations and limited crystallite size, Journal of Research of the National Institute of Standards and Technology, vol. 109, pp. 65-74, 2004.

[63] H. Ohkubo, S. Sugiyama, K. Fukuzato, M. Takenaka, N. Tsukuda and E. Kuramoto, Positron-lifetime study of electrically hydrogen charged Ni, austenitic stainless steel and Fe, Journal of Nuclear Materials, vol. 283-287, pp. 858-862, 2000.

[64] K. Sakaki, T. Kawase, M. Hirato, M. Mizuno, H. Araki, Y. Shirai and M. Nagumo, The effect of hydrogen on vacancy generation in iron by plastic deformation, Scripta Materialia, vol. 55, pp. 1031-1034, 2006.

[65] G.M. Hood and R.J. Schultz, Effect of hydrogen alloying on positron annihilation in Ti, Scripta Metallurgica, vol. 18, pp. 141-144, 1983.

[66] H.F.M. Mohamed, J. Kwon, Y.-M. Kim and W. Kim, Vacancy-type defects in cold-worked iron studied using positron annihilation techniques, Nuclear Instruments and Methods in Physics Research B, vol. 258, pp. 429-434, 2007.

[67] H.K. Birnbaum and P. Sofronis, Hydrogen-enhanced localized plasticity - a mechanism for hydrogen-related fracture, Materials Science and Engineering A, vol. 176, pp. 191-202, 1994.

[68] J.W. Christian and S. Mahajan, Deformation twinning, Progress in Materials Science, vol. 39, pp. 1-157, 1995.

[69] L. Bracke, L. Kestens and J. Penning, Transformation mechanism of α'-martensite in an austenitic Fe-Mn-C-N alloy, Scripta Materialia, vol. 57, pp. 385-388, 2007.

[70] D. Cornette, P. Cugy, A. Hildenbrand, M. Bouzekri and G. Lovato, Ultra high strength FeMn TWIP steels for automotive safety parts, SAE Conference, Detroit, United States of America, pp. 1-13, 2005.

[71] G. Frommeyer, U. Brüx and P. Neumann, Supra-ductile and high-strength Manganese-TRIP/TWIP steels for high energy absorption purposes, ISIJ International, vol. 43, no. 3, pp. 438-446, 2003.

[72] S. Allain, J.-P. Château, O. Bouaziz, S. Migot and N. Guelton, Materials Science and Engineering A, vol. 387-389, pp. 158-162, 2004.

[73] B.X. Huang, X.D. Wang, Y.H. Rong, L. Wang and L. Jin, Mechanical behavior and martensitic transformation of an Fe-Mn-Si-Al-Nb alloy, Materials Science and Engineering A, vol. 438-440, pp. 306-311, 2006.

[74] H. Ding, H. Ding, D. Song, S. Tang and P. Yang, Strain hardening behavior of a TRIP/TWIP steel with 18.8% Mn, Materials Science and Engineering A, vol. 528, pp. 868-873, 2011.

[75] K. Sato, M. Ichinose, Y. Hirotsu and Y. Inoue, Effects of deformation induced phase transformation and twinning on the mechanical properties of austenitic Fe-Mn-Al alloys, ISIJ International, vol. 29, pp. 868-877, 1989.

[76] R.T. van Tol, L. Zhao, H. Schut and J. Sietsma, Experimental investigation of structural defects in deep-drawn austenitic Mn-based TWIP steel, Material Science and Technology, vol. 28, no. 3, pp. 348-353, 2012.

[77] Y. Tomota, M. Strum and J.W. Morris, Microstructural dependence of Fe-high Mn tensile behavior, Metallurgical Transactions A, vol. 17, pp. 537-547, 1986.

[78] L. Xu and F. Barlat, Macroscopic constitutive modeling of a TWIP steel sheet sample, The 1st International Conference on High Mn TWIP Steels HMnS2011, Seoul, South Korea, 2011.

[79] K.H. Lo, C.H. Shek and J.K.L. Lai, Recent developments in stainless steels, Materials Science and Engineering R, vol. 65, pp. 39-104, 2009.

[80] N. Elhami, S. Zaefferer, I. Thomas and H. Hofmann, The 1st International Conference on High Mn TWIP Steels HMnS2011, Seoul, South Korea, 2011.

[81] R.A. McCoy and W.W. Gerberich, Hydrogen embrittlement studies of a TRIP steel, Metallurgical Transactions, vol. 4, pp. 539-547, 1973.

[82] R.T. van Tol, J.K. Kim, L. Zhao, J. Sietsma and B.C. De Cooman, α'-Martensite Formation in deep-drawn Mn-based TWIP Steel, Journal of Materials Science, vol. 47, pp. 4845-4850, 2012.

[83] D. Barbier, V. Favier and B. Bolle, Modeling the deformation textures and microstructural evolutions of a Fe-Mn-C TWIP steel during tensile and shear testing, Materials Science and Engineering A, vol. 540, pp. 212-225, 2012.

[84] R.T. van Tol, L. Zhao, H. Schut and J. Sietsma, Investigation of deformation mechanisms in deep-drawn and tensile-strained austenitic Mn-based TWIP steel, Metallurgical and Materials Transactions A, vol. 43, no. 9, pp. 3070-3077, 2012.

[85] H. Beladi, G.L. Kelly and P.D. Hodgson, The effect of multiple deformations on the formation of ultrafine grained steels, Metallurgical and Materials Transactions A, vol. 38, pp. 450-463, 2007.

[86] N.A. Razik, G.W. Lorimer and N. Ridley, An investigation of manganese partitioning during the austenite-pearlite transformation using analytical electron microscopy, Acta Materialia, vol. 22, pp. 1249-1258, 1974.

[87] A.S. Pandit and H.K.D.H. Bhadeshia, Diffusion-controlled growth of pearlite in ternary steels, Proceedings of the Royal Society A, vol. 467, pp. 2948-2961, 2011.

[88] C. Zheng, N. Xiao, L. Hao, D. Li and Y. Li, Numerical simulation of dynamic strain-induced austenite-ferrite transformation in a low carbon steel, Acta Materialia , vol. 57, pp. 2956-2968, 2009.

[89] N. Xiao, M. Tong, Y. Lan, D. Li and Y. Li, Coupled simulation of the influence of austenite deformation on the subsequent isothermal austenite-ferrite transformation, Acta Materialia, vol. 54, pp. 1265-1278, 2006.

[90] Z.-D. Li, Z.-G. Yang, C. Zhang and Z.-Q. Liu, Influence of austenite deformation on ferrite growth in a Fe-C-Mn alloy, Materials Science and Engineering A, vol. 527, pp. 4406-4411, 2010.

[91] N. Tsuji and T. Maki, Enhanced structural refinement by combining phase transformation and plastic deformation in steels, Scripta Materialia, vol. 60, pp. 1044-1049, 2009.

[92] E. Schmidt, Y. Wang and S. Sridhar, A study of nonisothermal austenite formation and decomposition in Fe-C-Mn alloys, Metallurgical and Materials Transactions A, vol. 37, pp.1799-1810, 2006.

[93] M. Avrami, Kinetics of phase change. I. General theory, Journal of Chemical Physics, vol. 7, no. 12, pp. 1103-1112, 1939.

[94] M. Avrami, Kinetics of phase change. II. Transformation-time relations for random distribution of nuclei, Journal of Chemical Physics, vol. 8, no. 2, pp. 212-224, 1940.

[95] M. Avrami, Kinetics of phase change. III. Granulation, phase change, and microstructure, Journal of Chemical Physics, vol. 9, no. 2, pp. 177-184, 1941.

[96] D.N. Hanlon, J. Sietsma and S. van der Zwaag, ISIJ International, vol. 41, no. 9, pp. 1028-1036, 2001.

[97] D.A. Porter and K.E. Easterling, Phase Transformations in Metals and Alloys, second edition, CRC press, Boca Raton, Florida, United States of America, 2001.

[98] S.E. Offerman, N.H. van Dijk, J. Sietsma, S. Grigull, E.M. Lauridsen, L. Margulies, H.F. Poulsen, M.Th. Rekveldt and S. van der Zwaag, Grain Nucleation and Growth During Phase Transformations, Science, vol. 298, pp. 1003-1005, 2002.

[99] J.W. Christian, The theory of transformations in metals and alloys: an advanced textbook in physical metallurgy, third edition, Pergamon Press, Amsterdam, The Netherlands, 2002.

[100] A. Godfrey, W.Q. Cao, N. Hansen and Q. Liu, Stored Energy, Microstructure, and Flow Stress of Deformed Metals, Metallurgical and Materials Transactions A, vol. 36, pp. 2371-2378, 2005.

[101] O. Bouaziz and N. Guelton, Modelling of TWIP effect on work-hardening, Materials Science and Engineering A, vol. 319–321, pp. 246–249, 2001.

[102] T. Kop, A dilatometric study of the austenite/ferrite interface mobility, Ph.D. thesis, Delft University of Technology, Delft, The Netherlands, 2000.